

ROLE OF NANOCONFINEMENT ON THIN FILM
EVAPORATION

By

Bahareh Eslami

A dissertation submitted to the Department of Mechanical Engineering

Cullen College of Engineering

in partial fulfillment of the requirement for the degree

DOCTOR OF PHILOSOPHY

in Mechanical Engineering

Chair of Committee: Hadi Ghasemi

Committee Member: Ralph Metcalfe

Committee Member: Dong Liu

Committee Member: Haleh Ardebili

Committee Member: Alamgir Karim

University of Houston
December 2020

Copyright 2020, Bahareh Eslami

DEDICATION

To my parents, Ezzat and Mahmoud for their unconditional love.

ACKNOWLEDGMENT

First of all, I would like to express my sincere thanks to my advisor, Professor Hadi Ghasemi for his continuous support, encouragement, and valuable comments that made this work successful. I'm also thankful to members of my dissertation committee: Professor Ralph Metcalfe, Professor Dong Liu, Professor Haleh Ardebili, and Professor Alamgir Karim for their time to review my work and attend my defense.

Additionally, I would like to thank the faculty and staff of the Nanofabrication Facility at the University of Houston for providing support and advice. I'm also grateful to my fellow lab members for interesting and stimulating discussions and good times. Also, I want to take this opportunity and extend my gratitude to many friends in Houston who helped me by their warm support and soothing company.

I owe my deepest gratitude to my beloved parents, Ezzat and Mahmoud and my supportive brothers, Moein and Amin. From the bottom of my heart, I want to acknowledge all of their love and support throughout my life and specially during my Ph.D. program. Last, but certainly not least, I must acknowledge with special thanks my husband, Milad, who has made Houston special for me. You make me a better person. Thanks for your love, support and encouragement.

ABSTRACT

Thin film boiling and evaporation have been recognized as most efficient thermal management solutions for reliable operations of high power density electronics. Liquid-vapor phase change process plays an important role in many natural phenomena and industrial applications ranging from thermal management of electronics, power generation, water harvesting, and water desalination. Enhancing liquid-vapor phase change efficiency push the boundaries specially in electronic industry. To achieve this purpose, many efforts have been devoted for better understanding of the underlying mechanism and improving performance solutions. Recent progress in micro/nano fabrication techniques have opened an avenue for scientists and engineers to elevate thermal conversion and management by manipulating effective parameters. Herein, we aim to survey the most enlightening recent advances in developing various nanoengineered architectures for thin film evaporation enhancement including micropillars and nanowires, micro/nano porous membranes, hierarchical structures, and micro/nano channels. We study their functionalities and compare their efficiencies. In the next step, we focused on the role of planar nanoporous membranes in thermal management due to their high heat removal potential. We utilized anodic aluminum oxide (AAO) membranes and a high heat flux of 560 W/cm^2 is achieved with wall superheat of $\sim 60 \text{ }^\circ\text{C}$. Thin film boiling as the next stage of pool boiling dramatically increases the bubble departure frequency as a result of reduced conduction resistance in liquid microlayer. As boiling regime enters the thin film region, the bubble diameter significantly shrinkages promoting the departure process. Moreover, separate liquid-vapor pathways play a critical role by providing liquid to nucleation sites in a more

efficient way. This work suggests utilizing thin film boiling as an advanced strategy for promoting heat removal performance in high power electronics.

Table of Contents

Acknowledgment	iv
Abstract	v
Table of Contents	vii
List of Figures	ix
Chapter 1 Introduction	1
1.1 Background	1
1.2 Micropillar/Nanowires	3
1.3 Hierarchical Structures.....	9
1.4 Thin Membranes.....	12
1.5 Isotropic Porous Structures.....	16
1.6 Hybrid Structures.....	20
1.7 Micro/nano Channels.....	23
Chapter 2 Role of Nanoconfinement on Thin Film Evaporation	28
2.1 Background	28
2.2 Motivation and Scopes of the Present Work	31
2.3 Experimental Procedure	31
2.4 Results and Discussion.....	38
2.5 Summary.....	43
Chapter 3 Stress-Localized Durable Antibiofouling Surfaces.....	45
3.1 Background	46
3.2 Motivation and Scope of the Present Work	48
3.3 Sample Preparation	48
3.4 Biofouling Assays	52
3.4.1 Settlement of <i>Ulva</i> Zoospores.....	52
3.4.2 Attachment and Adhesion of Bacterium <i>C. lytica</i> and Diatom	

<i>Navicula</i>	52
3.4.3 Attachment and Adhesion of Hard Macrofouling Barnacle and Mussel.....	53
3.5 Statistical Analysis.....	54
3.6 Results and Discussion.....	54
3.6.1 Bio-friendly Characteristics.....	54
3.6.2 Ulva Attachment.....	55
3.6.3 Attachment and Adhesion of Marine Bacterium, <i>C. lytica</i>	57
3.6.4 Attachment and Adhesion of Diatom <i>Navicula</i>	59
3.6.5 Attachment and adhesion of Barnacle.....	63
3.6.6 Attachment and Adhesion of Mussel.....	64
3.6.7 Durability Test.....	65
3.7 Summary.....	67
References.....	69

List of Figures

Figure 1.1	Physics of evaporation. The maximum evaporation occurs at the thin film region.3	3
Figure 1.2	Scanning electron microscopy and heat flux vs. wall superheat of (a) micropillars, (b) bi-porous structure of different arrangement of pin fin arrays, (c) silicon nanowires, and (d) biporous CNT strip and pillar forests.4	4
Figure 1.3	Fabrication process of (a) silicon micropillars, (b) Silicon nanowires (SiNWs), and (c) Chemical vapor deposition (CVD) growth of CNTs.....8	8
Figure 1.4	SEM images and heat flux curves as a function of wall superheat for (a) hierarchical structure of micopost wicks, (b) a metal foam on top of a micropost wicks, (c) sintered powder wicks, and (d) copper coated CNTs on a sintered powder wicks substrate.....11	11
Figure 1.5	Fabrication steps of (a) micropost wicks, (b) a metal foam on top of a micropost wicks, and (c) two-layer sintered powder wicks structure separated by micropost wicks array.....12	12
Figure 1.6	(a) SEM top view and schematic of Anodic Aluminum Oxide membranes (AAO). The heat flux has plotted corresponding to the wall superheat. (b) Schematic and heat flux of thin film boiling and evaporation mechanism.14	14
Figure 1.7	SEM image and attained CHF for (a) Si ₃ N ₄ porous membrane, and (b) supported ultra-thin porous membrane on microchannels. Fabrication process for aforementioned structures are presented in figure (c) and (d) respectively.....14	14
Figure 1.8	(a) SEM image of copper inverse opals and a schematic of boiling mechanism inside the IO porous structure. (b) The fabrication process of IOs. (c) Heat transfer performance against the wall superheat. (d) Capillary limit and boiling limit as a function of wicking length for different neck diameters.....19	19
Figure 1.9	(a) Mono and (b) biporous structures of sintered copper powder wicks structure. Heat transfer performance were displayed as a function of wall superheat.....20	20
Figure 1.10	(a) SEM, schematic, and heat flux vs. wall superheat of (a) conformal porous copper coated CVD grown diamond microchannels, (b) multilayered copper meshes, and (c) hybrid structure composed of bonded copper mesh on	

	microchannels.....	22
Figure 1.11	Fabrication process of (a) conformal copper coated CVD grown diamond microchannels and (b) multilayered copper mesh wicks with different roughness on the surface.....	23
Figure 1.12	Schematic and dissipated heat of (a) a hybrid nanochannel, (b) a nanochannel-nanopore hybrid structure, and (c) a nanochannel with a capillary pumping between hot and cold reservoir.....	26
Figure 1.13	Microfabrication method of (a) hybrid nanochannels with different height for test and reference chamber, (b) hybrid nanochannel-nanopore structure, (c) nanochannels with two reservoirs.....	27
Figure 2.1	SEM images of (a) top view, (b) tilted view, and (c) cross-sectional view.....	32
Figure 2.2	AFM image of AAO membrane with pore diameter of 20 nm.....	32
Figure 2.3	(a) SEM of AAO membrane (b) Pore distribution on AAO membrane characterized by Image J and (c) Pore distribution graph	33
Figure 2.4	Two ports of Multimeter are connected to the copper electrodes to measure the Pt heater resistance with a K-type thermocouple attached to 1 mm above of the membrane for reading temperatures. The whole setup is placed in a convective oven.	34
Figure 2.5	Platinum resistance changes vs. temperature.....	34
Figure 2.6	Attachment of AAO membrane on PTFE holder.....	36
Figure 2.7	Schematic of experimental setup.....	36
Figure 2.8	Experimental setup including stainless-steel vapor chamber, liquid chamber, water degassing platform, and water delivery system consisting of syringe and syringe pump	37
Figure 2.9	Conduction heat loss as a function of heater surface temperature.....	38
Figure 2.10	Transition in heat transfer mechanism on AAO membrane starting from (a) single phase convection to (b-d) pool boiling, (c) thin film boiling, and finally (d)	

	dryout.....	39
Figure 2.11	Dryout area and hot spots locations appeared on the membrane surface after reaching CHF.....	40
Figure 2.12	(a) Heat flux vs. wall superheat, and (b) Heat transfer coefficient as a function of heat flux.....	42
Figure 2.13	Wall superheat and heat flux incensement for mass flux of (a-b) 17 ml/min, (c-d) 15 ml/min, and (e-f) 5 ml/min.....	43
Figure 3.1	(a) and (b) Schematic of water flow including marine organisms (diatom <i>Navicula</i> , <i>Ulva</i> spores, bacterium, Mussels, and barnacles from left to right) over stress-localized coatings and its anti-biofouling property	51
Figure 3.2	(a) Schematic of experimental setup to exhibit stress-localization mechanism. (b) Interfacial cavities formed at phase II coordinate due to their low shear modulus. (c) The geometrical parameters in surface adhesion measurements.....	51
Figure 3.3	Assessment of leachate toxicity of ABF coatings and state-of-the-art coatings for (a) bacterium <i>C. lytica</i> after 24 hrs, and (b) diatom <i>Navicula</i> after 48 hrs. Error bars represent one standard deviation of the mean.the membranes. PMMA polymerization area is pointed on each membrane...55	
Figure 3.4	SPM analysis of <i>Ulva</i> on ABF coating showing (a) height graph, (b) adhesion, (c) deformation, and (d) elasticity modulus. <i>Ulva</i> spores attachment has been compared between (e) PDMS control sample and (f) ABF1.....	57
Figure 3.5	(a) Bacterial biofilm growth after 24 hours for ABF coatings, Silastic T2, Intersleek 700, and Polyurethane (PU). (b) Comparison of surface coverage for ABF and Intersleek 700. (c) Graphical representation of bacterial attachment on the coatings.....	58
Figure 3.6	(a) Biofilm removal by exposing to water jet for two different pressures of 10 psi and 20 psi. (b) Remained biomass after exposure to water jet. Error bars represent one standard deviation of the mean.....	59
Figure 3.7	Diatom attachment and EPS formation on the surface of ABF3. (a) Height, (b) deformation, (c) adhesion, and (d) modulus of elasticity of diatom and EPS. Diatom attachment has been compared between (e) PDMS control sample and (f) ABF3.....	61

Figure 3.8	Diatom attachment measured after 2 hours and biofilm growth after 48 hours of incubation. The fluorescence values present concentration of diatoms attached to the coatings and biofilm growth on the surface. Error bars represent one standard deviation of the mean.....	62
Figure 3.9	(a) Diatom <i>Navicula</i> removal by exposing to water jet for 10 seconds for two different pressures of 10 psi and 20 psi. (b) Remained biomass after exposure to water jet. Error bars represent one standard deviation of the mean.	63
Figure 3.10	Assessment of barnacles (a) reattached efficiency after 2 weeks of daily feedings of brine shrimp, and (b) reattached adhesion on ABFs, Intersleek 700, and standard sample (polysiloxane). Error bars represent one standard deviation of the mean.....	64
Figure 3.11	(a) Evaluation of mussel attachment on ABF and Intersleek 700 coatings. (b) Required force to remove the mussels from the surface after measuring the attachment efficiency in (a). Error bars represent one standard deviation of the mean.....	65
Figure 3.12	(a) Mechanical durability test of ABF3 (25% of phase (II)). (b) Different range of pH from 1.1 to 13.1 for chemical durability test. (c) UV test for 2000 hours. (d) On-field reparability. The scale bar is 10 mm.....	66
Figure 3.13	Abrasion test results for ABF coatings and PDMS. Primary thickness of each sample is 300 μm . PDMS sample has considered as the standard sample. ABF 3 with lowest concentration of organogels shows the best mechanical durability.....	67

List of Figures

Figure 1.1	Physics of evaporation. The maximum evaporation occurs at the thin film region.3	3
Figure 1.2	Scanning electron microscopy and heat flux vs. wall superheat of (a) micropillars, (b) bi-porous structure of different arrangement of pin fin arrays, (c) silicon nanowires, and (d) biporous CNT strip and pillar forests.4	4
Figure 1.3	Fabrication process of (a) silicon micropillars, (b) Silicon nanowires (SiNWs), and (c) Chemical vapor deposition (CVD) growth of CNTs.....8	8
Figure 1.4	SEM images and heat flux curves as a function of wall superheat for (a) hierarchical structure of micopost wicks, (b) a metal foam on top of a micropost wicks, (c) sintered powder wicks, and (d) copper coated CNTs on a sintered powder wicks substrate.....11	11
Figure 1.5	Fabrication steps of (a) micropost wicks, (b) a metal foam on top of a micropost wicks, and (c) two-layer sintered powder wicks structure separated by micropost wicks array.....12	12
Figure 1.6	(a) SEM top view and schematic of Anodic Aluminum Oxide membranes (AAO). The heat flux has plotted corresponding to the wall superheat. (b) Schematic and heat flux of thin film boiling and evaporation mechanism.14	14
Figure 1.7	SEM image and attained CHF for (a) Si ₃ N ₄ porous membrane, and (b) supported ultra-thin porous membrane on microchannels. Fabrication process for aforementioned structures are presented in figure (c) and (d) respectively.....14	14
Figure 1.8	(a) SEM image of copper inverse oplas and a schematic of boiling	

	mechanism inside the IO porous structure. (b) The fabrication process of IOs. (c) Heat transfer performance against the wall superheat. (d) Capillary limit and boiling limit as a function of wicking length for different neck diameters.....	19
Figure 1.9	(a) Mono and (b) biporous structures of sintered copper powder wicks structure. Heat transfer performance were displayed as a function of wall superheat.....	20
Figure 1.10	(a) SEM, schematic, and heat flux vs. wall superheat of (a) conformal porous copper coated CVD grown diamond microchannels, (b) multilayered copper meshes, and (c) hybrid structure composed of bonded copper mesh on microchannels.....	22
Figure 1.11	Fabrication process of (a) conformal copper coated CVD grown diamond microchannels and (b) multilayered copper mesh wicks with different roughness on the surface.....	23
Figure 1.12	Schematic and dissipated heat of (a) a hybrid nanochannel, (b) a nanochannel-nanopore hybrid structure, and (c) a nanochannel with a capillary pumping between hot and cold reservoir.....	26
Figure 1.13	Microfabrication method of (a) hybrid nanochannels with different height for test and reference chamber, (b) hybrid nanochannel-nanopore structure, (c) nanochannels with two reservoirs.....	27
Figure 2.1	SEM images of (a) top view, (b) tilted view, and (c) cross-sectional view.....	32
Figure 2.2	AFM image of AAO membrane with pore diameter of 20 nm.....	32

Figure 2.3	(a) SEM of AAO membrane (b) Pore distribution on AAO membrane characterized by Image J and (c) Pore distribution graph33
Figure 2.4	Two ports of Multimeter are connected to the copper electrodes to measure the Pt heater resistance with a K-type thermocouple attached to 1 mm above of the membrane for reading temperatures. The whole setup is placed in a convective oven.34
Figure 2.5	Platinum resistance changes vs. temperature.....34
Figure 2.6	Attachment of AAO membrane on PTFE holder.....36
Figure 2.7	Schematic of experimental setup.....37
Figure 2.8	Experimental setup including stainless-steel vapor chamber, liquid chamber, water degassing platform, and water delivery system consisting of syringe and syringe pump37
Figure 2.9	Conduction heat loss as a function of heater surface temperature.....38
Figure 2.10	Transition in heat transfer mechanism on AAO membrane starting from (a) single phase convection to (b-d) pool boiling, (c) thin film boiling, and finally (d) dryout.....40
Figure 2.11	Dryout area and hot spots locations appeared on the membrane surface after reaching CHF.....40
Figure 2.12	(a) Heat flux vs. wall superheat, and (b) Heat transfer coefficient as a function of heat flux.....42
Figure 2.13	Wall superheat and heat flux incensement for mass flux of (a-b) 17 ml/min,

	(c-d) 15 ml/min, and (e-f) 5 ml/min.....	44
Figure 3.1	(a) and (b) Schematic of water flow including marine organisms (diatom <i>Navicula</i> , <i>Ulva</i> spores, bacterium, Mussels, and barnacles from left to right) over stress-localized coatings and its anti-biofouling property	52
Figure 3.2	(a) Schematic of experimental setup to exhibit stress-localization mechanism. (b) Interfacial cavities formed at phase II coordinate due to their low shear modulus. (c) The geometrical parameters in surface adhesion measurements.....	52
Figure 3.3	Assessment of leachate toxicity of ABF coatings and state-of-the-art coatings for (a) bacterium <i>C. lytica</i> after 24 hrs, and (b) diatom <i>Navicula</i> after 48 hrs. Error bars represent one standard deviation of the mean.the membranes. PMMA polymerization area is pointed on each membrane...56	
Figure 3.4	SPM analysis of <i>Ulva</i> on ABF coating showing (a) height graph, (b) adhesion, (c) deformation, and (d) elasticity modulus. <i>Ulva</i> spores attachment has been compared between (e) PDMS control sample and (f) ABF1.....	58
Figure 3.5	(a) Bacterial biofilm growth after 24 hours for ABF coatings, Silastic T2, Intersleek 700, and Polyurethane (PU). (b) Comparison of surface coverage for ABF and Intersleek 700. (c) Graphical representation of bacterial attachment on the coatings.....	59
Figure 3.6	(a) Biofilm removal by exposing to water jet for two different pressures of 10 psi and 20 psi. (b) Remained biomass after exposure to water jet. Error bars represent one standard deviation of the mean.....	60
Figure 3.7	Diatom attachment and EPS formation on the surface of ABF3. (a) Height,	

	(b) deformation, (c) adhesion, and (d) modulus of elasticity of diatom and EPS. Diatom attachment has been compared between (e) PDMS control sample and (f) ABF3.....	62
Figure 3.8	Diatom attachment measured after 2 hours and biofilm growth after 48 hours of incubation. The fluorescence values present concentration of diatoms attached to the coatings and biofilm growth on the surface. Error bars represent one standard deviation of the mean.....	63
Figure 3.9	(a) Diatom <i>Navicula</i> removal by exposing to water jet for 10 seconds for two different pressures of 10 psi and 20 psi. (b) Remained biomass after exposure to water jet. Error bars represent one standard deviation of the mean.	64
Figure 3.10	Assessment of barnacles (a) reattached efficiency after 2 weeks of daily feedings of brine shrimp, and (b) reattached adhesion on ABFs, Intersleek 700, and standard sample (polysiloxane). Error bars represent one standard deviation of the mean.....	65
Figure 3.11	(a) Evaluation of mussel attachment on ABF and Intersleek 700 coatings. (b) Required force to remove the mussels from the surface after measuring the attachment efficiency in (a). Error bars represent one standard deviation of the mean.....	66
Figure 3.12	(a) Mechanical durability test of ABF3 (25% of phase (II)). (b) Different range of pH from 1.1 to 13.1 for chemical durability test. (c) UV test for 2000 hours. (d) On-field reparability. The scale bar is 10 mm.....	68
Figure 3.13	Abrasion test results for ABF coatings and PDMS. Primary thickness of each sample is 300 μm . PDMS sample has considered as the standard sample. ABF 3 with lowest concentration of organogels shows the best	

mechanical	
durability.....	68

Chapter 1: Introduction

1.1 Background

The demands for higher performance and computing power have led to continuous shrinking of electronic devices at the cost of increasing power density. Heat removal in a reliable, efficient, and uniform fashion has thus become a limiting design parameter. Thin film evaporation has attained a rapid growth of interest for thermal management solution due to the privilege of its high heat removal capacity¹⁻⁸. Liquid-vapor phase change has also served in a multitude applications including novel methods of water harvesting⁹, water desalination¹⁰⁻¹², humidification¹³, steam generation cycles¹⁴⁻¹⁶, biology¹⁷⁻¹⁹, agriculture^{20,21}, food and chemical processing industries^{22,23}. The importance of thin film evaporation has motivated researchers to continually develop new and ever-improving materials, processes, and design methodologies.

Evaporation from thin films as a key process of many two-phase cooling strategies have attracted great attention over the past half-century. Deep understanding of the physics of the phenomena associated with enhancing heat transfer efficiency have caused a very challenging set of circumstances. However, the extensive theoretical and experimental studies have revealed new understanding of the nature of solid-liquid-vapor interactions at the contact line and interfacial heat and mass fluxes²⁴⁻²⁹. Evaporation happens across a liquid-vapor interface which is called transition region where drives the liquid molecules into the vapor phase^{30,31}. The occurred phase change is governed by transport processes at the contact line which significantly depend on wettability and surface energy^{32,33}, thermal resistances^{34,35}, hydrodynamic resistances²⁸, and capillary wicking³⁶⁻⁴⁰. Moreover, heat transfer coefficient^{41,42}, disjoining pressure^{43,44}, and surface

tension gradient⁴⁵ have been reported in the literature as influencing evaporation parameters. In general, increased solid-liquid interface as well as increased number of nucleation sites for liquid vaporization dictate the enhancement of critical heat flux and wall superheat⁴⁶. Wall superheat is defined as the difference between surface temperature and the saturation temperature. To form liquid-vapor and solid-liquid interfaces, it is required to overcome the surface energies that is related to the wetting nature of the substrate⁴⁷. It has been well documented that surface wettability can be modified by chemical compositions and surface morphology. Micro/nano fabrication technique has been emerged as potential means of increasing evaporation through manipulation of wettability behavior of the surface. With the knowledge of determinant thin-film evaporation factors and advances in materials and surface engineering methods, now more than ever there are opportunities for novel methods to address thermal management challenges.

Micro/nano architectures have been studied extensively as model systems to understand influences of topography on wetting behavior and consequently on critical heat flux (CHF) limit. The objective of this chapter is to identify the fundamental governing mechanisms of evaporation in various tailored micro/nano structures including micropillars and nanowires, nanoporous membranes, hierarchical structures, sintered nanoparticles, and micro/nano channels. A comparison between thermal conversion efficiencies has also presented to provide a comprehensive study.

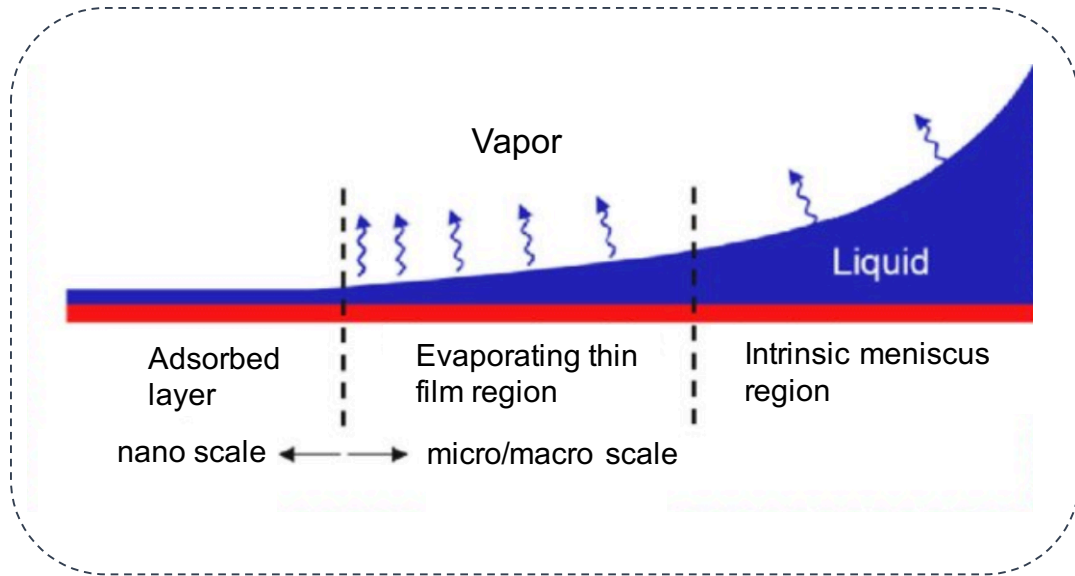


Figure 1.1 Physics of evaporation. The maximum evaporation occurs at the thin film region. Reprinted with permission from REF 48, American Chemical Society.

1.2 Micropillars/Nanowire

The enhancement of thin film evaporation significantly depends on the extension of liquid-vapor interface at the three-phase contact line. The extended meniscus can be achieved through micro/nano-structuring by varying the surface area-to-volume ratio. Moreover, micro/nano engineering of a surface significantly improves the liquid transport via capillary wicking^{49,50}. Higher capillary wicking capability of a structure postpones the liquid dry out that occurs when viscous forces overcome the capillary pressure. Therefore, tremendous efforts have been taken to understand how to manipulate the hydrodynamic characteristics of a working fluid and its interfacial interactivity. Micropillars and nanowires with high surface roughness greatly expand the interfacial contact area besides their improved wickability⁵¹⁻⁵⁴. It is demonstrated that desired performance of wick structures for fluid and thermal transport depend on various

parameters including extended menisci, capillary, permeability, porosity, and characteristic lengths.

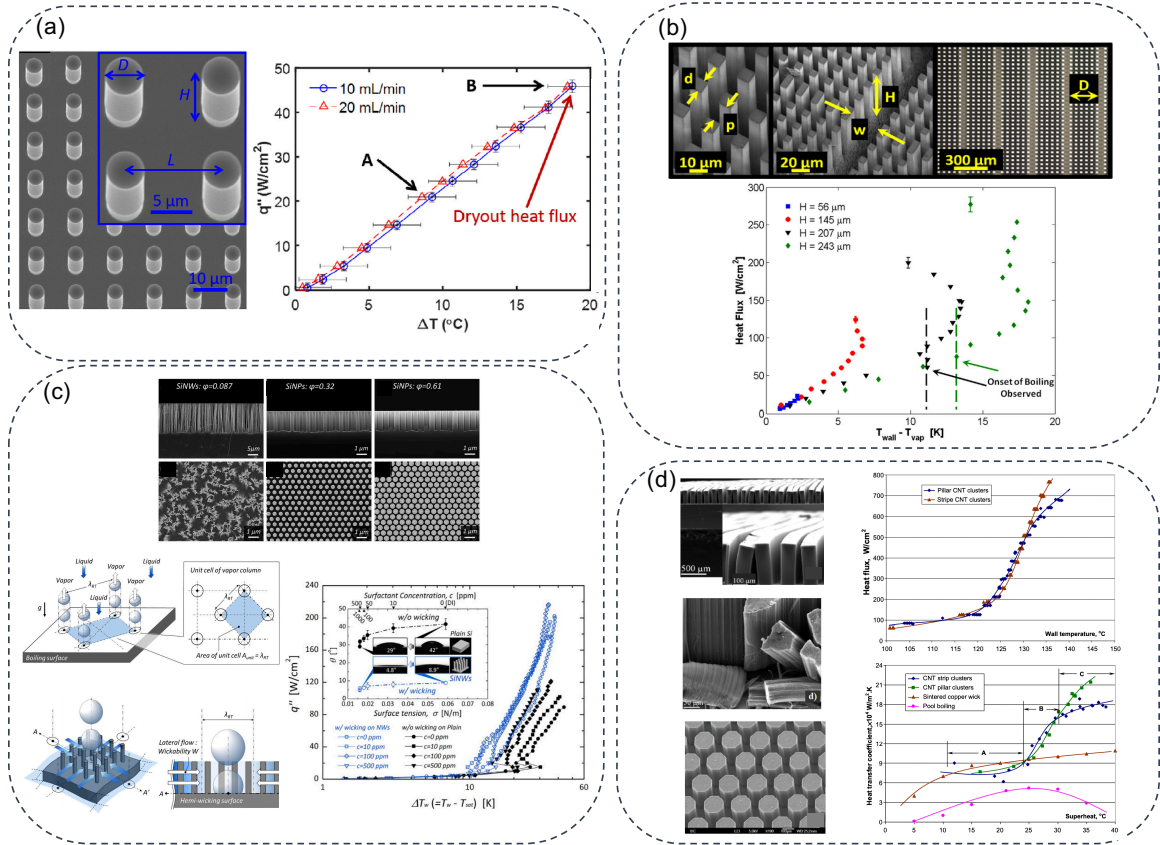


Figure 1.2 (a) micropillars, reprinted with permission from REF. 55, ELSEVIER (b) bi-porous structure of different arrangement of pin fin arrays, reprinted with permission from REF. 61, ASME. (c) silicon nanowires, reprinted with permission from REF. 63, Nature. (d) biporous CNT strip and pillar forests, reprinted with permission from REF. 69, ELSEVIER.

Adera et al.⁵⁵ experimentally characterized thin film evaporation from a $1 \times 1 \text{ cm}^2$ silicon micropillars and used a semi-analytical model to find the optimum design to maximize the heat dissipation. For silicon micropillars fabrication a standard photolithography and deep-reactive-ion etching (DRIE) process have been used. The final structure has been illustrated in Figure 1.2a showing diameter, height, and center to center distance of pillars. In this experimental study, pure evaporation was analyzed

without interfering any nucleation boiling. This achieved by applying a passive liquid transport utilizing a two-reservoir design. The passive transport strategy prevents flooding on the structure while wicks enough water to sustain the evaporation. The transferred heat through the silicon micropillar with high thermal conductivity triggers the evaporation on the top of pillars where the liquid meniscus is formed. The evaporation fluxes were presented against the temperature difference between the substrate wall and the saturation temperature of chamber in Figure 1.2a. The unaffected dry out heat flux and temperature by changing the flow rate from 10 to 20 ml/min from canister to reservoirs prove that capillary wicking is the only liquid transport mechanism in this structure. By increasing heat flux, the liquid meniscus adjusts its curvature in a way to counteract for the mass loss through the evaporation. This dynamic change in curvature continues to the point that it starts to recede due to the dominant effect of viscous forces vs. capillary wicking. This is known as capillary-limited dryout heat flux. The effect of spacing and diameter of pillars on the capillary-limited dryout heat flux is also investigated.

As shown in many experimental studies, thin film evaporation can be coupled with nucleation boiling. It is important to note that in evaporation and boiling regime how to increase both heat dissipation and heat transfer coefficient (HTC) simultaneously. It is known that capillary wicking enhances by increased surface area in wicks structure, but it may lead to higher viscous forces which results in lower heat transfer coefficient. So, there is an optimum design to favor both heat dissipation and heat transfer coefficient⁵⁶. Different numerical approaches were utilized to model thin-film evaporation on wick structures for an optimized design^{39,57-60}. Coso et al⁶¹. has presented a silicon biporous

wick structured made of periodically pin fin arrays separated in a microchannel. A schematic of fabrication process of evaporator wick was depicted in Figure 1.3a showing the sequential steps of photolithography and DRIE. Heater and copper electrode deposition has also been illustrated. In this evaporator design, the reduced thickness of liquid film in addition to enhanced capillary improves efficiency of heat dissipation. Heat dissipation has been measured for different arrangement of wick parameters including diameter, length, and microchannel width. As it is represented in Figure 1.2b, for pins with a height of less than $145\mu\text{m}$, heat transfer mechanism is in pure evaporation and it enters the boiling regime as height increases (Figure 1.2b). In the boiling regime, higher heat fluxes were dissipated at lower wall superheats due to enhanced thin film area generated by bubbles motion along the pins. The thickness of this film is a function of the space between pins and the bubbles velocity. As heat flux elevates, the liquid contact angle on the wall of pins reaches its minimum and further the liquid film thickness decreases. The increased thermal conductivity as a consequence of reduced film thickness and enhanced evaporation interface prior to the dry out, are the roots for high heat transfer coefficient. The effects of diameter and pitch have also been demonstrated for both evaporation and boiling regimes. Dual-height superhydrophilic (DHS) micro-post evaporator wicks are also fabricated by Ryo et al.⁶² to vertically stretch the thin evaporative film and increase the heat flux.

Micro/nano surface roughening has a significant contribution in enhancement of CHF by reinforcing interfacial re-wetting. Kim et al.⁶³ fabricated silicon nanowires to compare their performance with plain silicon substrate. As it is depicted in Figure 1.2c, the interaction between rewetting down flowing fluid and up flowing vapor governs the

heat transfer mechanism. Moreover, it is shown how nanowires intrigues the fluid transport through strong interfacial wicking caused by induced capillary pressure on engineered surface. Advanced capillary pressure allows for dissipation of higher heat fluxes with delivering more liquid to the boiling surface. Silicon nanowires take advantage of separate pathways for fluid and vapor to reach CHF with lower wall superheat as the comparison with a plain silicon surface (Figure 1.2c). At the final stage, the lack of stability between fluid resistance and vapor hydrodynamic (Helmholtz instability) leads to formation of a vapor blanket and finally burnout occurs. The effect of porosity and length of SiNWs have also been investigated on CHF and HTC value. Figure 1.3b displays the fabrication method of silicon nanowires arrays⁶⁴⁻⁶⁶.

Carbon nanotubes (CNTs) as a class of nano scale wick structure has received enormous amount of attention due to their high porosity and fast fluid transport capability. Moreover, a high thermal conductivity from 0.7 to 262 W/m.K^{67,68} can be achieved by tuning synthesis conditions of CNTs growth. An experimental study on bi-porous wick CNT strip forests and CNT pillar forests was conducted by Cai et al.⁶⁹ to measure the evaporation on these porous nano structures (Figure 1.2d). Although CNTs can provide a very high capillary pressure up to two orders of magnitude bigger than micro wicks, but their in-plane permeability is one to two orders of magnitudes smaller. To overcome this challenge, a bi-porous structure with micro pitches between CNT clusters has been shaped. With the presence of micro pitch, the liquid flow resistance decreases while capillary is highly increased in the nanopores of CNT clusters. As results indicate in Figure 1.2d, the transition from evaporation to nucleate boiling occurs at almost the same superheat for both structures. A maximum heat flux of 770 W/cm² and

600 W/cm² with a superheat of less than 40 °C has been achieved for stripe and pillar configurations, respectively. The privilege of nano porous CNT structures can be seen more clearly in heat transfer coefficient graph especially when evaporation enters the nucleate boiling regime and fully developed phase change is formed (region B). In the fully developed regime, increased evaporation interface and vapor jets in the large pores facilitate the heat dissipation mechanism. At high heat fluxes, the heat transfer coefficient is governed by thin liquid film conduction since it reaches its minimum conduction resistance at this region. Chemical vapor deposition (CVD) as a common method for synthesis of vertically aligned carbon nanotubes^{70,71} (VACNT) has been shown in Figure 1.3c.

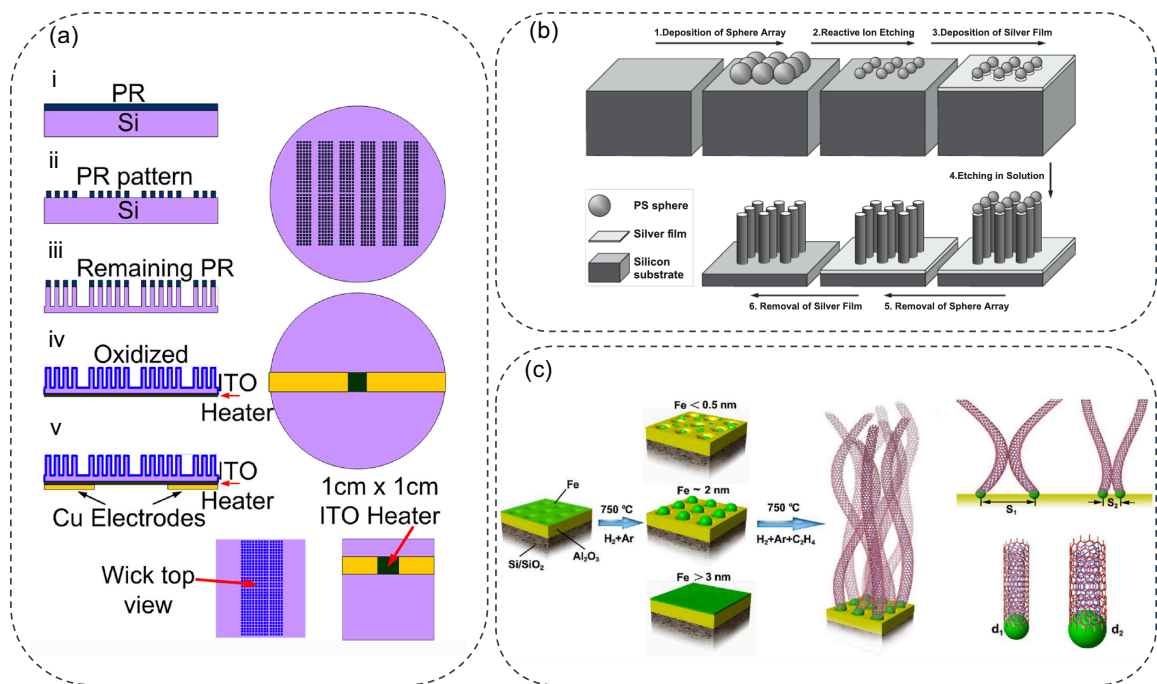


Figure 1.3. Fabrication process of (a) silicon micropillars, reprinted with permission from REF. 61, ASME. (b) Silicon nanowire (SiNWs), reprinted with permission from REF. 64, Wiley. (c) Chemical vapor deposition (CVD) growth of CNTs, reprinted with permission from REF. 70, ELSEVIER.

1.3 Hierarchical Structures

A number of studies have reported the privilege of hierarchical surfaces with increased surface roughness to enhance the HTC and CHF⁷². Hierarchical structures with two or more distinct pore sizes have been proposed as alternative geometries to boost the capillary limit^{73–75}. Nam et al.⁷⁶ have fabricated and analyzed heat transfer performance of dense arrays of superhydrophilic micro-post shown in Figure 1.4a. The solid fraction of micro-posts arrays is up to 50% with an aspect ratio of two. The fabrication process of Cu micro-porous wicks has been presented in Figure 1.5a. A seed layer of (Ti/Cu/ Ti) has been deposited on a silicon substrate using e-beam thermal evaporation. In the next step, the negative PR has been coated on the adhesive layer and patterned as mold for micro-post wicks. Then, the Cu wicks have formed utilizing electrodeposition under non-uniform current leading to discrete CuO nanostructures on a thin (< 200 nm) Cu_2O underlayer. In the last step, the PR mold has been completely removed after plating process⁷⁷. Chemical oxidization process results in achieving high surface energy and wettability without introducing large parasitic thermal resistance. Nam et al.⁷⁶ have characterized the heat transfer performance of Cu micro-post wicks and results are displayed in Figure 1.4a. The maximum heat flux of almost 200 W/cm^2 has been achieved for a heater size of $5 \times 5 \text{ mm}^2$ and it increases up to 950 W/cm^2 for a smaller heater size ($2 \times 2 \text{ mm}^2$). Increased heater area resulted in decreased heat flux in microstructures for phase change heat transfer due to the longer distance for liquid transport. D_p , D_{cc} , and f_s are representatives of diameter of the post, distance between the nearest neighboring posts, and solid fraction. Nam et al.⁷⁸ have further investigated the wicking behavior of different types of nanostructured copper surfaces for both water and

methanol. Integration of a nanostructured metal foam layer on top of the copper micro-post wicks enhanced the heat flux over 150% for micro-post wicks of ~ 0.4 solid fraction⁷⁹ (Figure 1.4b). This improvement caused by high permeability of liquid supply in addition to high capillary pressure of wicks. The fabrication approach is depicted in Figure 1.5b. Another configuration of evaporator wicks was introduced and studied by Sudhakar et al.⁸⁰ The wicks structure is made of two layer sintered porous copper with an array of posts bridging the two layers as shown in Figure 1.5c. A maximum heat flux of 485 W/cm^2 was achieved with a small superheat of 25°C for the optimized wicks with Cu particles of diameter $180\text{-}212 \mu\text{m}$ and 15×15 number of arrays (Figure 1.4c). As heat flux increases, the thermal resistance decreases until the two layer holds a near constant resistance in a heat flux above $\sim 240 \text{ W/cm}^2$. At this point, the liquid retreats into the cap layer through the wicks which defines a separate path for liquid and vapor. The high heat flux is a result of both high capillary pressure and low thermal resistance in the two-layer structure. The calculated thermal resistance was 0.052 K/W at the dryout point and stayed below 0.09 K/W during the whole process. The requirements to achieve high CHF in wicks structures make the carbon nanotubes as a decent candidate due to the high thermal conductivity and capillary pressure in them. In a work by Kousalya et al.⁸¹ CNTs were fabricated on a sintered copper substrate with plasma enhanced chemical vapor deposition technique. Then, a thin layer of copper was deposited on CNTs through physical vapor deposition method. Three different copper coating thicknesses were deposited and investigated including 250 nm , 500 nm , 750 nm . Results compared the CNTs copper coating performance with bare copper sintered powder and different copper coating thicknesses (Figure 1.4d). Following the heat flux curve, it can be observed that

at low heat fluxes ($<50\text{W/cm}^2$), heat transfer is in thin-film evaporation regime with a relatively low superheat. By further incensement of heat flux (between 50 and 350 W/cm^2), capillary pressure in the pores assists the liquid flow to the heated area to replenish the evaporated liquid in the dominant boiling heat transfer region. Reduced slope of boiling curve represents a decrease in HTC that leads to partial dryout and finally complete dryout. The presence of CNTs reasons a faster transition from evaporation to boiling at lower superheat. The highest CHF as well as lower superheat were attained for thicker copper coatings. This enhancement is owing to reduced thermal resistance and increased capillary pressure of coated carbon nanotubes.

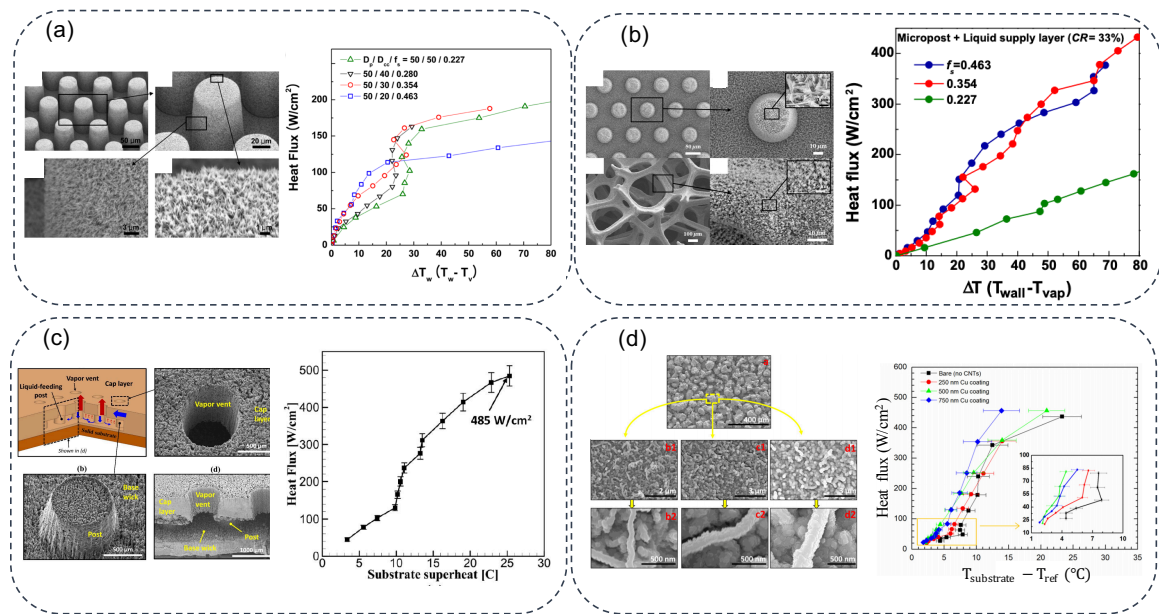


Figure 1.4 (a) hierarchical structure of micro-post wicks, reprinted with permission from REF. 76, ASME. (b) a metal foam on top of a micro-post wicks, reprinted with permission from REF. 79, ELSEVIER. (c) sintered powder wicks, reprinted with permission from REF. 80, ELSEVIER. (d) copper coated CNTs on a sintered powder wicks substrate, reprinted with permission from REF. 81, ELSEVIER.

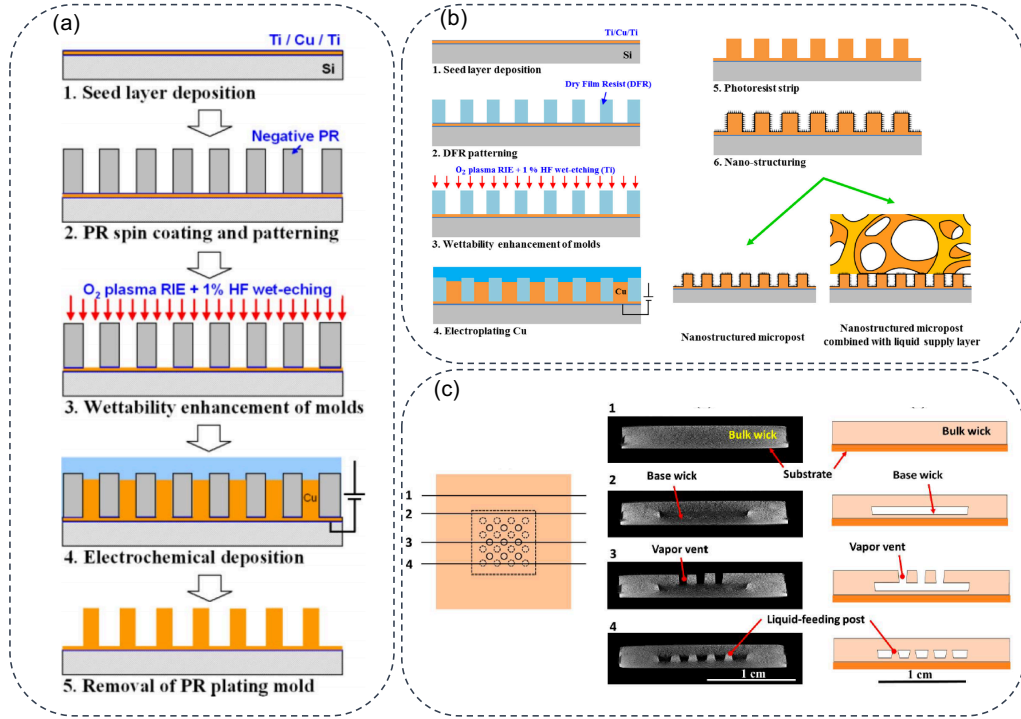


Figure 1.5 Fabrication steps of (a) micro-post wicks, reprinted with permission from REF. 77, IEEE. (b) a metal foam on top of a micro-post wicks, reprinted with permission from REF. 79, ELSEVIER. (c) two-layer sintered powder wicks structure separated by micro-post wicks array, reprinted with permission from REF. 80, ELSEVIER.

1.4 Thin Membranes

Thin film evaporation from nanoporous membranes has received a great deal of investigations due to their promising performances. A short distance for liquid to pass gives the privilege of low thermal resistance leading to a high evaporation flux and high frequency bubble departure in thin film boiling regime. Nanoporous membranes are able to provide high capillary pressures while decrease viscous losses due to short pathway⁸². Separate liquid and vapor pathways are known as a great advantage in porous membranes. Figure 1.6a shows an anodic aluminum oxide membrane with pore radii of 28–75 nm and porosities of 0.1–0.35⁸³. In this study, the role of various parameters on

heat transfer performance of AAO membrane including pore diameters (10 nm–200 nm), membrane porosity (0.1–0.35), and meniscus location within the pore have been investigated. A monolayer of perfluorodecyltrichlorosilane was deposited on top of platinum heater (RTD) to make the top side of membrane hydrophobic. The hydrophobic coating pins the meniscus at a specific location. Then, the free standing AAO membrane was placed in contact with water and the hydrophilic nature of the backside of membrane sucks the water inside. The heat transfer curve demonstrates the performance of different membranes which named as pore radius (nm)-Porosity- L^* . L^* is defined as the ratio of pore length to the pore diameter. Dashed lines represent where the transition from flooding regime to pore level evaporation regime happens ($\pi = 1$). For a π less than one, water flooded the membrane surface and when π is more than 1, all the fluid on top of membrane is fully evaporated and capillary pressure must supply the liquid (Figure 1.6b). Transition to the pure evaporation regime has caused an order of magnitude increase in dissipated heat compared with flooded regime. Membranes with higher porosities acquire higher heat fluxes due to more delivered liquid to the evaporation site. The effect of the meniscus location within the pore was investigated for different samples 75-0.35-2, 75-0.35-7, and 75-0.35-15. The results from these samples were compared with the modeling data. It is shown as L^* increases; the evaporative heat flux drops rapidly. As results demonstrated, 1 μm moving of the meniscus caused heat dissipation reduction by a factor of two. This drop in heat flux was due to the added vapor transport resistance through the hydrophobic pore section for generated vapor to escape.

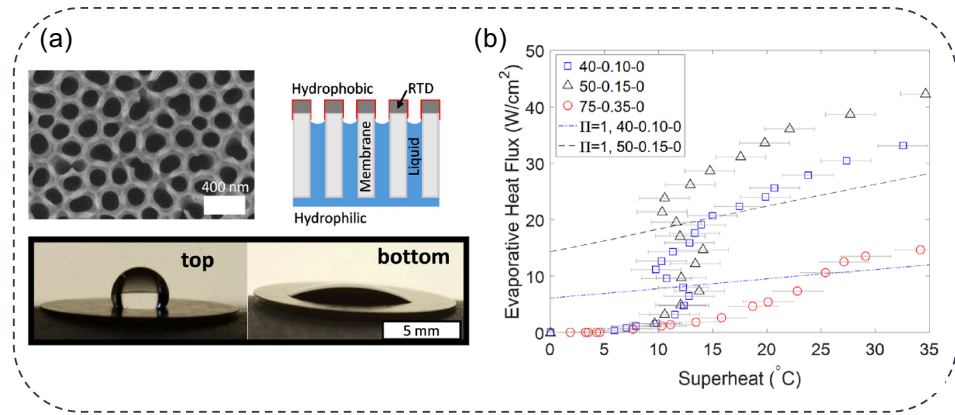


Figure 1.6 (a) SEM top view and schematic of Anodic Aluminum Oxide membranes (AAO). The heat flux has plotted corresponding to the wall superheat. (b) Schematic and heat flux of thin film boiling and evaporation mechanism. Part (a) and (b) are reprinted with permission from REF. 83, Applied Physics Letters.

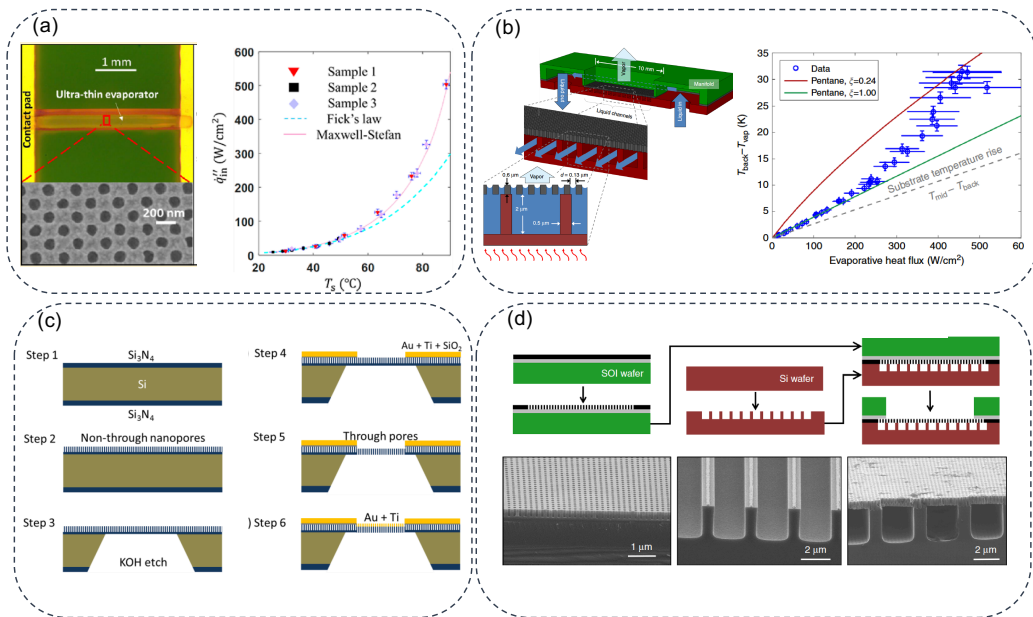


Figure 1.7 (a) Si₃N₄ porous membrane, and (b) supported ultra-thin porous membrane on microchannels. Fabrication process for aforementioned structures is presented in figure (c) and (d) respectively. Part (a) and (c) are reprinted with permission from REF. 84, American Chemical Society. Part (b) and (d) are reprinted with permission from REF. 85, Nature.

Besides the importance of liquid refilling efficiency, minimizing the transport resistance of vapor removal tremendously affects the heat transfer mechanism. In a novel

work presented by Lu et al.⁸⁴ a high heat flux of 500 W/cm^2 was achieved by utilizing an ultrathin nanoporous membrane with a thickness of 200 nm. The fabrication process of the ultrathin Si_3N_4 has been illustrated in Figure 1.7c. The pore radius is 65 nm with an area of $0.26 \text{ mm} \times 3.4 \text{ mm}$ coated with Au as heater as well as resistive temperature detector. The membrane has been experimented in air ambient and depicted high heat flux in pure evaporation regime shown in Figure 1.7a. The small boundary layer thickness assists the high evaporative heat flux transport. As Figure 1.7a depicts, experimental results validate the Maxwell-Stefan equation at high interfacial heat fluxes. Despite of high achieved heat flux, all the three aforementioned experimental studies on ultrathin membranes suffer from the mechanical stability. In a novel design, Hanks et al.⁸⁵ improved the mechanical stability of an ultrathin silicon membrane with the thickness of 600 nm by assembling it on a silicon microchannel. The presence of microchannels that are $2 \text{ }\mu\text{m}$ wide, $2 \text{ }\mu\text{m}$ high, and $200 \text{ }\mu\text{m}$ long with high permeability facilitates the liquid feeding of the nanoporous membrane with pores diameter of 50-100 nm. Within a thin wicking structure, it is possible to achieve a high CFH and HTC by suppressing the nucleate boiling and promoting a steady liquid-vapor interface. In the structure shown in Figure 1.7b, a high heat flux of $\sim 518 \text{ W/cm}^2$ was reached with a superheat of less than $35 \text{ }^\circ\text{C}$ for a dielectric fluid such as pentane with low surface tension of 0.016 N/m and low thermal conductivity of 0.11 W/m.K at $20 \text{ }^\circ\text{C}$. The fabrication process of both silicon membrane and microchannels and following fusion bonding process are displayed in Figure 1.7d. The platinum heater and RTD then deposited on the backside of the structure. The liquid enters the backside of the device and drawn by capillary into the channels that later evaporates from the nanoporous surface. The

excessive liquid bypasses the device and returns back to a flowmeter. The heat transfer performance of the device was tested in an environmental chamber and demonstrated in Figure 1.7b. The experimental data were compared with the results from a model (red and green lines) which anticipated the performance of the evaporator for different confinement of liquid meniscus in the pores. According to the model, the CHF in a capillary-driven structure occurs when the viscous pressure drop in the liquid surpasses the maximum capillary pressure. The maximum capillary pressure across an interface was obtained from the Young-Laplace equation considering a spherical meniscus and a low receding contact angle of 10 degrees for pentane. The gray dashed line in Figure 1.7b represents the thermal resistance through the 650 μm substrate. The red curve displays the situation where the liquid meniscus is confined to the pores, i.e., the liquid area fraction is equal to the porosity, $\xi = 0.242$. The green curve demonstrates when liquid spreading to cover a larger area fraction at the limit of $\xi=1$.

1.5 Isotropic Porous Structures

Isotropic porous structures are known as a diverse category for heat dissipation purposes and has been raised in various forms such as inverse opals, sintered particles, meshes, and etc. The copper inverse opals (IOs) structure as one of the most promising structures was introduced by Zhang et al.⁸⁶ and shown in Figure 1.8a^{28,86,87}. The 3D structure of periodically repeated uniform pores facilitates the liquid and vapor transport through separate pathways. With the emphasis on increasing capillary pressure in wicks structures, the size of pores continues to shrink owing to its inverse proportionality with feature size. At the same time, smaller feature size results in flow resistance increasement which scales inversely with the square of feature size. To achieve both requirements, an

adjustment of pore size is of vital importance. In IOs, the repeated pores were connected to each other through the necks and size of these necks control the hydraulic resistance and consequently fluid transport. Different neck sizes which is a function of sintering time was studied to tailor the permeability of the IOs. Then the permeability was predicted for each neck size by using a finite element model. The calculated permeability for each unit cell with symmetric boundary condition can be a good representative of whole structure due to the well-ordered pore arrangement. When IOs get in contact with water, the capillary wicking in lateral direction wets the porous structure and feeds it. As applied heat transfer increases, the temperature of active area of IOs rises and leads to more intense boiling until it reaches a steady state. The measured dissipated heat fluxes are demonstrated in Figure 1.8c as a function of wall superheat for different neck sintering times. A high heat flux of more than 1200 W/cm^2 was achieved with a small superheat of $12 \text{ }^\circ\text{C}$. To zoom more on the boiling regime in IOs, a schematic of vapor dynamic has been presented in Figure 1.8a displaying an upward movement direction of formed vapor in pores. The vapor passes the IO structure which has a thickness of δ and as it goes up, its pressure drops. By comparing the capillary limit and boiling limit from a model using Darcy's law, their intersection is found as a critical wicking length which below it, boiling performance is not limited by capillary. The vapor departure impedance resulting from drag of wick matrix defines the maximum boiling limit below the critical wicking length. The fabrication process on IOs is shown in Figure 1.8b⁸⁸.

Sintered particles form a diverse category of wicking structures including mono-porous and bi-porous wicks. A mono-porous structure is commonly composed of spherical metal powders such as copper. Various sizes of Cu particles shape wick

structures with different porosity and thickness. The thicker porous layer is, the more conduction resistance will be. Figure 1.9a illustrates a mono-porous sintered wicks and its heat transfer curve against wall superheat. The effect of thickness has been shown for the same powder size (250-335 μm)⁸⁹. For all particle sizes, the thermal resistance is at a maximum for the medium thickness sample and decreases slightly for the 600 and 1200 μm samples. The impact of wick layer thickness on the performance is therefore modest in the thickness range of 600–1200 μm . They also investigated the effect of various powder sizes between 45-335 μm for the same thickness of 900 μm and as results present, higher heat fluxes were attained for powder sizes in the range of 250-335 μm . The maximum heat flux gained for the powder with middle size (106 μm) which suggests there is an optimum size. The balance between available surface area, nucleation sites, permeability, and viscous resistance defines the heat performance of each structure. A schematic of two-phase regime and formed meniscus is demonstrated in Fig. 1.9a. In a study by Semenic et al.⁹⁰ a biporous wicks structure was investigated to further enhance the dissipated heat (Figure 1.9b). Although the heat dissipation mechanism is the same in both mono-porous and biporous wicks, biporous sintered wicks was achieved higher maximum heat flux. The increased evaporative meniscus inside the biporous structure compared with surface evaporation in mono-porous wicks gives rise to the critical heat flux. The comparison is shown in Figure 1.9b. The wicks 3D structure in this study is composed of clusters with a size of $\sim 500 \mu\text{m}$ that are made of sintered small copper particles with a size of $\sim 70 \mu\text{m}$. The liquid feeding is occurred through small pores of clusters by capillary action and vapor moves away from the large pores. Different cases (19 biporous wicks) were investigated to recognize the optimal design of biporous

through changing the particles and cluster sizes, wick thickness, and evaporator areas. The maximum heat flux in the best thin biporous wick had CHF at 520 W/cm^2 with a superheat of $50 \text{ }^\circ\text{C}$, and the best thick biporous wick tested had CHF at 990 W/cm^2 with a superheat of $147 \text{ }^\circ\text{C}$. The main different performance was observed for thin and thick biporous which refers to nucleation regime. Bubble nucleation does not form inside the thin biporous wicks while it occurs inside the thick wicks and produces vapor jets.

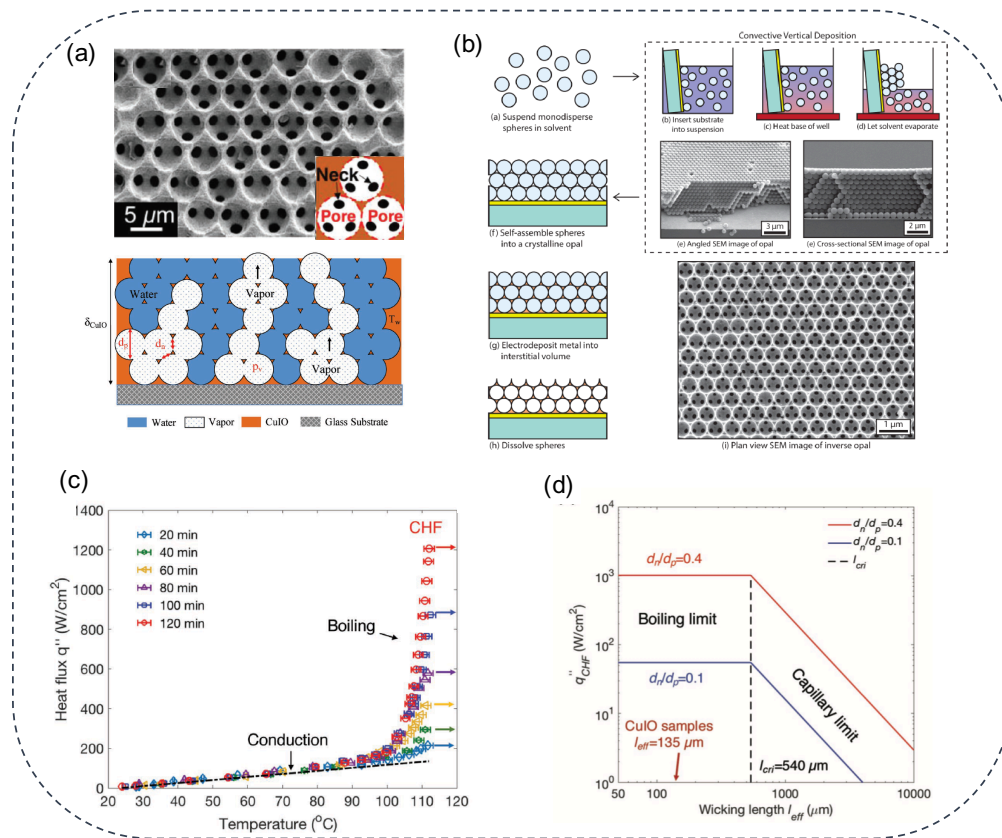


Figure 1.8 (a) SEM image of copper inverse opals and a schematic of boiling mechanism inside the IO porous structure. (b) The fabrication process of IOs. (c) Heat transfer performance against the wall superheat. (d) Capillary limit and boiling limit as a function of wicking length for different neck diameters. All parts are reprinted with permission from REF. 86, Wiley.

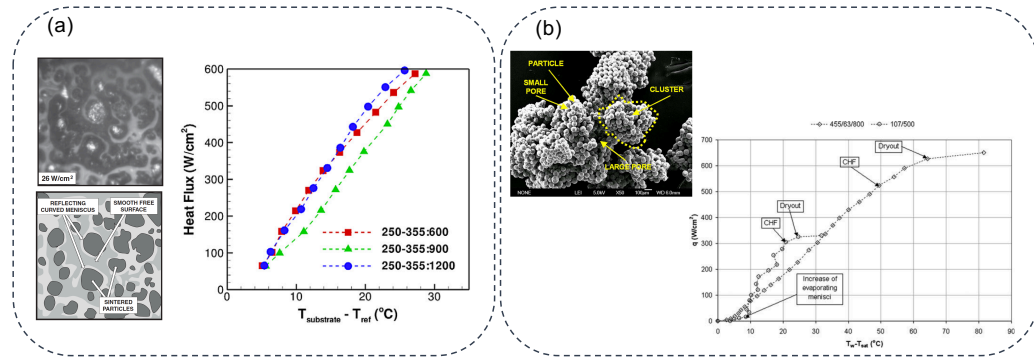


Figure 1.9 (a) Mono and (b) biporous structures of sintered copper powder wicks structure. Heat transfer performance were displayed as a function of wall superheat. Part (a) is reprinted with permission from REF. 89 ELSEVIER. Part (b) is reprinted with permission from REF. 90, ELSEVIER.

1.6 Hybrid Structures

The main porous of hybrid design is to take advantage of two or more various structures at the same time. Enhanced heat transfer is achievable by engineering of all effective parameters such as thermal conductivity, fast liquid transport including both capillary and permeability, separate liquid and vapor pathways, and etc. Considering the aforementioned influencing parameters, Palko et al.⁹¹ has introduced a hybrid structure consisting of a laser etched diamond heat sink coated with conformal, template-fabricated copper microporous (Figure 1.10a). Diamond heat sink spreads the heat aggressively along the triangular channels owing to its very high thermal conductivity. The microporous copper with pore size of 5 μm and thickness of 25 μm provides the optimized liquid and heat transfer. A manifold is responsible for uniform liquid feeding over the heat sink surface. As it is presented in Figure 1.10a, a maximum heat flux of 1280 W/cm^2 with a small superheat of less than 21 K was observed. With a small size of pore (5 μm) boiling forms into thin films with a thickness of less than 35 μm which results

in a high heat transfer coefficient. Small pores and a narrow distribution of them in addition to small thickness promote the uniform bubble nucleation. A cross sectional SEM in Figure 1.10a has been shown. Although small pores of wicks provide high capillary performance, permeability decreases as it scales with the square of pore diameter. To overcome this limitation, a triangular diamond fin base with liquid transport length of 500 μm according to porous copper performance was implemented. Besides the surface extension, the very high thermal conductivity of diamond (1800 W/m. K) boosts the heat spreading. The fabrication process of diamond heat sink is illustrated in Figure 1.11a. The heat transfer mechanism of the composed structure was capable of removing more than 1300 W/cm² with a superheat of less than 35 K (Figure 1.10a). It is also found that flow rate of liquid feeding has a significant effect on single phase contribution in cooling and finally enhances the CHF. The tradeoffs between high wicking flow rate for fluid feeding and low thermal resistance make the design challenging to find the optimized HTC and CHF⁹². To achieve this optimized design, Wen et al.⁹² studied a hybrid mesh structure with nano-grass and microcavities on the multilayer micro-meshes. The microchannels created by woven meshes transport the liquid flow to the microcavities surface. The SEM image of the multilayer copper mesh and the schematic of evaporation mechanism in it is depicted in Figure 1.10b. As it is shown in the schematic, the thin film evaporation happens at the top surface of the multilayer meshes with coupled thin film boiling inside the wicking structure. For wicks with a thickness more than 150 μm , thin film boiling elevates the HTC by disturbing the temperature gradient and reducing the thermal resistance in the thin liquid film. To take advantage of film boiling inside the thick wicks, it is necessary to activate nucleate boiling sites.

Addition of microcavities and nanotextures can be used to increase the number of nucleation sites. The dissipated heat flux was measured for structures with different nucleation sites. The dissipated heat flux was measured for structures with different number of mesh layers and presented in Figure 1.10b. The impact of film boiling can be seen from the small superheat on the surface. Figure 1.10c represents a hybrid structure composed of a sintered copper micromesh bonded on microchannels⁹³. It is found that CHF of the hybrid structure significantly increased by 83% and 198% compared with mono-porous evaporating surfaces such as microchannels and copper woven mesh with the same thickness. This enhancement is due to the separation of capillary pressure and fluid transport. Both micromembrane and microchannels are made of copper. The heat transfer performance of micromembrane suspended on microchannel is demonstrated against wall superheat in Figure 1.10c. In heat flux curve, four different evaporation surfaces with identical heating areas ($1 \times 1 \text{ cm}^2$) were investigated.

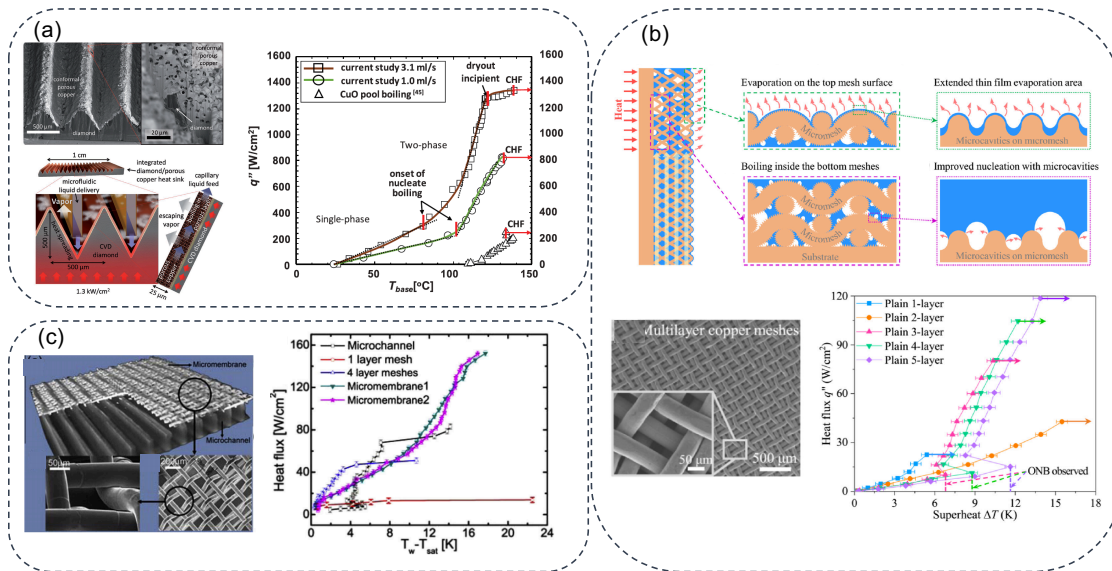


Figure 1.10 (a) conformal porous copper coated CVD grown diamond microchannels, reprinted with permission from REF. 91, WILEY. (b) multilayered copper meshes, reprinted with permission from REF. 92, ELSEVIER. (c) hybrid structure composed of bonded copper mesh on microchannels, reprinted with permission from REF. 93, ELSEVIER.

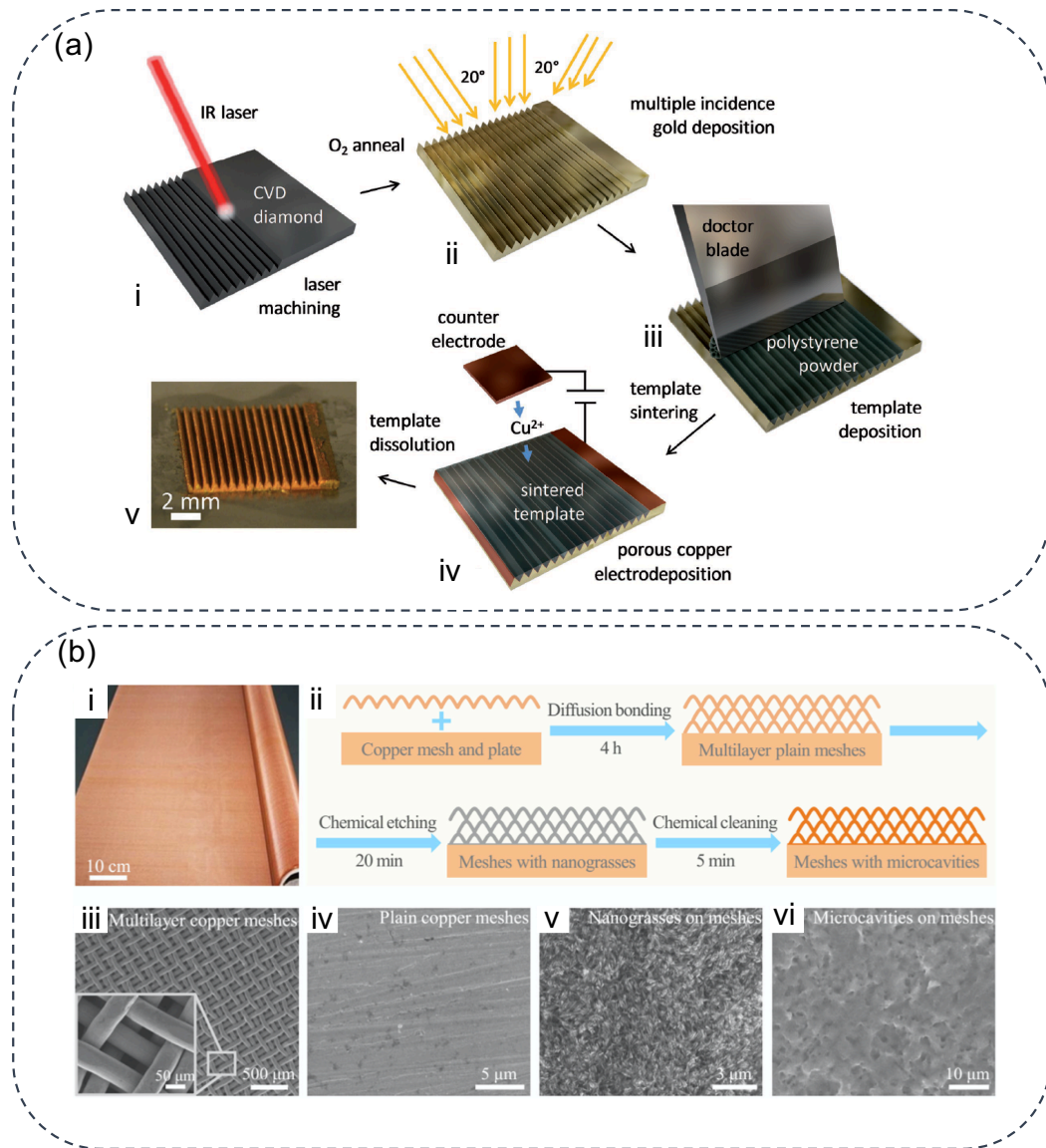


Figure 1.11 Fabrication process of (a) conformal copper coated CVD grown diamond microchannels, reprinted with permission from REF. 91, Wiley. (b) multilayered copper mesh wicks with different roughness on the surface, reprinted with permission from REF. 92, ELSEVIER.

1.7 Micro/Nano Channels

Thin film evaporation as heat and mass transfer mechanism utilizes capillary action to form a steady thin liquid film in contact with solid substrate. The minimized thermal resistance of steady evaporation originates fast liquid vaporization without

entering the boiling regime. The evaporation rate is an outcome of momentum transport, energy transport, and gas kinetics that depend on time scale, length scale, and thermodynamic properties^{30,94–98}. There are three main steps involved in capillary evaporation in nano-conduits, liquid transport to the liquid-vapor interface, liquid vaporization at the interface, and vapor removal⁹⁹. Understanding of underlying physics of each step assists to find new approaches to promote the maximum dissipated heat. Various experimental studies have been done on capillary transport and vapor removal from micro/nano structures, but a few experimental studies have worked on kinetic limit of evaporation at the interface. Li et al.¹⁰⁰ was conducted an experimental study on capillary evaporation in 2D nanochannels for the first time. They fabricated a hybrid silicon nanochannels composed of test channel and reference channel with two different heights (Figure 1.13a). The capillary pressure difference due to change in heights and contact angles, applies force on pinned meniscus of test channel and at the same time pulls the other meniscus at the reference channel. The evaporation rate was calculated by measuring the meniscus location displacement in test channel. The evaporation flux is measured through equation 1,

$$V^* = V \frac{h}{h^*} \quad (1.1)$$

with $\frac{h}{h^*}$ showing the ratio of reference channel to the test channel. From evaporation flux versus nanochannel length, it is found that as channel length reduces, the flux increases and then stays unchanged. It means the evaporation flux is no longer limited by fluid transport. Further experiments in vacuum chamber with pressure of 150 Pa revealed that vapor removal is also not the evaporation flux limit. The derived conclusion shows the

kinetics in nano conduits controls the evaporation flux. The kinetic-limited evaporation flux in different nanoscale confinements at 0% relative humidity is displayed in Figure 1.12a for temperatures from 20 to 40 °C. According to the evaporation flux curve as a function of height, a decreasing trend can be observed by increasing the channel's height. A change in the height results in changing of evaporation surface area. The experimental results were compared with theoretical data extracted from Hertz-Knudsen theory. The experimental results with one order of magnitude larger values presenting an extremely high evaporation flux. Presented results in Figure 1.12a explains that capillary evaporation in a nano-confinement such as nanochannel is ultimately controlled with kinetic limits at liquid-vapor interface. To analyze the kinetic limit of evaporation in nanoporous membranes, heat flux of a single nanopore and its underlying mechanism was discussed in a hybrid nanochannel-nanopore structure¹⁰¹. A single nanopore in a suspended silicon nitride membrane is connected to a nanochannel through a connecting chamber. The only variables in the hybrid geometry is the channel height and the pore diameter. The pore is hydrophilic and tested with both hydrophilic and hydrophobic outer surface area. The experiment was conducted in a vacuum chamber and pinned meniscus in nanopore/nanochannel were captured by a high-speed camera. The difference between pore diameter and nanochannel height creates the capillary pressure along the hybrid structure. The kinetically limited evaporation from nanopores were compared with evaporation flux in 2D nanochannels by Li et al¹⁰⁰. As results show in Figure 1.12b, evaporation flux strongly depends on the diameter. The maximum evaporation flux was attained for a pore with diameter of 27nm which is larger than the theoretical predictions. The possible underlying mechanisms to explain this strong dependency are change in

evaporation area and evaporation coefficient^{102–104}. To understand the effect of hydrophilicity and hydrophobicity of the top outer surface, the evaporation flux was measured for both cases and presented in Figure 1.12b. Both evaporation flux graphs in Figure 1.12b were prepared for eight set of different $\frac{d}{h}$. The fabrication method of the hybrid structure is depicted in Figure 1.13b. Nazari et al.⁹⁹ utilized the concept of negative absolute liquid pressure in uniformly heated nanochannels. A strong liquid transport was caused by the negative pressure. The evaporation continued in nanochannels without any bubble formation at the temperatures higher than boiling temperature. Smaller size of the nano-conduits than the nucleation radius prevented the bubble formation. The heat flux results are illustrated in Figure 1.12c. The fabrication process is shown in Figure 1.13c.

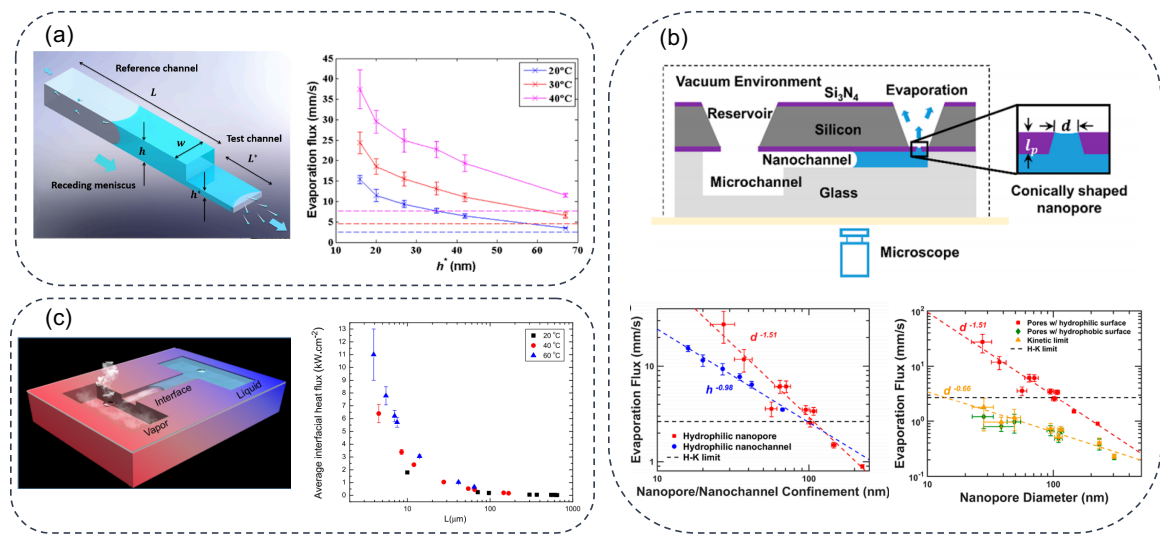


Figure 1.12 (a) A hybrid nanochannel, reprinted with permission from REF. 100, American Chemical Society. (b) A nanochannel-nanopore hybrid structure, reprinted with permission from REF. 101, American Chemical Society. (c) A nanochannel with a capillary pumping between hot and cold reservoir, reprinted with permission from REF. 99, American Chemical Society.

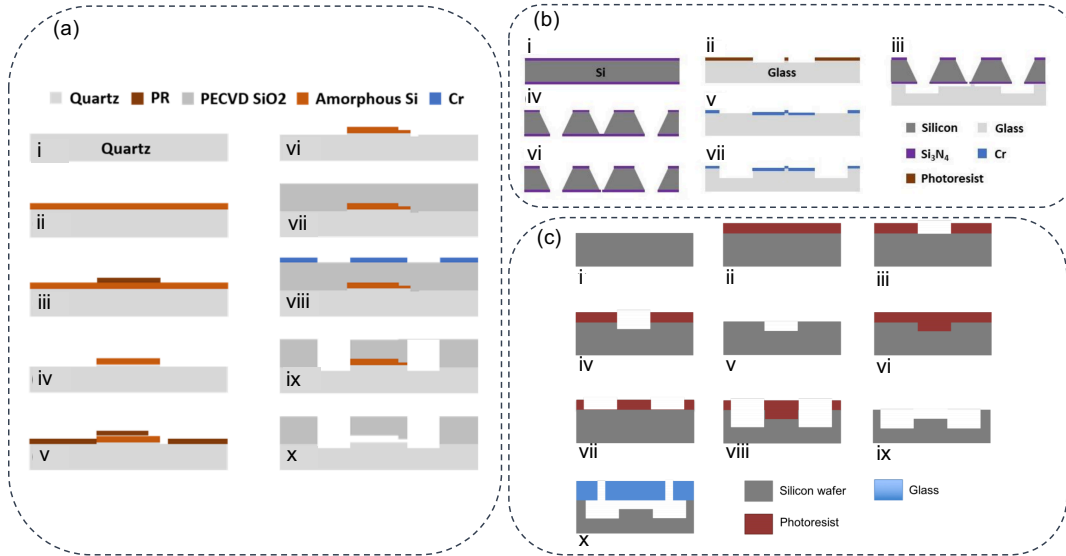


Figure 1.13 Microfabrication method of (a) hybrid nanochannels with different height for test and reference chamber, (b) hybrid nanochannel-nanopore structure, (c) nanochannels with two reservoirs.

Chapter 2: Role of Nanoconfinement on Thin Film Evaporation

This chapter presents the thermal performance of thin porous anodized aluminum oxide (AAO) membranes. The tested AAO membrane in this study has a thickness of 60 μm and averaged pore diameter of 80 nm. The underlying mechanisms of evaporation and thin film boiling in AAO membranes are investigated experimentally. The privilege of the planar porous structure for phase change heat transfer is highlighted in this work and a high dissipated heat flux of 560 W/cm^2 is achieved. The high value of transferred heat in this structure triggered by formation of a thin liquid film on top of the membrane surface. With a narrow thickness of liquid, the bubble departure frequency increases which leads to a higher heat transfer coefficient and higher critical heat flux (CHF). The reduced thermal resistance in the liquid layer also enhanced the CHF in the regime of thin film boiling. Moreover, a comprehensive characterization study on AAO membranes is performed and the special custom-made experimental setup is described in details in this chapter.

2.1 Background

High efficiency heat transfer approaches have attained considerable attention during the last decades due to their significant role in different domestic and industrial applications such as power generation^{14,15,105,106}, water harvesting⁹, water desalination^{12,13}, and thermal management in electronics^{7,8,28,46,47}. Liquid-vapor phase change process as one of the most effective heat transfer mechanism has been explored immensely to reach its optimal performance. In electronics cooling applications, reliability and lifetime of devices strongly depend on the heat transfer efficiency¹⁰⁷. An extensive investigation has been dedicated to recognize all the effective parameters on the

phase-change process^{27,29}. Surface energy and wettability^{33,108,109}, hydrodynamic and thermal resistances^{28,34}, liquid properties¹¹⁰, and capillary wicking^{36,37,39,111} can be named as most effective factors involved in liquid-vapor cooling.

Boiling with the high latent heat of vaporization has been utilized in various forms such as pool boiling^{112–114} and flow boiling^{52,115,116} for thermal management purposes. In pool boiling, the upper limit of the heat removal, i.e., the critical heat flux (CHF), is controlled by dynamics of bubble nucleation, growth, and departure^{117,118}. The CHF happens as a result of a notable decrease in the heat transfer coefficient (HTC) when a film of vapor forms near the solid surface. Enhancing the CHF through the improving of bubble nucleation site, surface area extension, wettability, and wickability is of great interest to researchers^{119,120}. Many micro/nano structures were fabricated to facilitate the solid-liquid interaction to promote the dynamics of the pool boiling. However, the maximum reported heat fluxes^{121,122} are less than 300 W/cm². The enhanced CHF can be seen in flow boiling as a result of external fluid pumping which elevates the liquid feeding to nucleation sites and improves the bubble departure speed^{91,123,124}. The flow boiling in microchannels has explored vastly as a promising phase-change process because of its capability of removing large amount of heat from small areas. The high heat fluxes of flow boiling in microchannels mostly contributed to the microlayer thin film at the walls of the channels¹²⁵. The dynamics of the nucleation and growth is dictated by the microlayer. Therefore, better understanding of thin film evaporation offers valuable insights to find how to increase flow boiling limits in confined structures. When a boiling regime forms in a confined microstructure, the vapor bubbles start to grow and fill the entire channel cross-section. By continuous growth of vapor core, the rewetting

flow is not able to reach the downstream of the channel and this mechanism triggers the CHF due to overheating¹¹⁶. Hence, it can be concluded that a separate liquid and vapor pathway will progress the boiling dynamics and result in a higher CHF with lower wall superheat⁸⁶.

Moving from pool boiling to thin film evaporation occurs with the corresponding decrease in the liquid film thickness. A new balance between thermal and hydraulic resistances is expected due to the film thickness reduction. Lower thermal resistance and shorter path for vapor to escape lead to higher HTC and consequently higher CHF. To further investigate the thin film evaporation, various micro/nano structures were studied. In a design by Lu et al.¹²⁶ thin film evaporation on a suspended ultrathin membrane is explored. The top side of the Si_3N_4 is deposited by gold to perform as the RTD heater. The hydrocarbonated Au heater and specific flow rate prevent the flooding of water on the membrane. The water was confined within the pores and contributed to a pure evaporation with high interfacial heat fluxes of $\approx 500 \text{ W/cm}^2$. Two main mechanisms are responsible for such a high heat flux in pure evaporation regime. Firstly, the ultra-thin thickness of 200 nm reduces the transport resistance forces dramatically running to extremely fast water delivery to the liquid-vapor interface. Secondly, the conduction resistance in liquid is controlled by the water radius (65 nm) confined in nanopores. A parametric study by Wilke et al.⁸³ shows the transition from flooding state to a thin film evaporation on an AAO membrane. The focus of this study is on different parameters including pore size, porosity, and meniscus location involved in pure evaporation regime. The comparison between various pore sizes reveals its influence on boiling regime before entering the pore-level pure evaporation. For larger pore sizes, the transition to pore-level

evaporation appears at higher heat fluxes and superheat. To further examine the pore size effect, Li et al.¹⁰¹ experimentally studied the evaporation kinetics at the liquid-vapor interface of a nanopore for both hydrophilic and hydrophobic single pore. The highest heat flux in pure evaporation regime with no nucleate boiling is reported by Hanks et al.⁸⁵ for a ultra-thin silicon membrane which is supported on microchannels. The high permeability and increased capillary pressure in this configuration is enlightened by using low surface tension fluids such as pentane and R245fa. The contamination accumulation in the liquid is known as the limiting factor for reaching higher heat fluxes not the capillary pressure in nanopores.

2.2 Motivation and Scope of the Present Work

In this work, we investigate the heat transfer performance of planar AAO membranes with averaged pore diameter of 80 nm and thickness of 60 μm . The test is performed in an experimental setup designed with specific features to reveal the potential of thin porous membranes for dissipating high heat fluxes in high power electronics. The coolant is DI water and supplied with a constant rate to the membrane by a syringe pump. Heat is generated in the Platinum heater on the top side of the membrane. A high heat flux of 560 W/cm^2 is achieved in the thin film boiling regime. A critical analysis explains the physics involved in this phenomenon and the contribution of effective parameters in enhanced CHF and HTC. A structural characterization of AAO membrane has been also presented.

2.3 Experimental Procedure

The nanoporous AAO membrane was characterized by SEM and AFM as shown in Figure 2.1 and Figure 2.2. Figure 2.1 demonstrates the top view, tilted view, and cross-

sectional SEM images of the membrane with averaged pore diameter of 80 nm and thickness of 60 μm . A better understanding of AAO membrane structure and its roughness can be found in Figure 2.2 which displays the AFM image of the surface. The average porosity of AAO membrane is calculated with Image J analysis of SEM images of three different membranes which is $34.90 \pm 2.65\%$. The pore size shape and distribution is shown in Figure 2.3.

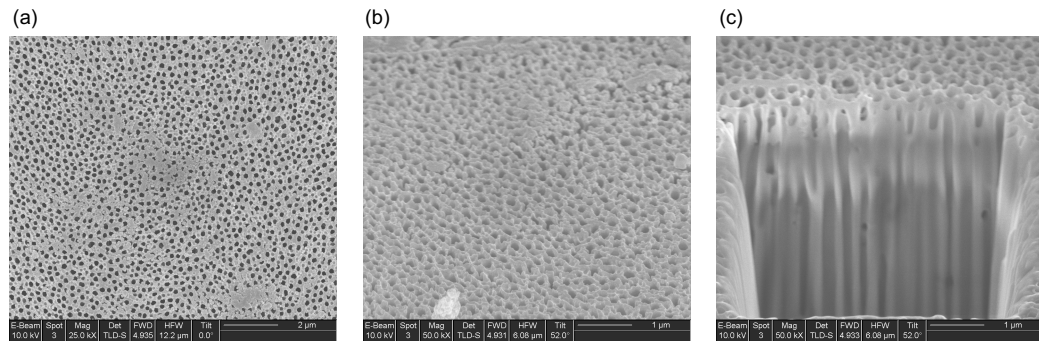


Figure 2.1 SEM images of (a) top view, (b) tilted view, and (c) cross-sectional view.

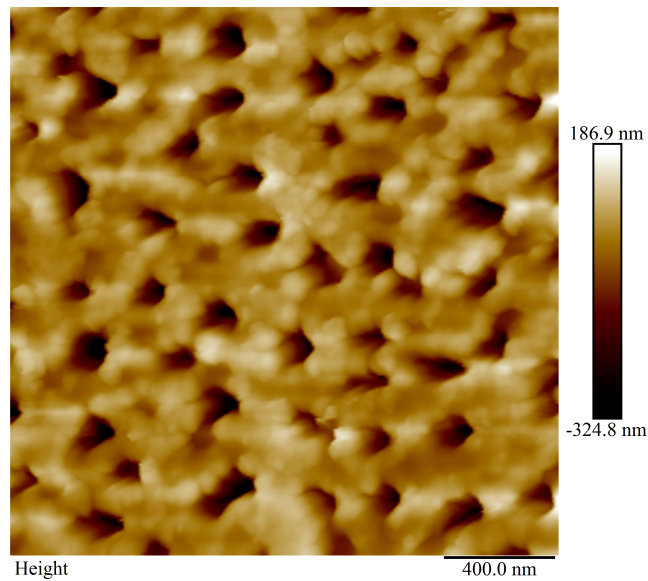


Figure 2.2 AFM image of AAO membrane with pore diameter of 20 nm.

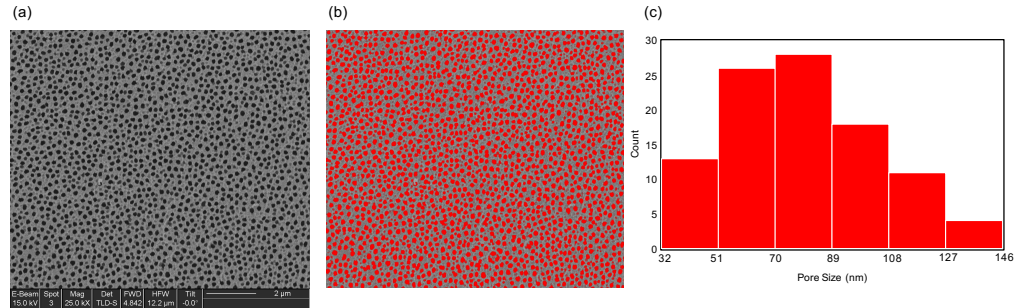


Figure 2.3 (a) SEM of AAO membrane (b) Pore distribution on AAO membrane characterized by Image J, and (c) Pore distribution graph.

A thin film (50nm) of Platinum (Pt) was sputtered on the AAO membrane with an area of 8 mm × 6 mm to serve as both heater and RTD. In the next step, two thick (1μm) Copper (Cu) pads were deposited by an e-beam evaporator as electrodes on two sides of the membrane. A thin layer of Ti and Cr were used as adhesion layers for Pt and Cu, respectively. All RTD heaters were calibrated prior to each experiment in a convective oven (Figure 2.4). The resistance was measured using a Keithly 2100 Digit Multimeter from 25 °C to 60 °C at a step of 5°C. A K-type thermocouple was placed in a very close distance (around 1mm) on top of the heater to measure the air temperature in a very close distance to the membrane. Each temperature step has been held for 1 hour before resistance measurement to reach the steady-state. A linear relation between resistance and temperature was attained as demonstrated in Figure 2.5. The average Temperature Coefficient of Resistivity (TCR) is 0.0022/°C, which is less than the bulk metal (0.0039/°C).

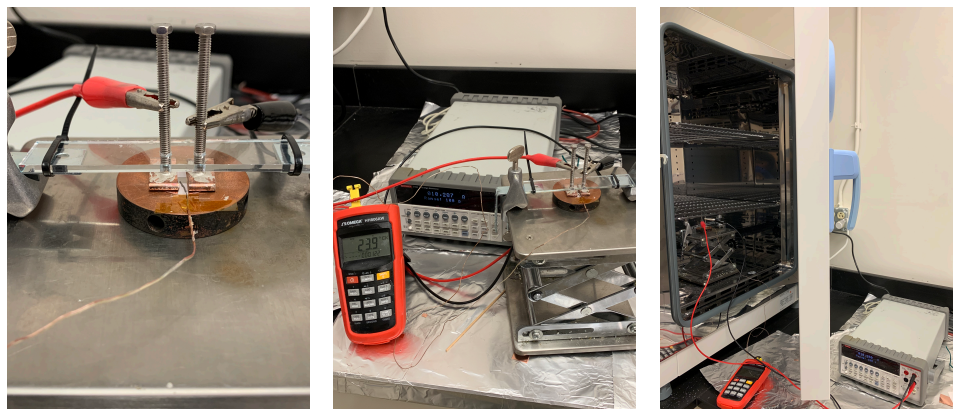


Figure 2.4 Two ports of Multimeter are connected to the copper electrodes to measure the Pt heater resistance with a K-type thermocouple attached to 1 mm above of the membrane for reading temperatures. The whole setup is placed in a convective oven.

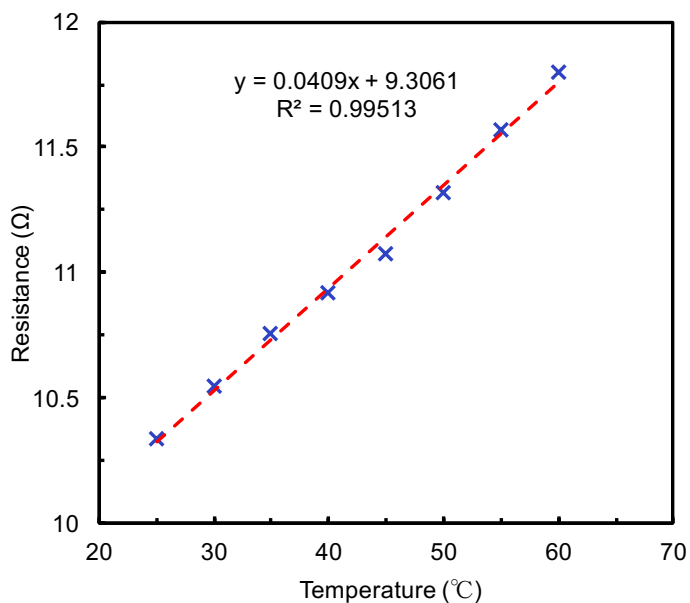


Figure 2.5 Platinum resistance changes vs. temperature.

Then, the AAO membrane was attached on a custom made PTFE holder and sealed with epoxy glue. The PTFE is a good thermal insulator and avoids heat losses through the supporting stage. After epoxy was completely cured, the holder with attached membrane on top was placed inside a vacuum chamber (Figure 2.6). The vacuum chamber is a stainless-steel evaporation chamber with four view ports and is connected to

a pressure transducer (INFICON, CDG045D) with an accuracy of 0.15% of the read value. All the non-condensable gases were evacuated, and pressure of the chamber was reduced to less than 2 kPa. Moreover, a fluid degassing platform was utilized to remove the dissolved gasses from the water before entering to the liquid chamber. The water kept in a glass flask and stirred and heated on a hot plate with temperature of 40 °C. At the same time, a roughing pump (Kurt J Lesker, KJLC-RV224) evacuated the dissolved gasses and continued to perform for at least 1 hour before each test. The degassed water was later transferred to the liquid vacuum chamber to get pressurized with nitrogen gas and reach a preset pressure before entering the vapor chamber and wetting the membrane. The water pressure was set at 1 bar. A connected pressure gauge to the liquid chamber indicates the water pressure. By opening the connection valve between the water chamber and syringe, the pressurized water filled the syringe and later got delivered to the sample through the applying force by syringe pump. A schematic of the experimental setup is demonstrated in Figure 2.7. To avoid the mechanical failure in the membrane due to high pressure difference of water and vapor chamber, the nitrogen gas is injected into the vapor chamber to provide the same pressure as water. After pressure stabilization in both water and vapor chamber, water was supplied to the test membrane by employing the constant flow rate by syringe pump. The flow rate kept uniform through the whole test time. The heating power was applied to the Pt heater by a DC power supply (Keysight N8761A). Two Cu foils were also used between Cu electrode pads on the membrane and screws which are connected to power supply ports. A four-probe method was utilized to measure the applied heat and temperature change of the heater. In the RTD method, voltage was increased gradually until the CHF is reached. A LabVIEW program

measured the corresponding current to each voltage to obtain the resistance and consequently the temperature of the calibrated heater. A minimum time step of 30 seconds is considered between each incensement in the voltage to reach stabilization. Afterwards, the CHF and superheat is calculated and presented for different cases. A camera was positioned on the top view port to capture the transition from the flooded stage (pool boiling) to the thin film boiling. Figure 2.8 depicts images of different sections of experimental setup.

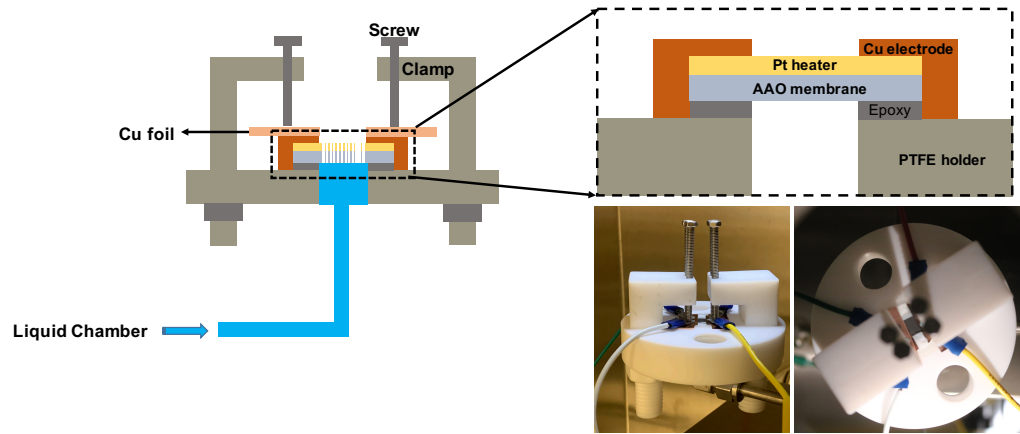


Figure 2.6 Attachment of AAO membrane on PTFE holder.

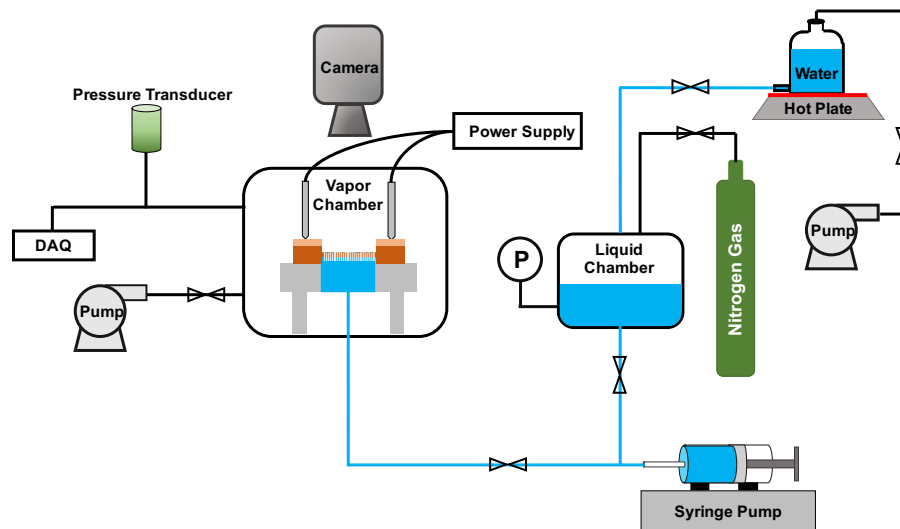


Figure 2.7 Schematic of experimental setup.

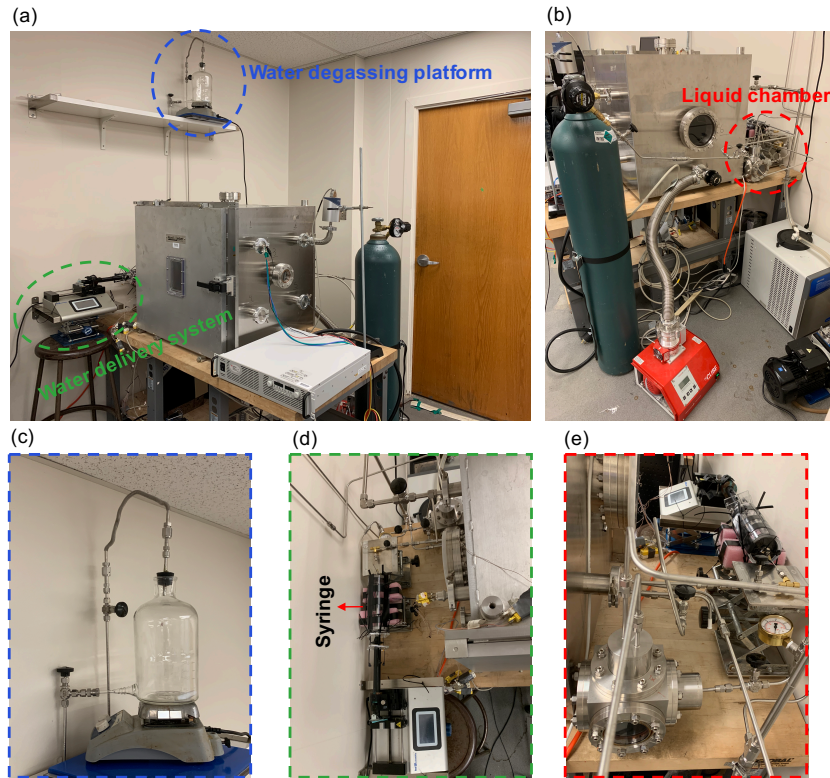


Figure 2.8 Experimental setup including stainless-steel vapor chamber, liquid chamber, water degassing platform, and water delivery system consisting of syringe and syringe pump.

In this experiment, heat is dissipated through convection in the fluid, latent heat, and conduction in the experimental sample holder. The measured heat loss in the experimental fixture presented in the Figure 2.9. To measure the heat loss, heat flux is applied on a sample in the vapor chamber with completely similar conditions as it has in the main test. The only difference is no water supply to the membrane. The maximum heat loss is 0.24 W or 0.48 W/cm^2 which is much less than the acquired heat flux (560 W/cm^2) by latent heat and convection in water.

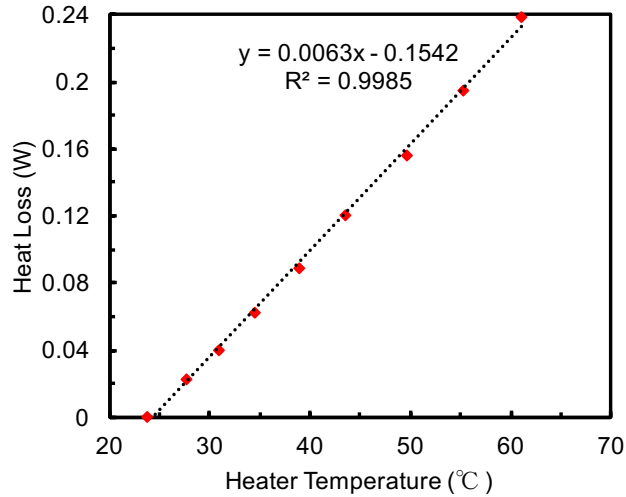


Figure 2.9 Conduction heat loss as a function of heater surface temperature.

2.4 Results and Discussion

In this study, we measured the dissipated heat from the porous membranes by applying heat through power supply and feeding the sample with DI water as the coolant. A constant flow rate is applied to pass water through the nanopores and wet the membrane to the point of forming a thick layer (few millimeters) of water on top surface. Figure 2.10a demonstrates the water formation on the membrane which involves single phase convection. This flow rate is large enough to overcome the viscous forces which is defined by membrane thickness, but yet smaller than a value to be accounted as flow boiling. So, convective boiling does not play a role inside the nanopores through the water transfer. The small size of nanopores (80 nm) only contributes to high capillary pressure and is decoupled from the viscous resistance⁸². As applied heat flux elevates, by increasing wall superheat, bubble nucleation starts to form as it is exhibited in Figure 2.10b, and heat transfer enters the pool boiling regime. The size of bubbles enlarges with

amplified applied power which results in dissipating more heat. Transferring more heat at liquid-vapor interface narrows the thickness of water layer for a constant mass flow rate (Figure 2.10c-d). Further decrease in liquid thickness reduces the barrier for bubble departure and changes the boiling regime from pool boiling to thin film boiling. The thin film boiling is displayed in Figure 2.10e with water thickness of tens of microns which is two orders of magnitude smaller than the pool boiling. The calculation of the liquid thickness in film boiling is presented in the next section. The increase in heat flux continued until the dryout is arrived at CHF. As shown in Figure 2.10f, at dryout stage, water flow is not enough to cover the surface and will cause a huge rise in wall superheat which eventually leads to membrane failure. The membrane is covered with liquid the whole time of experiment except for the last dryout stage. At the emergence of CHF, small vapor bubbles start to coalesce and create local hot spots at different locations. Figure 2.11 displays the dryout region on a tested AAO membrane.

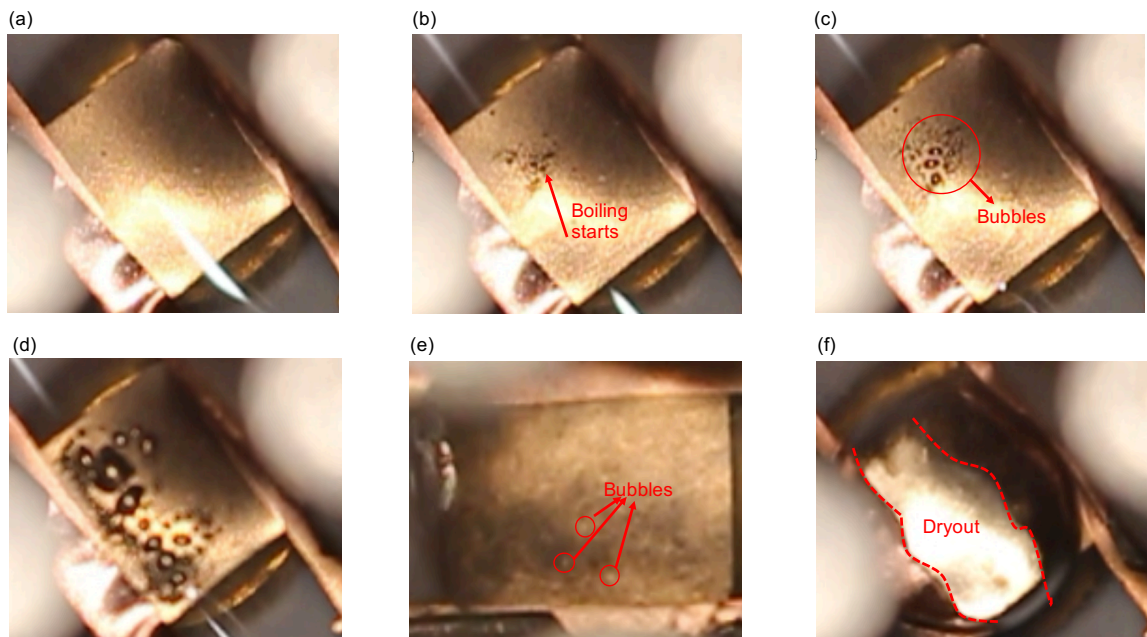


Figure 2.10 Transition in heat transfer mechanism on AAO membrane starting from (a) single phase convection to (b-d) pool boiling, (c) thin film boiling, and finally (d) dryout.

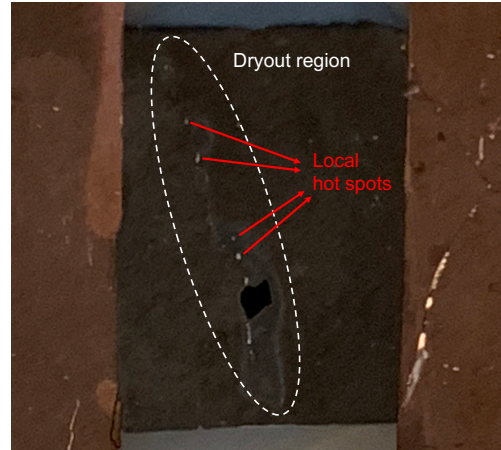


Figure 2.11 Dryout area and hot spots locations appeared on the membrane surface after reaching CHF.

Figure 2.12a illustrates the dissipated heat flux versus wall superheat for three different mass fluxes including 5 ml/min, 15 ml/min, and 17 ml/min. The reported heat flux in Figure 2.12a is the applied heat by power supply divided by the heater area. As it shown, a similar behavior for all three mass fluxes is observed. The heat transfer mechanism starts with simple convection followed by bubble nucleation, and then pool boiling begins. By advancing the pool boiling, more water is evaporated, and the liquid thickness lessens leading to thin film boiling initiation. The negative slope corresponds to the later stage of thin film boiling regime denoting the reduced wall superheat at higher heat fluxes as a consequence of improved heat transfer coefficient (HTC). In thin film boiling, as heat surges, the disjoining pressure increases by reduction in liquid layer thickness helping liquid molecules to escape from the microlayer at evaporating meniscus¹²⁷. Here, to understand how liquid layer thickness varies, the thermal boundary layer thickness of nucleate boiling at the beginning of thin film boiling and CHF are calculated based on an equation provided by Tien¹²⁸ which is as follows,

$$\bar{h}\delta_{th} = 3.22 k \quad (2.1)$$

where \bar{h} is the averaged heat transfer coefficient, δ_{th} is thermal boundary layer thickness, and k is liquid thermal conductivity. The δ_{th} is around 170 μm at the pool to thin film boiling transition occurring at heat flux of around 50 W/cm^2 and wall superheat of 40 $^\circ\text{C}$. The thermal boundary thickness recedes to 18 μm to 52 μm at the CHF for the highest to lowest flow rate, respectively. The reduced liquid thickness significantly affects the thermal resistance in liquid layer. As a result of lower thermal resistance, at high heat fluxes, the water temperature reaches close to the wall temperature. An order of magnitude change in thermal boundary thickness influences the bubble diameter size. To confirm this, maximum diameter of bubbles in the superheated liquid film is estimated according to Zuber¹²⁹ as follows,

$$D_m = \frac{\Delta T c_p \rho_l k \Delta T}{L \rho_v q} \quad (2.2)$$

where D_m , ΔT , c_p , ρ_l , ρ_v , k , L , and q represents the maximum diameter, wall superheat, specific heat, liquid density, vapor density, liquid thermal conductivity, latent heat of vaporization, and heat flux, respectively. The maximum bubble diameter close to CHF is $\sim 15.8 \mu\text{m}$ for flow rate of 17 ml/min corresponding to maximum CHF. The bubble size variation from few millimeters at the beginning to 15.8 μm at thin film boiling boosts the dynamics of growth and departure considerably. The enhanced boiling process can also be understood from the continuous increase in HTC as elucidated in Figure 2.12b. The enhancement of pool boiling relation with bubble size and departure frequency is also investigated with Shin et al.¹¹⁷. As depicted in Figure 2.12a, increase of mass flow rate results in delayed transition to thin film boiling and achieving higher CHF due to more available liquid.

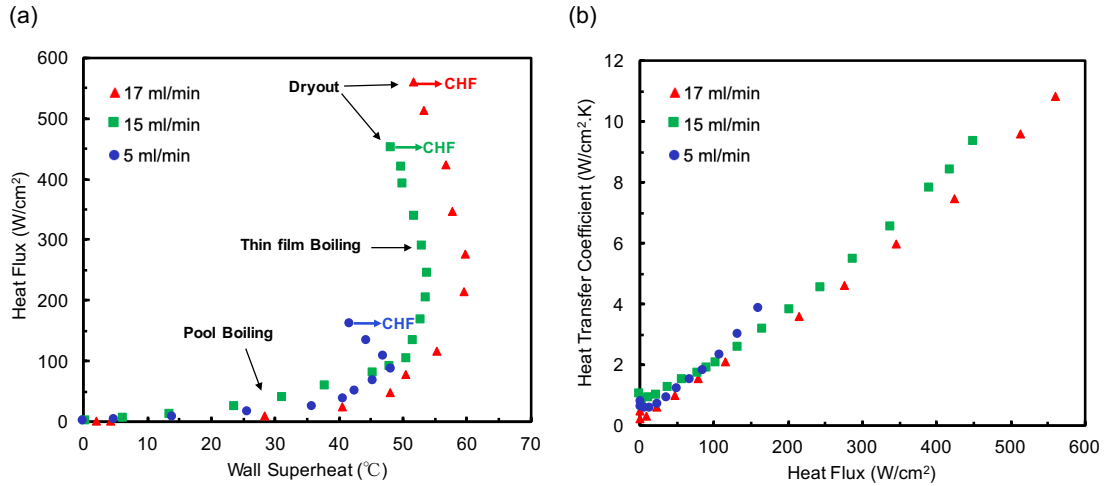


Figure 2.12 (a) Heat flux vs. wall superheat, and (b) Heat transfer coefficient as a function of heat flux.

In addition to aforementioned mechanisms for enhanced heat fluxes in this study, the fast replenishment of water to nucleation sites notably improves the boiling process leading to higher CHF. The reason for this matter is the separate liquid-vapor pathways for nanoporous AAO membrane. The generated vapor at the top of the membrane diffuses to the vapor chamber while the water is supplied from the bottom side of the membrane. Moreover, the short pitches of less than 100 nm between the pores, facilitates the liquid feeding in lateral direction on the membrane as well.

Figure 2.13 displays the wall superheat variation as a function of time which is originated from the increase in heat flux. The results for mass flow rate of 17 ml/min is shown in Figure 2.13a-b. The gradually increased wall superheat continued to the point where thin film boiling enters an inertia-controlled bubble growth regime. As heat flux enhances at this stage, wall superheat continues to drop due to higher heat transfer coefficient as a consequence of lower thermal resistance and shorter path for vapor to escape. The temperature is almost stable and uniform at each specific heat flux. As Figure 2.13 claims, higher mass flux increases the CHF by feeding more liquid to the membrane

active sites. A Reduction in the thickness promotes this feeding process by diminishing the resistance losses in the water pathway. Moreover, the role of surface tension on dynamics of boiling process can be investigated by applying surfactants on top side of membrane in future studies.

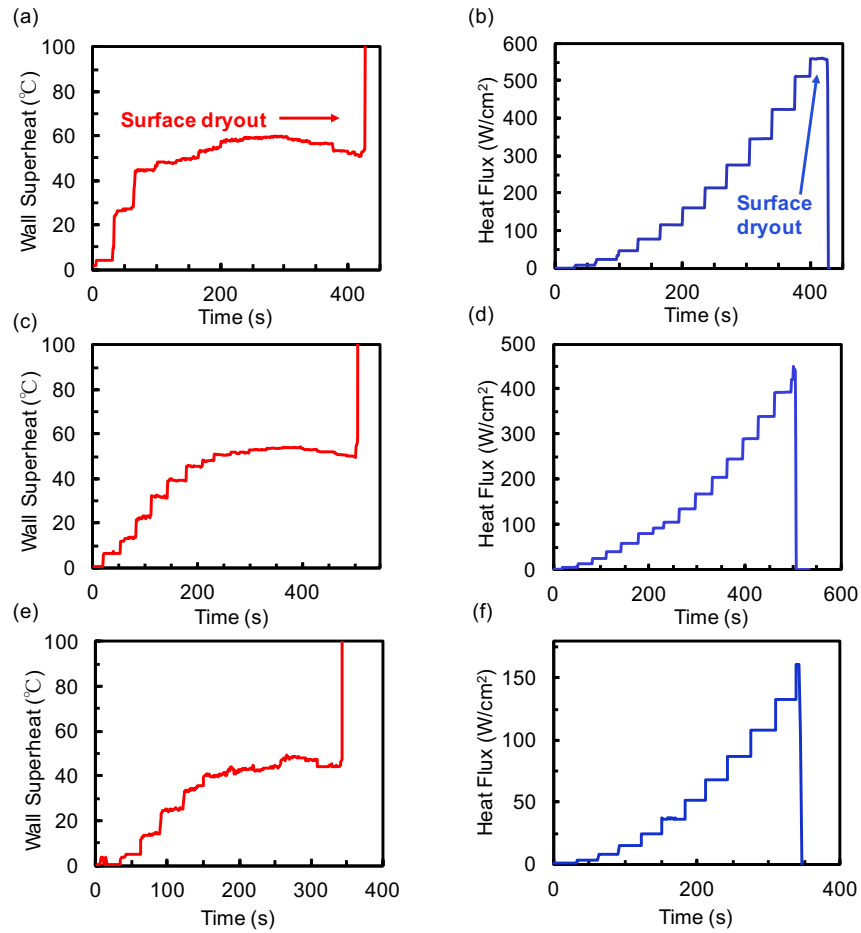


Figure 2.13 Wall superheat and heat flux incensement for mass flux of (a-b) 17 ml/min, (c-d) 15 ml/min, and (e-f) 5 ml/min.

2.5 Summary

In conclusion, we investigated the thermal performance of nanoporous planar membranes with water as the cooling liquid. The high heat flux of 560.4 W/cm^2 is

attained and the responsible reasons for it are discussed. A separate pathway for liquid and vapor provides faster water replenishment to nucleation sites. In addition, boiling regime in a thin liquid layer film improves the rate of bubble departure because of reduced thermal conduction resistance and shorter route for dissipating heat. These mechanisms are accountable for increase in boiling slope to eventually a negative slope. This study illuminates the importance of planar nanoporous membranes for removing heat from high power devices.

Chapter 3: Stress-Localized Durable Anti-Biofouling Surfaces

Growing demands for bio-friendly antifouling surfaces have stimulated the development of new and ever-improving material paradigms. Despite notable progress in bio-friendly coatings, the biofouling problem remains a critical challenge. In addition to biofouling characteristics, mechanically stressed surfaces such as ship hulls, piping systems, and heat exchangers require long-term durability in marine environments. Here, we introduce a new generation of anti-biofouling coatings with superior characteristics and high mechanical, chemical and environmental durability. In these surfaces, we have implemented the new physics of stress localization to minimize the adhesion of bio-species on the coatings. This polymeric material contains dispersed organogels in a high shear modulus matrix. Interfacial cavitation induced at the interface of bio-species and organogel particles leads to stress localization and detachment of bio-species from these surfaces with minimal shear stress. In a comprehensive study, the performance of these surfaces is assessed for both soft and hard biofouling including *Ulva*, bacteria, diatoms, barnacles and mussels, and is compared with that of state-of-the-art surfaces. These surfaces show *Ulva* accumulation of less than 1%, minimal bacterial biofilm growth, diatom attachment of 2%, barnacle adhesion of 0.02 MPa and mussel adhesion of 7.5 N. These surfaces promise a new physics-based route to address the biofouling problem and avoid adverse effects of biofouling on the environment and relevant technologies.

Some parts of the following chapter first prepared in *Soft Matter* 2019, 15, 6014-6026 [99]

Title: Stress-Localized Durable Anti-Biofouling Surfaces

Authors: Bahareh Eslami, Peyman Irajizad, Parham Jafari, Masoumeh Nazari, Ali Masoudi, Varun Kashyap, Shane Stafslie, and Hadi Ghasemi.

3.1 Background

Biofouling is an outcome of undesired marine organisms' accumulating on surfaces. It impacts a variety of industries such as naval, heat exchangers, piping systems, and medical fields¹³⁰⁻¹³³ adversely. Any engineered structure immersed in water is prone to irreversible settlement of fouling organisms on it which leads to both economic and environmental penalties^{1,134}. Marine fouling on ship hulls increases the hydrodynamic drag resistant forces leading to lesser maneuverability of vessels and higher fuel consumption. This inevitably gives rise to emission of harmful compounds¹³⁴⁻¹³⁶. Moreover, it accelerates surface corrosion, damage to protective coatings and required cleaning maintenance at a cost of billions of dollars a year to the maritime industry^{131,137}. The estimated cost due to fouling for the US Navy fleets, which represents only 1% of world fleets in numbers, is approximately \$200M per year^{130,135}. Hence, development of new materials to solve biofouling problem is of immediate importance.

Fouling process initiates with the formation of conditioning film induced by accumulation of physically adsorbed organic molecules (proteins, polysaccharides, glycoproteins) as a precursor to microfouling settlements, including bacteria, fungi, and protozoans¹³⁸⁻¹⁴¹. This colonization is governed by Brownian motion, electrostatic interactions and Van der Waal's forces^{142,143}. The growth development proceeds with macro-fouler establishments such as barnacles, mussels, hydroids, and tubeworms^{144,145}. The diversity of fouling organisms including their diverse adhesion mechanisms leads to

complexity in design of anti-biofouling coatings¹³⁰. Fundamental understanding and manipulation of the adhesion mechanism and stability of the responsible forces of the adhesive complex to the substrate are paramount to develop highly efficient and reliable antifouling surfaces^{146, 147}. The progress of antifouling surfaces is attributed to modification of effective parameters such as topography^{148, 149}, roughness¹⁵⁰, surface energy^{151, 152}, and elasticity modulus¹⁵³. Historically, toxic antifouling agents containing biocides such as lead, arsenic, mercury and their organic derivatives were used on ship hulls. Tributyltin (TBT), a revolutionary self-polishing copolymer was the most successful in combating bio-fouling in ships and was estimated to cover 70% of the world's fleet¹⁵⁴. However, its use was banned globally in 2008 by the International Maritime Organization (IMO) due to severe shellfish deformities and the bioaccumulation of tin in some ducks, seals and fish¹⁵⁵⁻¹⁵⁸. Numerous investigations have been conducted to substitute the biocidal toxic surfaces with biocompatible fouling resistant coatings^{155, 159} including silicone elastomer based materials¹³⁸, fouling release paints^{130, 160-163}, organogels^{164, 165}, fluoropolymers¹⁶², Poly (ethylene glycol)^{166, 167}, slippery liquid-infused porous surfaces (SLIPS)¹⁶⁸⁻¹⁷², Zwitterionic¹⁷³⁻¹⁷⁶, Polydimethylsiloxane-based materials^{177, 178}, and bio-inspired micro/nano topographical surfaces¹⁷⁹⁻¹⁸¹. The zwitterionic polymers have received increasing attention over the recent years for their promising ultralow fouling and antibacterial properties. Surface hydration layer is the main antibacterial mechanism responsible for repelling the bacteria and fouling species. Strong hydrogen-bond of water molecules at the polymer surface and electrostatic interactions improve their performance. However, lack of long-term durability and mechanical stability have limited the effectiveness of these anti-

biofouling coatings. Various durability tests should be conducted to qualify antifouling surfaces for marine environment. It is also noteworthy that applicability of coating techniques in large scales is an essential parameter in the naval industry.

3.2 Motivation and Scope of the Present Work

Here, we present a new generation of durable anti-biofouling materials called stress-localized surfaces. These surfaces are based on a new physics, stress-localization¹⁸², developed to minimize adhesion of solids on a surface. This physics is implemented in stress-localized surfaces and their superior anti-biofouling performance is demonstrated. In a comprehensive assessment, adhesion of five different marine organisms is analyzed on these coatings. The performance of these stress-localized coatings was investigated in comparison with state-of-the-art silicone elastomer-based fouling-release coatings including Polydimethylsiloxane (PDMS), Silastic 2, polysiloxane and Intersleek 700. We demonstrated superior mechanical, chemical and environmental durability of these surfaces. Furthermore, on-site reparability of the coatings is demonstrated by spraying the coatings on the damaged area.

3.3 Sample Preparation

The physics of stress-localization and mathematical derivations is discussed in our recent publication¹⁸². These surfaces are composed of two phases: phase (I) with high shear modulus and phase (II) with low shear modulus, Figure 3.1. Phase I is an elastomer with high shear modulus and phase II is organogel particles consisting of tuned liquid organic phases entrapped within a solid phase (three-dimensionally crosslinked gel network). The shear stress for detachment of a solid from elastomers (σ) is proportional

to shear modulus of elastomers ($\sigma \propto \sqrt{G}$)¹⁸³. That is why gels with low shear modulus have minimal adhesion to solid objects. In the stress-localization concept, visualized in Figure 3.2, once a solid (which here is a bio-foul) attaches to the coating, at the solid-coating surface, we have two interfaces, solid-phase I and solid-phase II. If the solid is exposed to a shear rate, solid locally detaches from phase II as phase II has low shear modulus. The detachment of solid from phase II forms some cavities at the solid-coating surface as shown in Figure 3.2b. Note that imposed shear stress forms cavities at the coordinate of phase II. The cavities at the interface localize stress at the periphery of the cavities. This localized shear stress opens the cavity and leads to detachment of solid from the coating. The stress-localization effect at the interface can reduce the shear stress for detachment of solid from the substrate by an order of magnitude compared to a material with the same shear modulus. We could also predict the stress-localization effect through first-principles as discussed in our previous work¹⁸².

As shown in Figure 3.2a, we visualized the stress-localization effect through a developed experimental setup. A glass prism is attached to a stress-localized surface. The interface of the glass and the stress-localized surface is visualized through a high-speed imaging camera and a microscope. As shown in Figure 3.2b, by a small shear force, the cavities are formed at the coordinates of phase II. The fringes show the growth of the cavities. The growth of these cavities leads to final detachment of solid from the stress-localized surface.

Through mathematical formulation of the problem, the adhesion on stress-localized surfaces is written as¹⁸⁴

$$\sigma_s = g(\varphi_{II}) \left(\frac{a}{l}\right) \sqrt{\frac{\overline{W}_a G_m}{h}} \quad (3.1)$$

where $g(\varphi_{II})$ denotes the stress-localization function, a and l are the geometrical parameters in the adhesion measurement setup (Figure 3.2c), φ_{II} is the volumetric fraction of phase II, \overline{W}_a is the work of adhesion of the material, and G_m is the shear modulus of the material. The value of stress-localization function varies between 0 and 1. It is demonstrated that this function reduces adhesion of a solid on a surface by an order of magnitude (i.e., $g(\varphi_{II})=0.1$)¹⁸⁴. Here, we implemented the same concept in anti-biofouling surfaces. Phase I in these structures is silicon elastomer with tensile strength of 8 N/mm², Shore hardness A of 30, tear strength of 13.5 N/m. The procedure for development of the organogels are as follow: 10 mL of Sylgard 184 base was mixed with 1 mL of Sylgard 184 curing agent. 100 mL of an organic liquid (i.e., Polydimethylsiloxane) was added to this mixture. The solution was then vigorously mixed to obtain a homogeneous solution. The precursor sample was heated at 100 °C for 4 hrs in a petri dish. The final product is a non-syneresis organogel. Non-syneresis property of organogel comes from miscibility of silicone oil with PDMS before and after gelation¹⁸⁵. Once phase II was developed, it was crushed in the presence of silicon oil for 10 mins to avoid aggregation of gel particles. The solution was filtered to remove excess oil. The final product is a batch of gel particles with dimension in the range of 2-20 μm. It should note that shape and size of the organogels can significantly affect the stress-localization that needs to be studied in detail in future works. The particles were mixed with the elastomer in a pre-defined concentration. The solution was diluted with a solvent, Hexamethyldisiloxane, to reduce viscosity for spraying on a surface. Developed samples of ABF 1, ABF 2, and ABF 3 consist of 50%, 33% and 25% of phase II,

respectively.

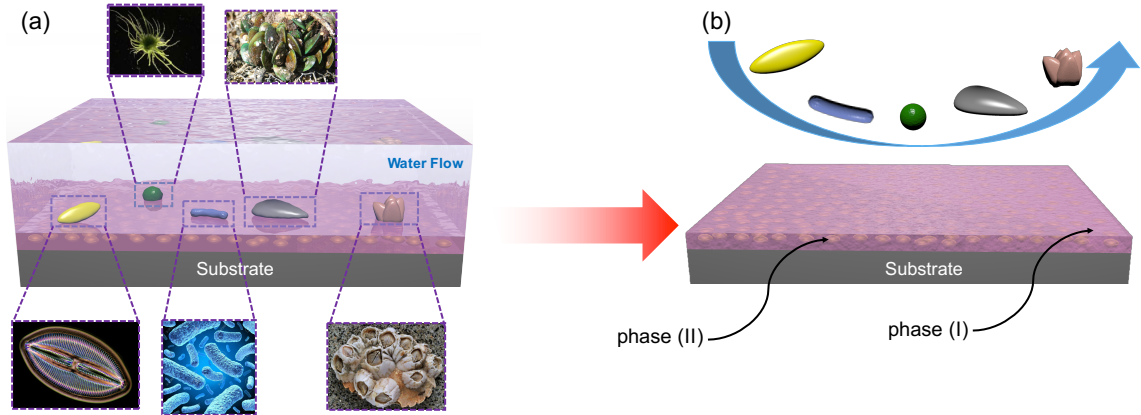


Figure 3.1 (a) and (b) Schematic of water flow including marine organisms (diatom *Navicula*, *Ulva* spores, bacterium, Mussels, and barnacles from left to right) over stress-localized coatings and its anti-biofouling property.

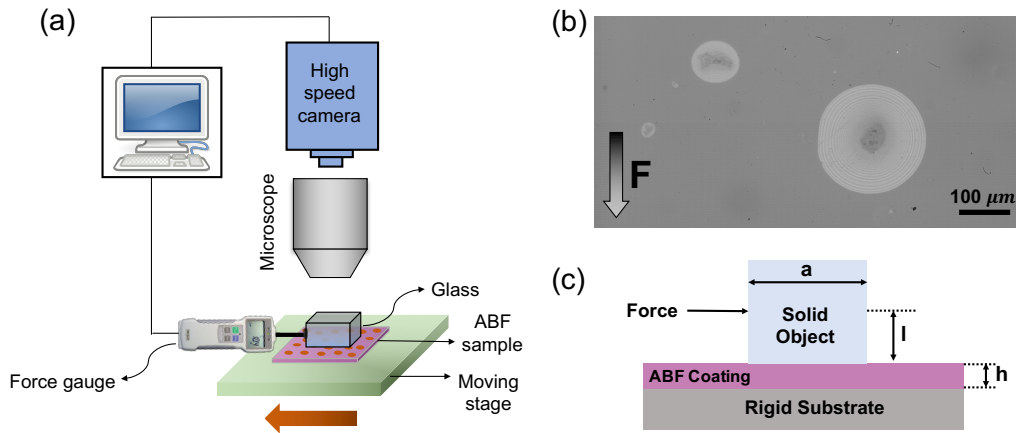


Figure 3.2 (a) Schematic of experimental setup to exhibit stress-localization mechanism. (b) Interfacial cavities formed at phase II coordinate due to their low shear modulus. (c) The geometrical parameters in surface adhesion measurements.

Scanning Probe Microscopy (SPM, Bruker Multimedia 8) was used to characterize mechanical and surface properties of the anti-biofouling coatings and the settled biological cells on the coating. SPM was set on ScanAsyst mode in air using Silicon Tip on Nitride cantilever. This mode allowed us to study adhesion behavior of the

cells giving the information of preferred attachment coordinate and cell accumulation.

3.4 Biofouling Assays

The studied fouling organisms belong to two main categories. They are ‘microfouling’ (i.e., *Ulva* spores, bacteria *Cytophaga lytica*, and diatom *Navicula*) and ‘hard macrofouling’ (i.e., barnacle and mussel). We utilized an environmental chamber (Carolina Biological Supply) to precisely control critical parameters such as light, humidity, and temperature to determine functionality of stress-localized coatings in the simulated marine environment.

3.4.1 Settlement of *Ulva* zoospores

All the samples were placed in petri dishes and filled with the sea water solution containing suspended spores. To settle *Ulva* spores on the surface, the suspended spores were diluted to an absorbance of 0.15 at 660 nm and then added to the petri dishes. The petri dishes were transferred to the dark environmental chamber as quickly as possible and incubated at 20°C for 45-60 minutes¹⁸⁶. All the samples from each treatment were then washed 10 times by passing in a beaker of seawater to remove unsettled spores. To fix the settled cells on the substrates, an additional treatment was carried out by placing the samples inside 2.5% glutaraldehyde solution for 10-15 minutes.

3.4.2 Attachment and Adhesion of Bacterium *C. lytica* and Diatom *Navicula*

Initial cell attachment and biofilm growth of algae were assessed before water jet adhesion analysis.

Bacterium *C. lytica*: A 5% suspension of bacterium in ASW + nutrients ($\sim 10^7$ cells.ml⁻¹) was prepared and 1 ml was added to each well of a 24 well-plate. A 24 well-plate was used to study characteristics of bio-species on the surface. The circular coupons were coated uniformly by ABF and other coatings with the same thickness of 100 μm and were placed in the wells. Plates were incubated at 28 °C for 24 hours to facilitate bacterial attachment and colonization. Then, plates were rinsed three times with DI water and stained with crystal violet. Images for analysis were taken after staining and extraction of crystal violet in 33% acetic acid (AA). The resulting eluates were measured for absorbance at 600 nm. After 24 hrs of bacteria settlement, water jet adhesion was conducted for 5 seconds at pressure of 10 and 20 psi.

Diatoms *Navicula*: Diatoms were diluted to an optical density (OD) of 0.03 at 660 nm in artificial sea water (ASW) supplemented with nutrients. 1 ml of the diatom solution was added to each well and allowed to incubate in static condition for 2 hours to facilitate cell attachment. For biofilm growth analysis, the wells were incubated for 48 hours. Cell attachment and biofilm growth were quantified by fluorescence measurements of dimethylsulfoxide (DMSO) extracts of chlorophyll. Cell attachment/solution growth was reported as fluorescence intensity (relative fluorescence units). After 2 hrs of cell attachment, water jet adhesion was carried out for 10 seconds at pressure of 10 and 20 psi.

3.4.3 Attachment and Adhesion of Hard Macrofouling Barnacle and Mussel

To examine attachment and adhesion of barnacles, six *A. amphitrite* barnacles were immobilized on the surface of the coatings. Coatings were analyzed after 2 weeks of

reattachment with daily feedings of brine shrimp. In order to investigate adhesion behavior of mussel *Geukensia demissa*, coatings were analyzed after 3 days of attachment with two feedings of phytoplankton. A tensile force gauge, mounted to an automated stage, was used to measure the force required to completely remove attached barnacles and mussels from the surfaces.

3.5 Statistical Analysis

The coverage percentage of species on the surfaces was measured through statistical analysis of images obtained from the fluorescence microscopy. To precisely excite and capture each species in fluorescence microscope, filters with different excitation and emission spectra were utilized.

3.6 Results and Discussion

3.6.1 Bio-Friendly Characteristics

These analyses were conducted after 14 days of water immersion preconditioning. Leachate toxicity for *C. lytica* was assessed by introducing the bacterium into overnight extracts (artificial sea water with nutrients) for each coating and evaluating growth after 24 hrs via crystal violet colorimetric assay. Growth in coating leachates was reported as an absorbance ratio (600 nm) to a growth control. A series of negative growth controls (medium + bacteria + triclosan (Tc)) and positive growth control (G+) were also included in the analysis. The results are shown in Figure 3.3a. All the ABF coatings and other control samples show no toxicity.

Leachate toxicity for diatoms was assessed by introducing the microalgae into

overnight extracts (artificial sea water with nutrients) for each coating. Growth evaluation was measured after 48 hours via fluorescence of chlorophyll and reported as a fluorescence ratio to a positive growth control (fresh nutrient medium). A negative growth control (medium + bacteria + triclosan) was also included in the analysis. The results are shown in Figure 3.3b. Similar to *C. lytica*, no toxicity was observed for all the samples.

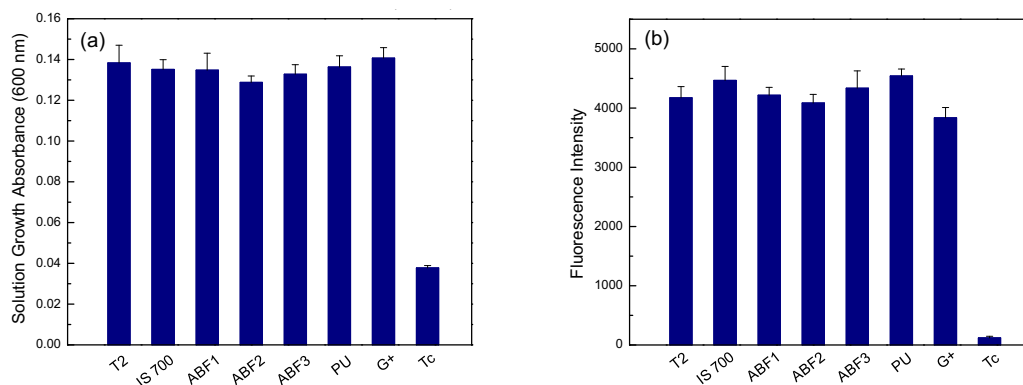


Figure 3.3 Assessment of leachate toxicity of ABF coatings and state-of-the-art coatings for (a) bacterium *C. lytica* after 24 hrs, and (b) diatom *Navicula* after 48 hrs. Error bars represent one standard deviation of the mean.

3.6.2 *Ulva* Attachment

Fouling formation is an outcome of the initial attachment of swimming *Ulva* zoospores to a suitable surface which forms sporelings adhesion consequently.¹⁸⁷ Once settled, the spores start to secrete the adhesive extracellular matrices which is a polydisperse, self-aggregating hydrophilic glycoprotein. They then undergo cross-linking with a corresponding rise in adhesion strength^{188, 189}. Mechanical properties of secreted adhesive and surface properties of *Ulva* spores is studied through SPM. Figure 3.4a

shows morphology of the spores on the surface and how they settle down on the substrate. For *Ulva* attachment, glycoprotein acts as an adhesive matrix (similar to EPS in diatoms attachment) and keeps the cell in contact with the surface which will be explained in more detail later¹⁹⁰. In SPM, adhesion is characterized by pull-off force which measures adhesion between cantilever and substrate¹⁹¹. Adhesion work is defined as pull-off force divided by the tip radius¹⁹¹. As shown in Figure 3.4b, the highest adhesion belongs to glycoprotein formed around the cell. Figure 3.4c and 3.4d depict SPM cantilever deformation and modulus of elasticity of spores, respectively. By comparing Figure 3.4c and 3.4d, dependence of the cantilever deformation on the modulus of elasticity is evident. The regions with highest elasticity show lowest cantilever deformation. The anti-biofouling property of stress-localized coatings is compared with PDMS in Figure 3.4e-3.4f. As shown, the stress-localized surface shows remarkable reduction in concentration of *Ulva* on the surface compared to PDMS. Statistical analysis of the fluorescence microscopy images reveals the concentration of *Ulva* spores on a surface in terms of percentage of colony coverage area. The analysis shows concentration of 8% for PDMS sample, while this value reduces to less than 1% (0.9 %) for ABF.

As discussed in the literature^{192, 187}, low modulus of elasticity and critical surface tension are major determinants to low adhesion of spores and sporelings. However, low modulus of elasticity leads to poor mechanical durability of the coatings. Here, through the idea of stress-localization, we have achieved both low adhesion of spores on the surface and high mechanical durability.

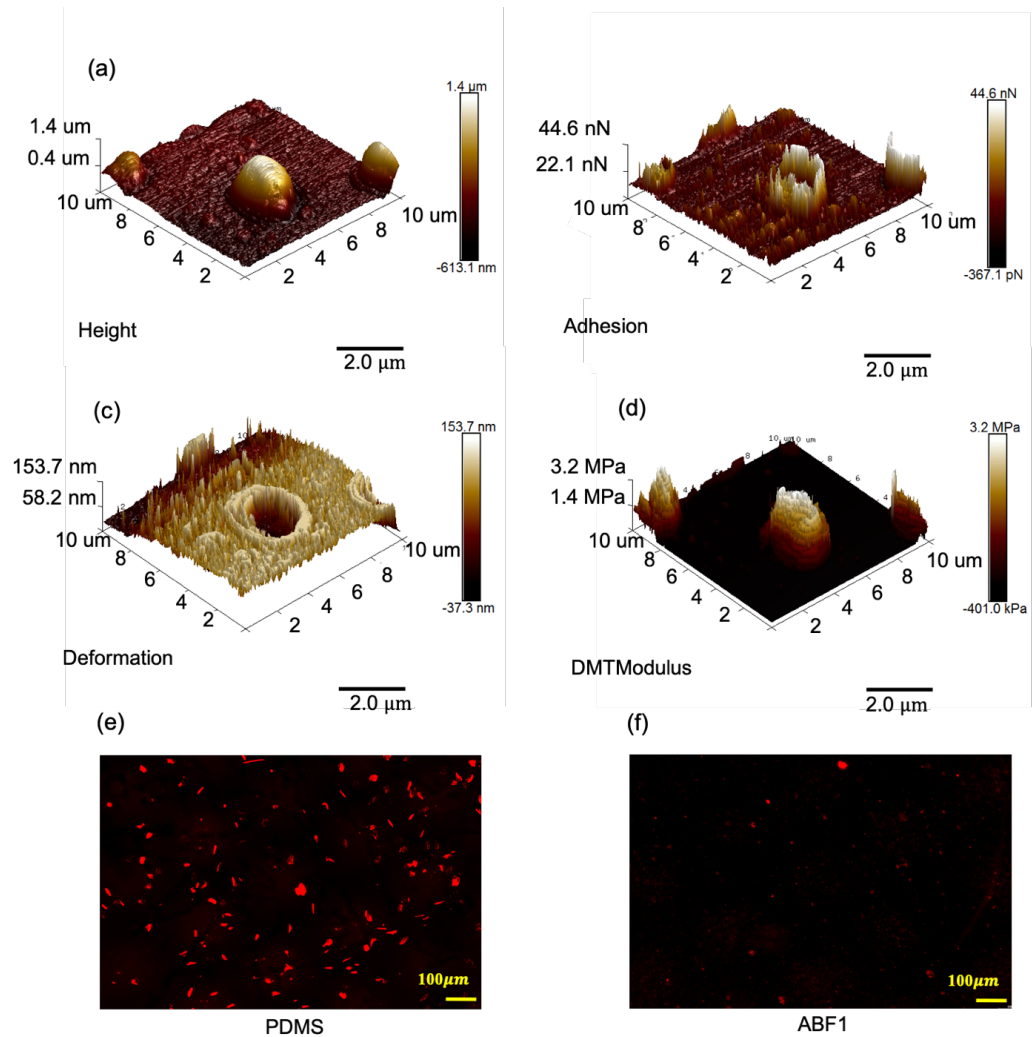


Figure 3.4 SPM analysis of *Ulva* on ABF coating showing (a) height graph, (b) adhesion, (c) deformation, and (d) elasticity modulus. *Ulva* spores attachment has been compared between (e) PDMS control sample and (f) ABF1.

3.6.3 Attachment and Adhesion of Marine Bacterium, *C. lytica*

Bacterium *C. lytica* as a component of microbial biofilm provides cues for settlement of other organisms on man-made structures¹⁹³. The results from the experimental assessment of biofilm growth and bacterium attachment are illustrated in Figure 3.5. Biofilm growth was reported as the mean absorbance value of three replicate

samples after 24 hours in Figure 3.5a. All the ABF coatings demonstrate smaller bacterial biofilm growth compared with state-of-the-arts. In the following step, the covered area was measured as presented in Figure 3.5b indicating the best result for ABF3, which is almost 20% less than Intersleek 700. Figure 3.5c shows the coated surfaces partially covered by bacterium *C. lytica*.

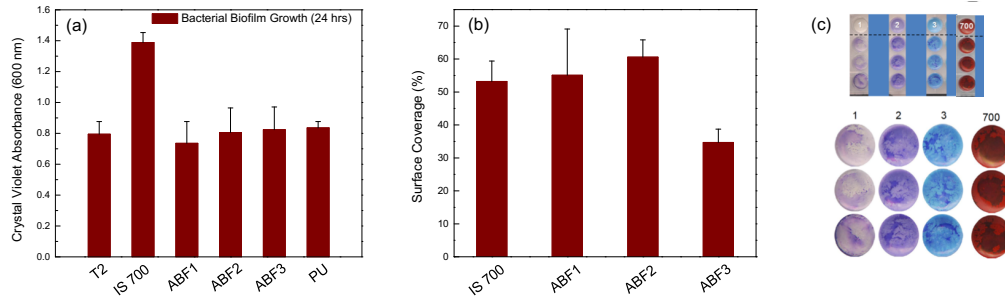


Figure 3.5 (a) Bacterial biofilm growth after 24 hours for ABF coatings, Silastic T2, Intersleek 700, and Polyurethane (PU). (b) Comparison of surface coverage for ABF and Intersleek 700. (c) Graphical representation of bacterial attachment on the coatings.

Water jet adhesion was carried out after 24 hours of bacterial biofilm growth. The first column of each plate was not treated and served as the measure of biofilm growth before water jetting. The second and third columns of each stress-localized ABF coating were jetted for 5 seconds at a pressure of 10 psi and 20 psi, respectively. Biofilm adhesion was reported as a function of percent removal, Figure 3.6a, and remained biomass measured by colorimetric method via crystal violet absorbance, Figure 3.6b. Based on the results, ABF3 possesses highest removal percentage as well as the lowest remained biomass.

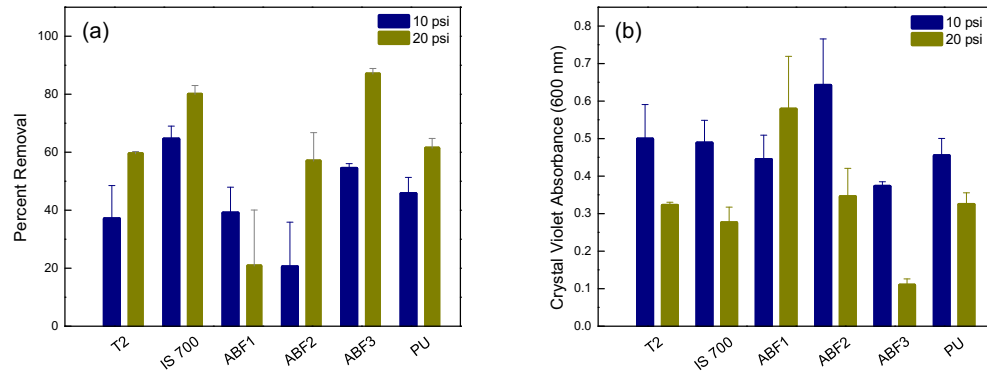


Figure 3.6 (a) Biofilm removal by exposing to water jet for two different pressures of 10 psi and 20 psi. (b) Remained biomass after exposure to water jet. Error bars represent one standard deviation of the mean.

3.6.4 Attachment and Adhesion of Diatom *Navicula*

The motility of the diatoms in contact with a surface enable them to migrate and find the most suitable coordinate for settlement^{194, 195}. Coordinate selection is not random but highly strategic and is based on diatom's potential to search for existing stalks. As diatoms seek out to find a proper coordinate, they secrete adhesive material called extracellular polymeric substances (EPS)^{138,196,197}. This material acts as a bridge between raphe and surface which results in deposition of a trail on the surface¹⁹⁸ and holds diatoms on the surface¹⁹⁹. EPS is divided into two forms: bound EPS including tightly bound (TB) and loosely bound (LB), and soluble EPS. The bound EPS forms closely to the diatom and strongly bonds to it. The soluble EPS is weakly bonded to diatom and dissolves in the fluid environment²⁰⁰. Due to preference of diatoms for agglomeration, diatoms form a raft which constitutes of each individual EPS.¹⁹⁴ The SPM study in Figure 3.7a confirms this structure for EPS around the diatoms and both tightly bound and loosely bound EPS are highlighted. Figure 3.7b shows the deformation graph which is a

representative of the SPM cantilever indentation. The highest deflection of cantilever occurs for the softest material which is EPS in this case. Less deformation can be seen for diatom due to its hard silica shield^{201, 202}. Figure 3.7c represents the maximum adhesion for EPS and also shows the deposition of adhesive complex further away from the diatom on the surface. Figure 3.7d shows high modulus of elasticity of diatom compared to its surrounding. We analyzed the concentration of diatoms on the substrates through fluorescence microscopy. The results for PDMS and ABF3 sample are shown in Figures 3.7e and 3.7f. As shown, the superior anti-biofouling characteristics of ABF coatings are evident. The concentration of diatoms on PDMS sample is 20 %, while this value for ABF3 coating is 2% indicating an order of magnitude drop in diatom accumulation. Diatom attachment and biofilm growth are shown in Figure 3.8. All the ABF coatings have almost the same order of diatom attachment similar to Intesleek 700, Silastic T2, and PU.

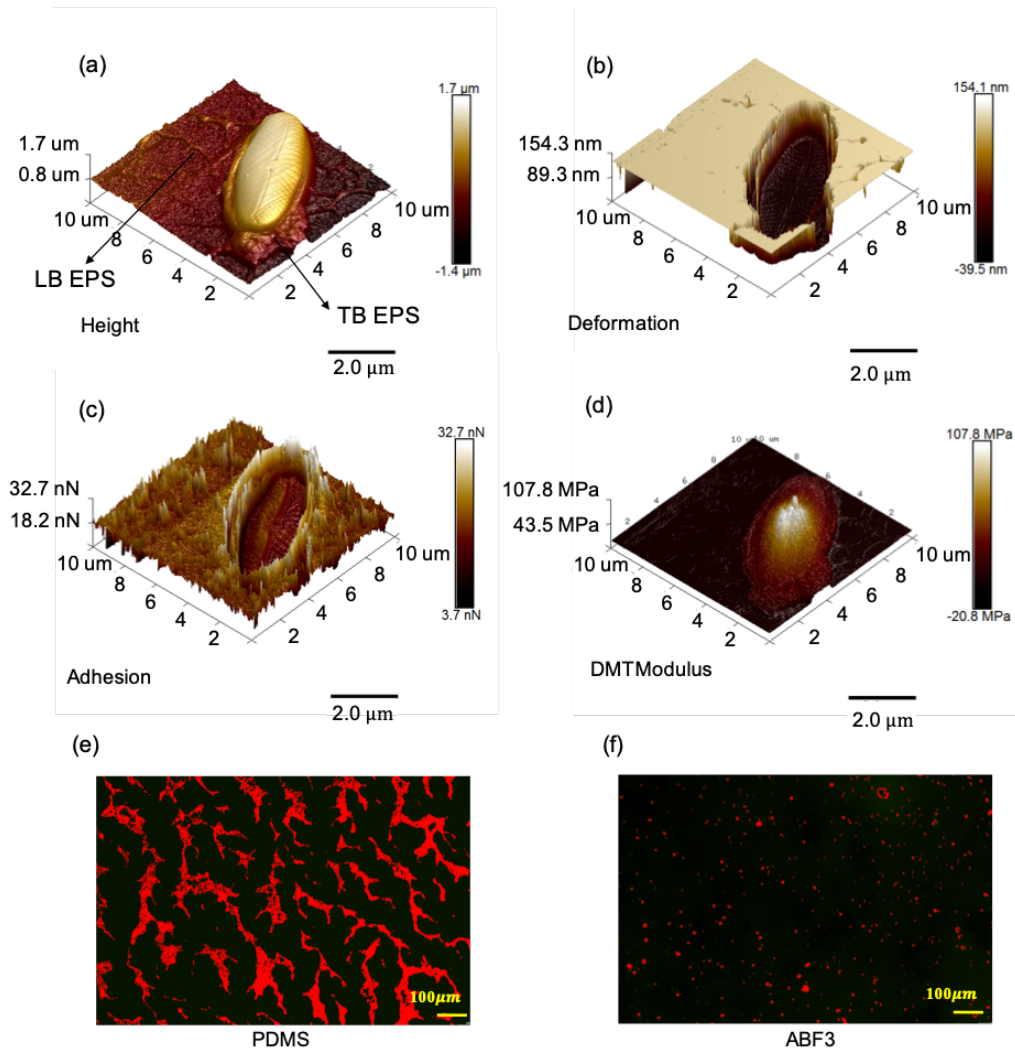


Figure 3.7 Diatom attachment and EPS formation on the surface of ABF3. (a) Height, (b) deformation, (c) adhesion, and (d) modulus of elasticity of diatom and EPS. Diatom attachment has been compared between (e) PDMS control sample and (f) ABF3.

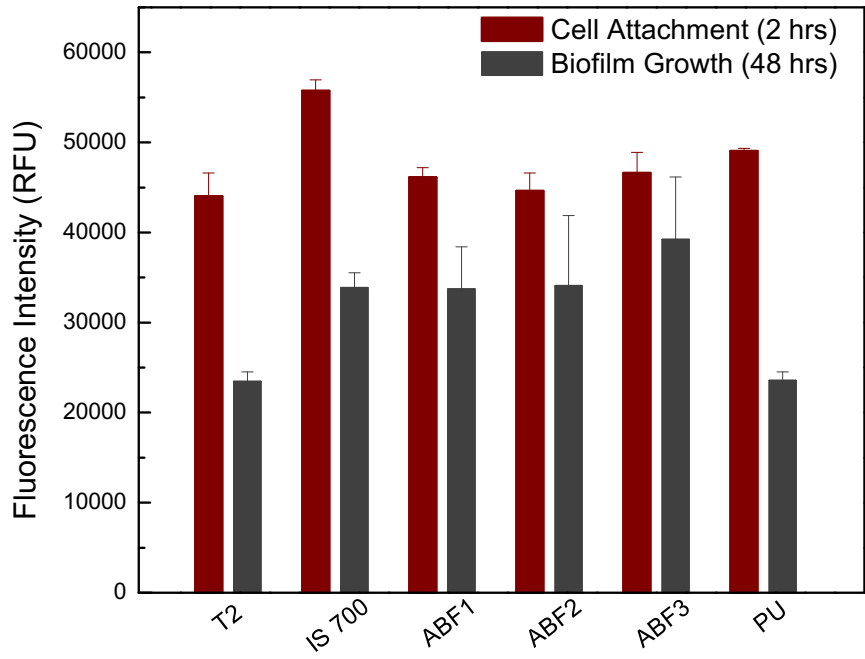


Figure 3.8 Diatom attachment measured after 2 hours and biofilm growth after 48 hours of incubation. The fluorescence values present concentration of diatoms attached to the coatings and biofilm growth on the surface. Error bars represent one standard deviation of the mean.

Water jet adhesion was conducted after 2 hours of initial cell attachment. The first column of each plate was not treated and served as the measure of cell attachment after 2 hours. The second and third column of each coating were jetted for 10 seconds at a pressure of 10 psi and 20 psi, respectively. Diatom adhesion was reported as a function of percentage removal, Figure 3.9a, and remained biomass measured by Fluorescence microscopy, Figure 3.9b. For 10 psi pressure, all the samples show the same performance. However, for 20 psi, Intersleek 700 shows slightly better performance than ABF samples.

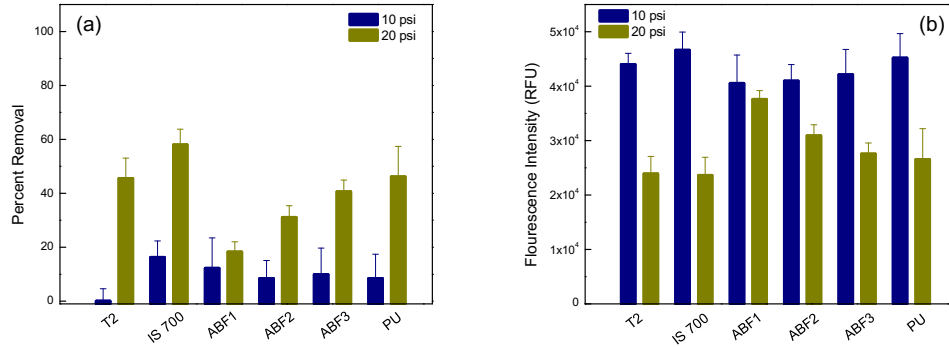


Figure 3.9 (a) Diatom *Navicula* removal by exposing to water jet for 10 seconds for two different pressures of 10 psi and 20 psi. (b) Remained biomass after exposure to water jet. Error bars represent one standard deviation of the mean.

3.6.5 Attachment and Adhesion of Barnacle

Barnacle is among the most common marine fouling organisms that has received considerable attention due to its strong and durable adhesive behaviour^{203, 204}. This specie goes through six developmental stages starting from nauplii to adult cypris stage²⁰⁵. Similar to other marine organisms, barnacle is able to sense a wide range of physical and chemical surface parameters to find the most suitable coordinate for settlement²⁰⁵. By secreting proteinaceous cement from the cement gland, barnacle produces strong adhesion after going through several functions including establishment of interfacial contact and molecular attraction between dissimilar materials^{206, 207}. Coatings were analyzed after 2 weeks of reattachment with daily feedings of brine shrimp. The number of barnacles that were able to attach to each surface were recorded and then reattachment efficiency calculated as shown in Figure 3.10a. ABF2 possesses the lowest barnacle attachment. Adhesion strength of barnacles was calculated then by dividing the measured force required to remove the barnacle by the basal area and reported in MPa. Each data

point is the mean value of the total number of barnacles that reattached to the coating surface as shown in Figure 3.10b. The small shear value required to remove the barnacle from ABF1, grants the privilege of high removal percentage. Adhesion strength is also relatively low for ABF2 and ABF3 and no significant difference can be seen with Intersleek 700. PU was not considered for barnacle test in this study as the result reported by Galhenage et al.¹⁶⁷ which is almost 0 within the accuracy of their measurements.

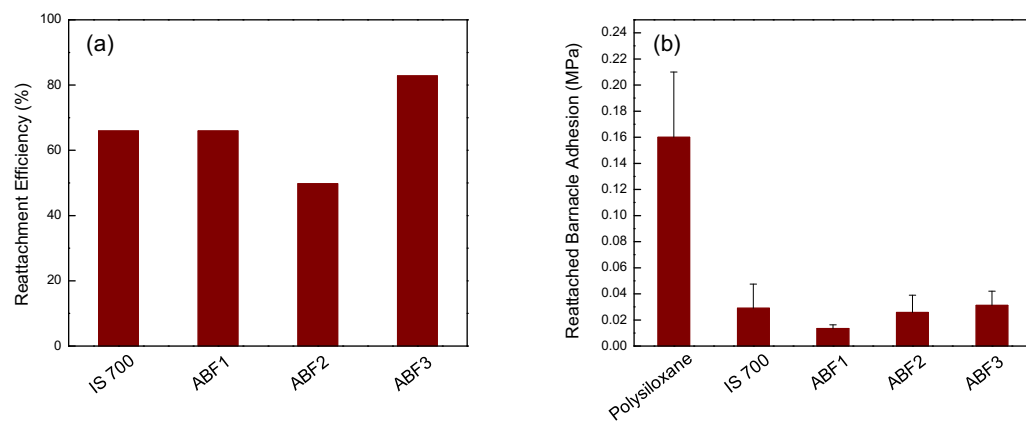


Figure 3.10 Assessment of barnacles (a) reattached efficiency after 2 weeks of daily feedings of brine shrimp, and (b) reattached adhesion on ABFs, Intersleek 700, and standard sample (polysiloxane). Error bars represent one standard deviation of the mean.

3.6.6 Attachment and Adhesion of Mussel

Mussels attach to hydrophilic and hydrophobic solid surfaces via adhesive elastomeric protein based byssal threads¹⁶⁸. This special protein equips mussels to adhere to various surfaces including metals, minerals, plastics, cement, and even low surface energy fluoropolymers in their chemically heterogenous habitat²⁰⁸. Their adhesion must be fast and strong to avoid them from getting dislodged and dashed by incoming waves²⁰⁹. Mussel *Geukensia demissa* was studied for its attachment and adhesion

behavior. Coatings were analyzed after 3 days of attachment with two feedings of phytoplankton. Each data point is the mean value of all mussels that attached to the coating surface. The mean number of mussels settled on ABF1 and ABF2 are approximately half of Intersleek 700, illustrated in Figure 3.11a. The required force for detachment of mussels from the surface was measured by using a tensile force gauge and minimum belongs to ABF1 (Figure 3.11b). PU was not tested for mussels in this study but result reported by Galhenage et al.¹⁶⁷ which is 10 N.

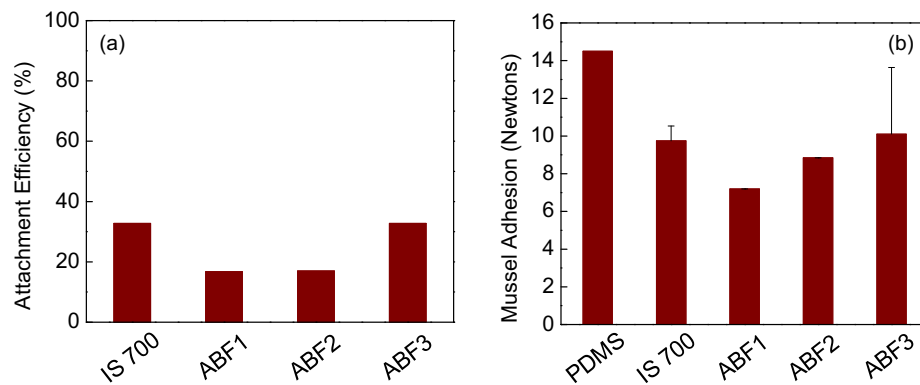


Figure 3.11 (a) Evaluation of mussel attachment on ABF and Intersleek 700 coatings. (b) Required force to remove the mussels from the surface after measuring the attachment efficiency in (a). Error bars represent one standard deviation of the mean.

3.6.7 Durability Test

We assessed mechanical, chemical and environmental durability of these surfaces. The mechanical durability was examined through abrasion of these surfaces by files and sands as shown in Figure 3.12a. The abrasion test was conducted using a Taber Reciprocating Abraser, model 5900 according to ASTM D4060. In this test, we measured material removal thickness at three different loading conditions (i.e., 1N, 5N, and 10 N)

for 1000 abrasion cycles. Abrasion test results are presented in Figure 3.13 for all three ABF coatings and standard PDMS. The primary thickness of each sample is 300 μm . Minimum thickness loss belongs to ABF 3 which has the minimum percentage of organogels. The samples are durable with no sign of degradation in response to mechanical stresses. For chemical durability, we immersed these samples in solutions with pH varying from 1.1 to 13.1 and kept the samples for a duration of 48 hrs in these solutions, Figure 3.12b. The anti-biofouling coatings show complete integrity with no sign of degradation. For environmental durability, the coated samples were examined according to ASTM G154. In this standard, the samples are exposed to 2000 hrs cycling. Each cycle includes 8 hrs exposure to UV-irradiation ($0.49 \text{ W/m}^2 \text{ nm}$ at 310 nm at 70 °C) followed by 4 hrs of condensation at 50 °C. After this test, integrity of the coatings is examined to determine any surface defects on the surface. As shown in Figure 3.12c, the coatings are intact with no degradation. Finally, we demonstrated on-field reparability of these stress-localized coatings, Figure 3.12d. The coating was damaged by a sharp object and it is repaired through spraying of the new material. The sprayed material cures and integrates in the coating. This highlight facile implementation and application of these sprayable coatings compared to the other surface-modified approaches.

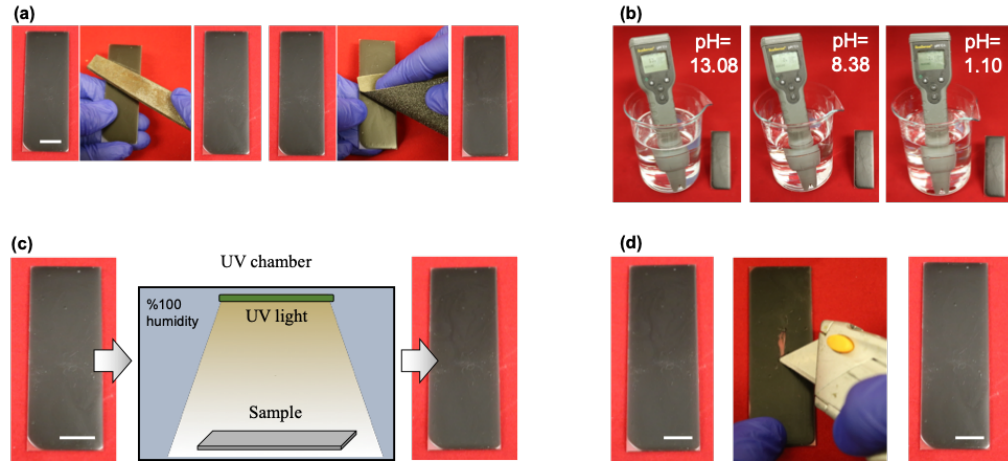


Figure 3.12 (a) Mechanical durability test of ABF3 (25% of phase II). (b) Different range of pH from 1.1 to 13.1 for chemical durability test. (c) UV test for 2000 hours. (d) On-field reparability. The scale bar is 10 mm.

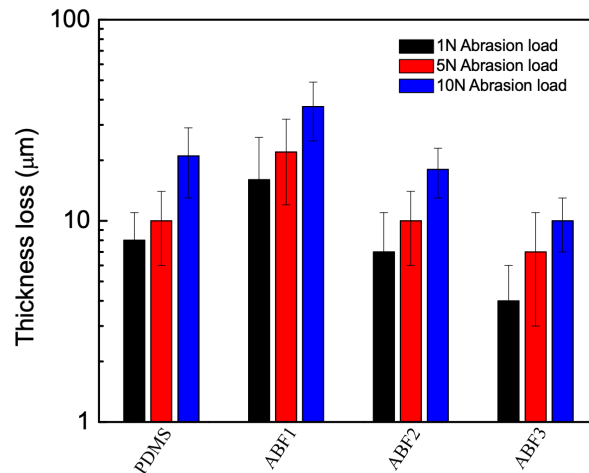


Figure 3.13 Abrasion test results for ABF coatings and PDMS. Primary thickness of each sample is 300 μm . PDMS sample has considered as the standard sample. ABF 3 with lowest concentration of organogels shows the best mechanical durability.

3.7 Summary

In summary, we have implemented the idea of stress-localization to minimize adhesion of bio-species on a surface and have developed durable anti-biofouling surfaces.

As demonstrated, these surfaces are bio-friendly and have no negative impact on marine environment. In a comprehensive study, we analyzed performance of these stress-localized surfaces with soft and hard bio-species including *Ulva*, bacteria, diatoms, barnacles and mussels. ABF1 sample provides minimal attachment to diatom, *Ulva*, barnacle and mussel. The stress-localization effect is maximum for ABF1 sample (i.e., $(g(\varphi_{II})=0.1)$) and leads to its minimal adhesion to hard bio-species. The performance of ABF1 is better than state-of-the-art anti-biofouling samples. For anti-bacterial characteristics to minimize growth, ABF3 is the winner sample in comparison to state-of-the-art and control samples. Lower concentration of second phase (i.e., organogel) may have contributed to this anti-bacterial characteristic. Stress-localized coatings provide less suitable environment for attachment of marine fouling organisms and allows to minimize adhesion of hard objects on a surface with no compromise in durability of these coatings.

References

- (1) Bar-Cohen, A.; Geisler, K. J. L. Cooling the Electronic Brain. *Mech. Eng.* **2011**, *133* (4).
- (2) Won, Y.; Cho, J.; Agonafer, D.; Asheghi, M.; Goodson, K. E. Cooling Limits for GaN HEMT Technology. *Tech. Dig. - IEEE Compd. Semicond. Integr. Circuit Symp. CSIC* **2013**, 1–5.
- (3) Lu, Z.; Salamon, T. R.; Narayanan, S.; Bagnall, K. R.; Hanks, D. F.; Antao, D. S.; Barabadi, B.; Sircar, J.; Simon, M. E.; Wang, E. N. Design and Modeling of Membrane-Based Evaporative Cooling Devices for Thermal Management of High Heat Fluxes. *IEEE Trans. Components, Packag. Manuf. Technol.* **2016**, *6* (7), 1058–1067.
- (4) Marcinichen, J. B.; Olivier, J. A.; Lamaison, N.; Thome, J. R. Advances in Electronics Cooling. *Heat Transf. Eng.* **2013**, *34* (5–6), 434–446.
- (5) Lin, Z.; Wang, S.; Huo, J.; Hu, Y.; Chen, J.; Zhang, W.; Lee, E. Heat Transfer Characteristics and LED Heat Sink Application of Aluminum Plate Oscillating Heat Pipes. *Appl. Therm. Eng.* **2011**, *31* (14–15), 2221–2229.
- (6) Kim, L.; Choi, J. H.; Jang, S. H.; Shin, M. W. Thermal Analysis of LED Array System with Heat Pipe. *Thermochim. Acta* **2007**, *455* (1–2), 21–25.
- (7) Garimella, S. V.; Fleischer, A. S.; Murthy, J. Y.; Keshavarzi, A.; Prasher, R.; Patel, C.; Bhavnani, S. H.; Venkatasubramanian, R.; Mahajan, R.; Joshi, Y.; et al. Thermal Challenges in Next-Generation Electronic Systems. *IEEE Trans. Components Packag. Technol.* **2008**, *31* (4), 801–815.
- (8) Andresen, M.; Liserre, M. Impact of Active Thermal Management on Power Electronics Design. *Microelectron. Reliab.* **2014**, *54* (9–10), 1935–1939.

- (9) Lee, A.; Moon, M. W.; Lim, H.; Kim, W. D.; Kim, H. Y. Water Harvest via Dewing. *Langmuir* **2012**, *28* (27), 10183–10191.
- (10) El-Dessouky, H. T.; Ettouney, H. M. Multiple-Effect Evaporation Desalination Systems: Thermal Analysis. *Desalination* **1999**, *125* (1–3), 259–276.
- (11) Humplik, T.; Lee, J.; O’Hern, S. C.; Fellman, B. A.; Baig, M. A.; Hassan, S. F.; Atieh, M. A.; Rahman, F.; Laoui, T.; Karnik, R.; et al. Nanostructured Materials for Water Desalination. *Nanotechnology* **2011**, *22* (29).
- (12) Semiat, R. Energy Issues in Desalination Processes. *Environ. Sci. Technol.* **2008**, *42* (22), 8193–8201.
- (13) Kabeel, A. E.; El-Said, E. M. S. A Hybrid Solar Desalination System of Air Humidification, Dehumidification and Water Flashing Evaporation: Part II. Experimental Investigation. *Desalination* **2014**, *341* (1), 50–60.
- (14) Ghasemi, H.; Ni, G.; Marconnet, A. M.; Loomis, J.; Yerci, S.; Miljkovic, N.; Chen, G. Solar Steam Generation by Heat Localization. *Nat. Commun.* **2014**, *5*, 1–7.
- (15) Ni, G.; Li, G.; Boriskina, S. V.; Li, H.; Yang, W.; Zhang, T. J.; Chen, G. Steam Generation under One Sun Enabled by a Floating Structure with Thermal Concentration. *Nat. Energy* **2016**, *1* (9).
- (16) Laing, D.; Bahl, C.; Bauer, T.; Lehmann, D.; Steinmann, W. D. Thermal Energy Storage for Direct Steam Generation. *Sol. Energy* **2011**, *85* (4), 627–633.
- (17) des Rieux, A.; Fievez, V.; Garinot, M.; Schneider, Y. J.; Pr eat, V. Nanoparticles as Potential Oral Delivery Systems of Proteins and Vaccines: A Mechanistic Approach. *J. Control. Release* **2006**, *116* (1), 1–27.

- (18) Sefiane, K. On the Formation of Regular Patterns from Drying Droplets and Their Potential Use for Bio-Medical Applications. *J. Bionic Eng.* **2010**, 7 (SUPPL.), S82–S93.
- (19) Goto, E.; Matsumoto, Y.; Kamoi, M.; Endo, K.; Ishida, R.; Dogru, M.; Kaido, M.; Kojima, T.; Tsubota, K. Tear Evaporation Rates in Sjögren Syndrome and Non-Sjögren Dry Eye Patients. *Am. J. Ophthalmol.* **2007**, 144 (1), 81–86.
- (20) Lozano, A. L.; Cherblanc, F.; Cousin, B.; Bénét, J. C. Experimental Study and Modelling of the Water Phase Change Kinetics in Soils. *Eur. J. Soil Sci.* **2008**, 59 (5), 939–949.
- (21) Li, H.; Harvey, J.; Ge, Z. Experimental Investigation on Evaporation Rate for Enhancing Evaporative Cooling Effect of Permeable Pavement Materials. *Constr. Build. Mater.* **2014**, 65, 367–375.
- (22) Haryanto, A.; Fernando, S.; Murali, N.; Adhikari, S. Current Status of Hydrogen Production Techniques by Steam Reforming of Ethanol: A Review. *Energy and Fuels* **2005**, 19 (5), 2098–2106.
- (23) Hansen, J. D.; Johnson, J. A.; Winter, D. A. History and Use of Heat in Pest Control: A Review. *Int. J. Pest Manag.* **2011**, 57 (4), 267–289.
- (24) Raj, R.; Kunkelmann, C.; Stephan, P.; Plawsky, J.; Kim, J. Contact Line Behavior for a Highly Wetting Fluid under Superheated Conditions. *Int. J. Heat Mass Transf.* **2012**, 55 (9–10), 2664–2675.
- (25) Ibrahim, K.; Abd Rabbo, M. F.; Gambaryan-Roisman, T.; Stephan, P. Experimental Investigation of Evaporative Heat Transfer Characteristics at the 3-Phase Contact Line. *Exp. Therm. Fluid Sci.* **2010**, 34 (8), 1036–1041.
- (26) Gokhale, S. J.; Plawsky, J. L.; Wayner, P. C. The CVB Experiment Constrained Bubble

Nucleation In Microgravity Spreading , Evaporation , and Contact Line Dynamics of Surfactant-Laden Microdrops. **2011**, No. October.

- (27) Migliaccio, C. P.; Dhavaleswarapu, H. K.; Garimella, S. V. Temperature Measurements near the Contact Line of an Evaporating Meniscus V-Groove. *Int. J. Heat Mass Transf.* **2011**, *54* (7–8), 1520–1526.
- (28) Plawsky, J. L.; Fedorov, A. G.; Garimella, S. V.; Ma, H. B.; Maroo, S. C.; Chen, L.; Nam, Y. Nano-and Microstructures for Thin-Film Evaporation-A Review. *Nanoscale Microscale Thermophys. Eng.* **2014**, *18* (3), 251–269.
- (29) Jafari, P.; Masoudi, A.; Irajizad, P.; Nazari, M.; Kashyap, V.; Eslami, B.; Ghasemi, H. Evaporation Mass Flux: A Predictive Model and Experiments. *Langmuir* **2018**, *34* (39), 11676–11684.
- (30) Persad, A. H.; Ward, C. A. Expressions for the Evaporation and Condensation Coefficients in the Hertz-Knudsen Relation. *Chem. Rev.* **2016**, *116* (14), 7727–7767.
- (31) Maroo, S. C.; Chung, J. N. Heat Transfer Characteristics and Pressure Variation in a Nanoscale Evaporating Meniscus. *Int. J. Heat Mass Transf.* **2010**, *53* (15–16), 3335–3345.
- (32) Courbin, L.; Denieul, E.; Dressaire, E.; Roper, M.; Ajdari, A.; Stone, H. A. Imbibition by Polygonal Spreading on Microdecorated Surfaces. *Nat. Mater.* **2007**, *6* (9), 661–664.
- (33) Ojha, M.; Chatterjee, A.; Dalakos, G.; Wayner, P. C.; Plawsky, J. L. Role of Solid Surface Structure on Evaporative Phase Change from a Completely Wetting Corner Meniscus. *Phys. Fluids* **2010**, *22* (5), 1–15.
- (34) Chen, W.; Lin, J. Thermal Analysis of Nanofluids on the Thin Film Evaporation of Meniscus. *Heat Transf. - Asian Res.* **2016**, *45* (6), 578–593.

- (35) Wang, H.; Garimella, S. V.; Murthy, J. Y. Characteristics of an Evaporating Thin Film in a Microchannel. *Int. J. Heat Mass Transf.* **2007**, *50* (19–20), 3933–3942.
- (36) Ramon, G.; Oron, A. Capillary Rise of a Meniscus with Phase Change. *J. Colloid Interface Sci.* **2008**, *327* (1), 145–151.
- (37) Xiao, R.; Wang, E. N. Microscale Liquid Dynamics and the Effect on Macroscale Propagation in Pillar Arrays. *Langmuir* **2011**, *27* (17), 10360–10364.
- (38) Liu, W.; Li, Y.; Cai, Y.; Sekulic, D. P. Capillary Rise of Liquids over a Microstructured Solid Surface. *Langmuir* **2011**, *27* (23), 14260–14266.
- (39) Ranjan, R.; Murthy, J. Y.; Garimella, S. V. Analysis of the Wicking and Thin-Film Evaporation Characteristics of Microstructures. *J. Heat Transfer* **2009**, *131* (10), 1–11.
- (40) Ward, C. A.; Duan, F. Turbulent Transition of Thermocapillary Flow Induced by Water Evaporation. *Phys. Rev. E - Stat. Physics, Plasmas, Fluids, Relat. Interdiscip. Top.* **2004**, *69* (5), 10.
- (41) Wayner, P. C.; Kao, Y. K.; LaCroix, L. V. The Interline Heat-Transfer Coefficient of an Evaporating Wetting Film. *Int. J. Heat Mass Transf.* **1976**, *19* (5), 487–492.
- (42) Kharangate, C. R.; Lee, H.; Mudawar, I. Computational Modeling of Turbulent Evaporating Falling Films. *Int. J. Heat Mass Transf.* **2015**, *81*, 52–62.
- (43) Carey, V. P.; Wemhoff, A. P. Disjoining Pressure Effects in Ultra-Thin Liquid Films in Micropassages - Comparison of Thermodynamic Theory with Predictions of Molecular Dynamics Simulations. *J. Heat Transfer* **2006**, *128* (12), 1276–1284.
- (44) Dhavaleswarapu, H. K. Microscale Temperature Measurements Near the Triple Line of an

Evaporating Thin Liquid Film Measurements Near the Triple Line of an Evaporating Thin. **2009**.

- (45) Sefiane, K.; Ward, C. A. Recent Advances on Thermocapillary Flows and Interfacial Conditions during the Evaporation of Liquids. *Adv. Colloid Interface Sci.* **2007**, *134–135*, 201–223.
- (46) Wen, R.; Ma, X.; Lee, Y. C.; Yang, R. Liquid-Vapor Phase-Change Heat Transfer on Functionalized Nanowired Surfaces and Beyond. *Joule* **2018**, *2* (11), 2307–2347.
- (47) Cho, H. J.; Preston, D. J.; Zhu, Y.; Wang, E. N. Nanoengineered Materials for Liquid-Vapour Phase-Change Heat Transfer. *Nat. Rev. Mater.* **2016**, *2* (2), 1–17.
- (48) Akkus, Y.; Koklu, A.; Beskok, A. Atomic Scale Interfacial Transport at an Extended Evaporating Meniscus. *Langmuir* **2019**, *35* (13), 4491–4497.
- (49) Sadaghiani, A. K.; Saadi, N. S.; Parapari, S. S.; Karabacak, T.; Keskinöz, M.; Koşar, A. Boiling Heat Transfer Performance Enhancement Using Micro and Nano Structured Surfaces for High Heat Flux Electronics Cooling Systems. *Appl. Therm. Eng.* **2017**, *127*, 484–498.
- (50) Antao, D. S.; Adera, S.; Zhu, Y.; Farias, E.; Raj, R.; Wang, E. N. Dynamic Evolution of the Evaporating Liquid-Vapor Interface in Micropillar Arrays. *Langmuir* **2016**, *32* (2), 519–526.
- (51) Zhang, L.; Zhu, Y.; Lu, Z.; Zhao, L.; Bagnall, K. R.; Rao, S. R.; Wang, E. N. Characterization of Thin Film Evaporation in Micropillar Wicks Using Micro-Raman Spectroscopy. *Appl. Phys. Lett.* **2018**, *113* (16).
- (52) Wang, S.; Chen, H. H.; Chen, C. L. Enhanced Flow Boiling in Silicon Nanowire-Coated

- Manifold Microchannels. *Appl. Therm. Eng.* **2019**, *148* (October 2018), 1043–1057.
- (53) Kim, B. S.; Choi, G.; Shim, D. Il; Kim, K. M.; Cho, H. H. Surface Roughening for Hemi-Wicking and Its Impact on Convective Boiling Heat Transfer. *Int. J. Heat Mass Transf.* **2016**, *102*, 1100–1107.
- (54) Cai, S. Q.; Bhunia, A. Characterization of Phase Change Heat and Mass Transfers in Monoporous Silicon Wick Structures. *J. Heat Transfer* **2014**, *136* (7).
- (55) Adera, S.; Antao, D.; Raj, R.; Wang, E. N. Design of Micropillar Wicks for Thin-Film Evaporation. *Int. J. Heat Mass Transf.* **2016**, *101*, 280–294.
- (56) Farokhnia, N.; Irajizad, P.; Sajadi, S. M.; Ghasemi, H. Rational Micro/Nanostructuring for Thin-Film Evaporation. *J. Phys. Chem. C* **2016**, *120* (16), 8742–8750.
- (57) Zhu, Y.; Antao, D. S.; Lu, Z.; Somasundaram, S.; Zhang, T.; Wang, E. N. Prediction and Characterization of Dry-out Heat Flux in Micropillar Wick Structures. *Langmuir* **2016**, *32* (7), 1920–1927.
- (58) Ranjan, R.; Murthy, J. Y.; Garimella, S. V. A Microscale Model for Thin-Film Evaporation in Capillary Wick Structures. *Int. J. Heat Mass Transf.* **2011**, *54* (1–3), 169–179.
- (59) Liu, T.; Dunham, M. T.; Jung, K. W.; Chen, B.; Asheghi, M.; Goodson, K. E. Characterization and Thermal Modeling of a Miniature Silicon Vapor Chamber for Die-Level Heat Redistribution. *Int. J. Heat Mass Transf.* **2020**, *152*, 119569.
- (60) Vaartstra, G.; Lu, Z.; Wang, E. N. Simultaneous Prediction of Dryout Heat Flux and Local Temperature for Thin Film Evaporation in Micropillar Wicks. *Int. J. Heat Mass Transf.* **2019**, *136*, 170–177.

- (61) Coso, D.; Srinivasan, V.; Lu, M. C.; Chang, J. Y.; Majumdar, A. Enhanced Heat Transfer in Biporous Wicks in the Thin Liquid Film Evaporation and Boiling Regimes. *J. Heat Transfer* **2012**, *134* (10), 1–11.
- (62) Ryu, S.; Lee, W.; Nam, Y. Heat Transfer and Capillary Performance of Dual-Height Superhydrophilic Micropost Wicks. *Int. J. Heat Mass Transf.* **2014**, *73*, 438–444.
- (63) Kim, B. S.; Choi, G.; Shin, S.; Gemming, T.; Cho, H. H. Nano-Inspired Fluidic Interactivity for Boiling Heat Transfer: Impact and Criteria. *Sci. Rep.* **2016**, *6*, 1–11.
- (64) Huang, Z.; Fang, H.; Zhu, J. Fabrication of Silicon Nanowire Arrays with Controlled Diameter, Length, and Density. *Adv. Mater.* **2007**, *19* (5), 744–748.
- (65) Huang, Z.; Geyer, N.; Werner, P.; De Boor, J.; Gosele, U. Metal-Assisted Chemical Etching of Silicon: A Review. *Adv. Mater.* **2011**, *23* (2), 285–308.
- (66) Lu, X.; Hanrath, T.; Johnston, K. P.; Korgel, B. A. Growth of Single Crystal Silicon Nanowires in Supercritical Solution from Tethered Gold Particles on a Silicon Substrate. *Nano Lett.* **2003**, *3* (1), 93–99.
- (67) Ganguli, S.; Roy, A. K. Aligned Carbon Nanotube to Enhance through Thickness Thermal Conductivity in Adhesive Joints. *Int. SAMPE Tech. Conf.* **2006**.
- (68) Huang, H.; Liu, C.; Wu, Y.; Fan, S. Aligned Carbon Nanotube Composite Films for Thermal Management. *Adv. Mater.* **2005**, *17* (13), 1652–1656.
- (69) Cai, Q.; Bhunia, A. High Heat Flux Phase Change on Porous Carbon Nanotube Structures. *Int. J. Heat Mass Transf.* **2012**, *55* (21–22), 5544–5551.
- (70) Ji, K.; Meng, G.; Yuan, C.; Cui, E.; Li, Y.; Sun, J.; Dai, Z. Synergistic Effect of Fe and

Al₂O₃ Layers on the Growth of Vertically Aligned Carbon Nanotubes for Gecko-Inspired Adhesive Applications. *J. Manuf. Process.* **2018**, 33 (June 2017), 238–244.

- (71) Sharma, P.; Pavelyev, V.; Kumar, S.; Mishra, P.; Islam, S. S.; Tripathi, N. *Analysis on the Synthesis of Vertically Aligned Carbon Nanotubes: Growth Mechanism and Techniques*; Springer US, 2020; Vol. 31.
- (72) Chu, K. H.; Joung, Y. S.; Enright, R.; Buie, C. R.; Wang, E. N. Hierarchically Structured Surfaces for Boiling Critical Heat Flux Enhancement. *Appl. Phys. Lett.* **2013**, 102 (15).
- (73) Ravi, S.; Dharmarajan, R.; Moghaddam, S. Physics of Fluid Transport in Hybrid Biporous Capillary Wicking Microstructures. *Langmuir* **2016**, 32 (33), 8289–8297.
- (74) Ma, P.; Wang, Y.; Feng, K.; Chen, Z.; Wu, W. Hierarchical Superhydrophobic/Hydrophilic Substrates Based on Nanospheres Self-Assembly onto Micro-Pillars. *Mater. Res. Express* **2015**, 1 (4).
- (75) Wang, Z.; Zhao, J.; Bagal, A.; Dandley, E. C.; Oldham, C. J.; Fang, T.; Parsons, G. N.; Chang, C. H. Wicking Enhancement in Three-Dimensional Hierarchical Nanostructures. *Langmuir* **2016**, 32 (32), 8029–8033.
- (76) Nam, Y.; Sharratt, S.; Cha, G.; Ju, Y. S. Characterization and Modeling of the Heat Transfer Performance of Nanostructured Cu Micropost Wicks. *J. Heat Transfer* **2011**, 133 (10).
- (77) Nam, Y.; Sharratt, S.; Byon, C.; Kim, S. J.; Ju, Y. S. Fabrication and Characterization of the Capillary Performance of Superhydrophilic Cu Micropost Arrays. *J. Microelectromechanical Syst.* **2010**, 19 (3), 581–588.
- (78) Nam, Y.; Ju, Y. S. A Comparative Study of the Morphology and Wetting Characteristics

- of Micro/Nanostructured Cu Surfaces for Phase Change Heat Transfer Applications. *J. Adhes. Sci. Technol.* **2013**, *27* (20), 2163–2176.
- (79) Ryu, S.; Han, J.; Kim, J.; Lee, C.; Nam, Y. Enhanced Heat Transfer Using Metal Foam Liquid Supply Layers for Micro Heat Spreaders. *Int. J. Heat Mass Transf.* **2017**, *108*, 2338–2345.
- (80) Sudhakar, S.; Weibel, J. A.; Zhou, F.; Dede, E. M.; Garimella, S. V. Area-Scalable High-Heat-Flux Dissipation at Low Thermal Resistance Using a Capillary-Fed Two-Layer Evaporator Wick. *Int. J. Heat Mass Transf.* **2019**, *135*, 1346–1356.
- (81) Kousalya, A. S.; Weibel, J. A.; Garimella, S. V.; Fisher, T. S. Metal Functionalization of Carbon Nanotubes for Enhanced Sintered Powder Wicks. *Int. J. Heat Mass Transf.* **2013**, *59* (1), 372–383.
- (82) Xiao, R.; Maroo, S. C.; Wang, E. N. Negative Pressures in Nanoporous Membranes for Thin Film Evaporation. *Appl. Phys. Lett.* **2013**, *102* (12), 1–5.
- (83) Wilke, K. L.; Barabadi, B.; Lu, Z.; Zhang, T.; Wang, E. N. Parametric Study of Thin Film Evaporation from Nanoporous Membranes. *Appl. Phys. Lett.* **2017**, *111* (17), 0–5.
- (84) Lu, Z.; Wilke, K. L.; Preston, D. J.; Kinefuchi, I.; Chang-Davidson, E.; Wang, E. N. An Ultrathin Nanoporous Membrane Evaporator. *Nano Lett.* **2017**, *17* (10), 6217–6220.
- (85) Hanks, D. F.; Lu, Z.; Sircar, J.; Salamon, T. R.; Antao, D. S.; Bagnall, K. R.; Barabadi, B.; Wang, E. N. Nanoporous Membrane Device for Ultra High Heat Flux Thermal Management. *Microsystems Nanoeng.* **2018**, *4* (1), 1–5.
- (86) Zhang, C.; Palko, J. W.; Barako, M. T.; Asheghi, M.; Santiago, J. G.; Goodson, K. E. Enhanced Capillary-Fed Boiling in Copper Inverse Opals via Template Sintering. *Adv.*

Funct. Mater. **2018**, 28 (41), 1–8.

- (87) Palko, J. W.; Zhang, C.; Wilbur, J. D.; Dusseault, T. J.; Asheghi, M.; Goodson, K. E.; Santiago, J. G. Approaching the Limits of Two-Phase Boiling Heat Transfer: High Heat Flux and Low Superheat. *Appl. Phys. Lett.* **2015**, 107 (25).
- (88) Barako, M. T.; Sood, A.; Zhang, C.; Wang, J.; Kodama, T.; Asheghi, M.; Zheng, X.; Braun, P. V.; Goodson, K. E. Quasi-Ballistic Electronic Thermal Conduction in Metal Inverse Opals. *Nano Lett.* **2016**, 16 (4), 2754–2761.
- (89) Weibel, J. A.; Garimella, S. V.; North, M. T. Characterization of Evaporation and Boiling from Sintered Powder Wicks Fed by Capillary Action. *Int. J. Heat Mass Transf.* **2010**, 53 (19–20), 4204–4215.
- (90) Semenic, T.; Catton, I. Experimental Study of Biporous Wicks for High Heat Flux Applications. *Int. J. Heat Mass Transf.* **2009**, 52 (21–22), 5113–5121.
- (91) Palko, J. W.; Lee, H.; Zhang, C.; Dusseault, T. J.; Maitra, T.; Won, Y.; Agonafer, D. D.; Moss, J.; Houshmand, F.; Rong, G.; et al. Extreme Two-Phase Cooling from Laser-Etched Diamond and Conformal, Template-Fabricated Microporous Copper. *Adv. Funct. Mater.* **2017**, 27 (45), 1–8.
- (92) Wen, R.; Xu, S.; Lee, Y. C.; Yang, R. Capillary-Driven Liquid Film Boiling Heat Transfer on Hybrid Mesh Wicking Structures. *Nano Energy* **2018**, 51 (June), 373–382.
- (93) Dai, X.; Yang, F.; Yang, R.; Lee, Y. C.; Li, C. Micromembrane-Enhanced Capillary Evaporation. *Int. J. Heat Mass Transf.* **2013**, 64, 1101–1108.
- (94) Ward, C. A.; Findlay, R. D.; Rizk, M. Statistical Rate Theory of Interfacial Transport. I. Theoretical Development. *J. Chem. Phys.* **1982**, 76 (11), 5599–5605.

- (95) Ghasemi, H.; Ward, C. A. Energy Transport by Thermocapillary Convection during Sessile-Water-Droplet Evaporation. *Phys. Rev. Lett.* **2010**, *105* (13).
- (96) Ghasemi, H.; Ward, C. A. Mechanism of Sessile Water Droplet Evaporation: Kapitza Resistance at the Solid-Liquid Interface. *J. Phys. Chem. C* **2011**, *115* (43), 21311–21319.
- (97) Yu, Q.; Cai, S.; Zhu, Z.; Liu, Q.; Zhou, B. Droplet Image Feedback Control System in Evaporation Experiment. *Microgravity Sci. Technol.* **2010**, *22* (2), 139–144.
- (98) Davis, E. J. A History and State-of-the-Art of Accommodation Coefficients. *Atmos. Res.* **2006**, *82* (3–4), 561–578.
- (99) Nazari, M.; Masoudi, A.; Jafari, P.; Irajizad, P.; Kashyap, V.; Ghasemi, H. Ultrahigh Evaporative Heat Fluxes in Nanoconfined Geometries. *Langmuir* **2019**, *35* (1), 78–85.
- (100) Li, Y.; Alibakhshi, M. A.; Zhao, Y.; Duan, C. Exploring Ultimate Water Capillary Evaporation in Nanoscale Conduits. *Nano Lett.* **2017**, *17* (8), 4813–4819.
- (101) Li, Y.; Chen, H.; Xiao, S.; Alibakhshi, M. A.; Lo, C. W.; Lu, M. C.; Duan, C. Ultrafast Diameter-Dependent Water Evaporation from Nanopores. *ACS Nano* **2019**, *13* (3), 3363–3372.
- (102) Narayanan, S.; Fedorov, A. G.; Joshi, Y. K. Interfacial Transport of Evaporating Water Confined in Nanopores. *Langmuir* **2011**, *27* (17), 10666–10676.
- (103) Lu, Z.; Narayanan, S.; Wang, E. N. Modeling of Evaporation from Nanopores with Nonequilibrium and Nonlocal Effects. *Langmuir* **2015**, *31* (36), 9817–9824.
- (104) Buffone, C.; Sefiane, K. Investigation of Thermocapillary Convective Patterns and Their Role in the Enhancement of Evaporation from Pores. *Int. J. Multiph. Flow* **2004**, *30* (9),

1071–1091.

- (105) Wang, Z.; Liu, Y.; Tao, P.; Shen, Q.; Yi, N.; Zhang, F.; Liu, Q.; Song, C.; Zhang, D.; Shang, W.; et al. Bio-Inspired Evaporation through Plasmonic Film of Nanoparticles at the Air-Water Interface. *Small* **2014**, *10* (16), 3234–3239.
- (106) Al-Zareer, M.; Dincer, I.; Rosen, M. A. A Review of Novel Thermal Management Systems for Batteries. *Int. J. Energy Res.* **2018**, *42* (10), 3182–3205.
- (107) Moore, A. L.; Shi, L. Emerging Challenges and Materials for Thermal Management of Electronics. *Mater. Today* **2014**, *17* (4), 163–174.
- (108) Wen, L.; Tian, Y.; Jiang, L. Bioinspired Super-Wettability from Fundamental Research to Practical Applications. *Angew. Chemie - Int. Ed.* **2015**, *54* (11), 3387–3399.
- (109) Quéré, D. Wetting and Roughness. *Annu. Rev. Mater. Res.* **2008**, *38*, 71–99.
- (110) Sohel Murshed, S. M.; Nieto de Castro, C. A. A Critical Review of Traditional and Emerging Techniques and Fluids for Electronics Cooling. *Renew. Sustain. Energy Rev.* **2017**, *78* (April), 821–833.
- (111) Rahman, M. M.; Ölçeroglu, E.; McCarthy, M. Role of Wickability on the Critical Heat Flux of Structured Superhydrophilic Surfaces. *Langmuir* **2014**, *30* (37), 11225–11234.
- (112) Shojaeian, M.; Koşar, A. Pool Boiling and Flow Boiling on Micro- and Nanostructured Surfaces. *Exp. Therm. Fluid Sci.* **2015**, *63*, 45–73.
- (113) Mori, S.; Utaka, Y. Critical Heat Flux Enhancement by Surface Modification in a Saturated Pool Boiling: A Review. *Int. J. Heat Mass Transf.* **2017**, *108*, 2534–2557.
- (114) Shi, B.; Wang, Y. B.; Chen, K. Pool Boiling Heat Transfer Enhancement with Copper

Nanowire Arrays. *Appl. Therm. Eng.* **2015**, *75*, 115–121.

- (115) Li, D.; Wu, G. S.; Wang, W.; Wang, Y. D.; Liu, D.; Zhang, D. C.; Chen, Y. F.; Peterson, G. P.; Yang, R. Enhancing Flow Boiling Heat Transfer in Microchannels for Thermal Management with Monolithically-Integrated Silicon Nanowires. *Nano Lett.* **2012**, *12* (7), 3385–3390.
- (116) Yang, F.; Dai, X.; Peles, Y.; Cheng, P.; Khan, J.; Li, C. Flow Boiling Phenomena in a Single Annular Flow Regime in Microchannels (II): Reduced Pressure Drop and Enhanced Critical Heat Flux. *Int. J. Heat Mass Transf.* **2014**, *68* (II), 716–724.
- (117) Shin, S.; Choi, G.; Rallabandi, B.; Lee, D.; Shim, D. II; Kim, B. S.; Kim, K. M.; Cho, H. H. Enhanced Boiling Heat Transfer Using Self-Actuated Nanobimorphs. *Nano Lett.* **2018**, *18* (10), 6392–6396.
- (118) Gregorčič, P.; Zupančič, M.; Golobič, I. Scalable Surface Microstructuring by a Fiber Laser for Controlled Nucleate Boiling Performance of High- and Low-Surface-Tension Fluids. *Sci. Rep.* **2018**, *8* (1), 1–8.
- (119) Li, J.; Fu, W.; Zhang, B.; Zhu, G.; Miljkovic, N. Ultrascalable Three-Tier Hierarchical Nanoengineered Surfaces for Optimized Boiling. *ACS Nano* **2019**, *13* (12), 14080–14093.
- (120) Wu, F.; Ze, H.; Chen, S.; Gao, X. High-Efficiency Boiling Heat Transfer Interfaces Composed of Electroplated Copper Nanocone Cores and Low-Thermal-Conductivity Nickel Nanocone Coverings. *ACS Appl. Mater. Interfaces* **2020**, *12* (35), 39902–39909.
- (121) Li, Y.; Zhang, K.; Lu, M. C.; Duan, C. Single Bubble Dynamics on Superheated Superhydrophobic Surfaces. *Int. J. Heat Mass Transf.* **2016**, *99*, 521–531.
- (122) Wen, R.; Li, Q.; Wang, W.; Latour, B.; Li, C. H.; Li, C.; Lee, Y. C.; Yang, R. Enhanced

- Bubble Nucleation and Liquid Rewetting for Highly Efficient Boiling Heat Transfer on Two-Level Hierarchical Surfaces with Patterned Copper Nanowire Arrays. *Nano Energy* **2017**, *38* (November), 59–65.
- (123) Bigham, S.; Fazeli, A.; Moghaddam, S. Physics of Microstructures Enhancement of Thin Film Evaporation Heat Transfer in Microchannels Flow Boiling. *Sci. Rep.* **2017**, *7* (November 2016), 1–11.
- (124) Jia, Y. T.; Xia, G. D.; Zong, L. X.; Ma, D. D.; Tang, Y. X. A Comparative Study of Experimental Flow Boiling Heat Transfer and Pressure Drop Characteristics in Porous-Wall Microchannel Heat Sink. *Int. J. Heat Mass Transf.* **2018**, *127*, 818–833.
- (125) Zou, A.; Singh, D. P.; Maroo, S. C. Early Evaporation of Microlayer for Boiling Heat Transfer Enhancement. *Langmuir* **2016**, *32* (42), 10808–10814.
- (126) Lu, Z.; Wilke, K. L.; Preston, D. J.; Kinefuchi, I.; Chang-Davidson, E.; Wang, E. N. Supplemental Information: An Ultrathin Nanoporous Membrane Evaporator. *Nano Lett.* **2017**, *17* (10), 6217–6220.
- (127) Hu, H.; Sun, Y. Effect of Nanostructures on Heat Transfer Coefficient of an Evaporating Meniscus. *Int. J. Heat Mass Transf.* **2016**, *101*, 878–885.
- (128) Tien, C. L. A Hydrodynamic Model for Nucleate Pool Boiling. *Int. J. Heat Mass Transf.* **1962**, *5* (6), 533–540.
- (129) Zuber, N. The Dynamics of Vapor Bubbles in Nonuniform Temperature Fields. *Int. J. Heat Mass Transf.* **1961**, *2* (1–2), 83–98.
- (130) Callow, J. A.; Callow, M. E. Trends in the Development of Environmentally Friendly Fouling-Resistant Marine Coatings. *Nat. Commun.* **2011**, *2* (1).

- (131) Terlizzi, A.; Frascchetti, S.; Gianguzza, P.; Faimali, M.; Boero, F. Environmental Impact of Antifouling Technologies : State of the Art and Perspectives. *Environ. Sci. Technol.* **2001**, *35* (3), 311–317.
- (132) Yebra, D. M.; Kiil, S.; Dam-Johansen, K. Antifouling Technology - Past, Present and Future Steps towards Efficient and Environmentally Friendly Antifouling Coatings. *Prog. Org. Coatings* **2004**, *50* (2), 75–104.
- (133) Kirschner, C. M.; Brennan, A. B. Bio-Inspired Antifouling Strategies. *Annu. Rev. Mater. Res.* **2012**, *42* (1), 211–229.
- (134) Chambers, L. D.; Stokes, K. R.; Walsh, F. C.; Wood, R. J. K. Modern Approaches to Marine Antifouling Coatings. *Surf. Coatings Technol.* **2006**, *201* (6), 3642–3652.
- (135) Schultz, M.; Bendick, J.; Holm, E.; Hertel, W. Economic Impact of Biofouling on a Naval Surface Ship. *Biofouling* **2011**, *27*, 87–98.
- (136) Dürr, S.; Thomason, J. C. *Biofouling*, 1st ed.; WILEY-BLACKWELL: Chichester, 2010.
- (137) Videla, H. A. *Manual of Biocorrosion*, 1st ed.; McCombs, K., Ed.; CRS Press: Boca Raton, 1996.
- (138) Lejars, M.; Margailan, A.; Bressy, C. Fouling Release Coatings: A Nontoxic Alternative to Biocidal Antifouling Coatings. *Chem. Rev.* **2012**, *112* (8), 4347–4390.
- (139) Callow, M. E. C. *Antifouling Compounds*; Springer, Berlin, Heidelberg, 2006.
- (140) Patel, P.; Callow, M. E.; Joint, I.; Callow, J. A. Specificity in the Settlement - Modifying Response of Bacterial Biofilms towards Zoospores of the Marine Alga *Enteromorpha*. *Environ. Microbiol.* **2003**, *5* (5), 338–349.

- (141) Costerton, J. W. Introduction to Biofilm. *Int. J. Antimicrob. Agents* **1999**, *11* (3–4), 217–221.
- (142) Jain, A.; Bhosle, N. B. Biochemical Composition of the Marine Conditioning Film: Implications for Bacterial Adhesion. *Biofouling* **2009**, *25*, 13–19.
- (143) Abarzua, S.; Jakubowski, S. Biotechnological Investigation for the Prevention of Biofouling. 1. Biological and Biochemical Principles for the Prevention of Biofouling. *Mar. Ecol. Prog. Ser.* **1995**, *123* (1–3), 301.
- (144) Qian, P. Y.; Lau, S. C. K.; Dahms, H. U.; Dobretsov, S.; Harder, T. Marine Biofilms as Mediators of Colonization by Marine Macroorganisms: Implications for Antifouling and Aquaculture. *Mar. Biotechnol.* **2007**, *9* (4), 399–410.
- (145) Haras, D. Biofilms and Deteriorations of Materials: From Analysis of the Phenomenon to Prevention Strategies. *Mater. Tech.* **2005**, *93*, 27–41.
- (146) Sheng, G.; Yu, H.; Li, X. Extracellular Polymeric Substances (EPS) of Microbial Aggregates in Biological Wastewater Treatment Systems : A Review. **2010**, *28*, 882–894.
- (147) Lin, H.; Zhang, M.; Wang, F.; Meng, F.; Liao, B. Q.; Hong, H.; Chen, J.; Gao, W. A Critical Review of Extracellular Polymeric Substances (EPSs) in Membrane Bioreactors: Characteristics, Roles in Membrane Fouling and Control Strategies. *J. Memb. Sci.* **2014**, *460*, 110–125.
- (148) Schumacher, J. F.; Aldred, N.; Callow, M. E.; Finlay, J. A.; Callow, J. A.; Clare, A. S.; Brennan, A. B. Species-Specific Engineered Antifouling Topographies: Correlations between the Settlement of Algal Zoospores and Barnacle Cyprids. *Biofouling* **2007**, *23* (5), 307–317.

- (149) Berntsson, K. M.; Jonsson, P. R.; Lejhall, M.; Gatenholm, P. Analysis of Behavioural Rejection of Micro-Textured Surfaces and Implications for Recruitment by the Barnacle *Balanus Improvisus*. *J. Exp. Mar. Bio. Ecol.* **2000**, *251* (1), 59–83.
- (150) Fletcher, R. L.; Callow, M. E. The Settlement, Attachment and Establishment of Marine Algal Spores. *Br. Phycol. J.* **1992**, *27* (3), 303–329.
- (151) Callow, M. E.; Fletcher, R. L. The Influence of Low Surface Energy Materials on Bioadhesion-a Review. *Int. Biodeterior. Biodegradation* **1994**, *34* (3–4), 333–348.
- (152) Liu, Y.; Zhao, Q. Influence of Surface Energy of Modified Surfaces on Bacterial Adhesion. *Biophys. Chem.* **2005**, *117* (1), 39–45.
- (153) Brady, R. F.; Singer, I. L. Mechanical Factors Favoring Release from Fouling Release Coatings. *Biofouling* **2000**, *15* (1–3), 73–81.
- (154) Champ, M. a. The Status of the Treaty to Ban TBT in Marine Antifouling Paints and Alternatives. *Proc. 24th UJNR Mar. Facil. Panel Meet.* **2001**, No. 703, 1–7.
- (155) Champ, M. A. A Review of Organotin Regulatory Strategies, Pending Actions, Related Costs and Benefits. *Sci. Total Environ.* **2000**, *258* (1–2), 21–71.
- (156) Strand, J.; Jacobsen, J. A. Accumulation and Trophic Transfer of Organotins in a Marine Food Web from the Danish Coastal Waters. *Sci. Total Environ.* **2005**, *350* (1–3), 72–85.
- (157) Evans, S. M.; Leksono, T.; McKinnell, P. D. Tributyltin Pollution: A Diminishing Problem Following Legislation Limiting the Use of TBT-Based Anti-Fouling Paints. *Mar. Pollut. Bull.* **1995**, *30* (1), 14–21.
- (158) Terlizzi, A.; Frascchetti, S.; Gianguzza, P.; Faimali, M.; Boero, F. Environmental Impact of

Antifouling Technologies : State of the Art and Perspectives. *Aquat. Conserv. Mar. Freshw. Ecosyst.* **2001**, 317 (March), 311–317.

- (159) Alzieu, C. Environmental Impact of TBT: The French Experience. *Sci. Total Environ.* **2000**, 258 (1–2), 99–102.
- (160) Krishnan, S.; Weinman, C. J.; Ober, C. K. Advances in Polymers for Anti-Biofouling Surfaces. *J. Mater. Chem.* **2008**, 18 (29), 3405.
- (161) Schmidt, D. L.; Brady, R. F.; Lam, K.; Schmidt, D. C.; Chaudhury, M. K. Contact Angle Hysteresis, Adhesion, and Marine Biofouling. *Langmuir* **2004**, 20 (7), 2830–2836.
- (162) Donald L. Schmidt, Charles E. Coburn, Benjamin M. DeKoven, Gregg E. Potter, Gregory F. Meyers, A. D. a. F. Water-Based Non-Stick Hydrophobic Coatings. *Nature* **1994**, 368, 39–41.
- (163) Qiu, H.; Hölken, I.; Gapeeva, A.; Filiz, V.; Adlung, R.; Baum, M. Development and Characterization of Mechanically Durable Silicone-Polythiourethane Composites Modified with Tetrapodal Shaped ZnO Particles for the Potential Application as Fouling-Release Coating in the Marine Sector.
- (164) Wang, Y.; Yao, X.; Wu, S.; Li, Q.; Lv, J.; Wang, J. Bioinspired Solid Organogel Materials with a Regenerable Sacrificial Alkane Surface Layer. **2017**, 1700865, 1–7.
- (165) Lv, J.; Yao, X.; Zheng, Y.; Wang, J.; Jiang, L. Antiadhesion Organogel Materials : From Liquid to Solid. **2017**, 1703032, 1–8.
- (166) Ekblad, T.; Bergstro, G.; Ederth, T.; Conlan, S. L.; Mutton, R.; Clare, A. S.; Wang, S.; Liu, Y.; Zhao, Q.; Souza, F. D.; et al. Poly (Ethylene Glycol) -Containing Hydrogel Surfaces for Antifouling Applications in Marine and Freshwater Environments Poly (

Ethylene Glycol) -Containing Hydrogel Surfaces for Antifouling Applications in Marine and Freshwater Environments. **2008**, 2775–2783.

- (167) Galhenage, T. P.; Webster, D. C.; Moreira, A. M. S.; Burgett, R. J.; Stafslie, S. J.; Vanderwal, L.; Finlay, J. A.; Franco, S. C.; Clare, A. S. Polyurethane Coatings and Their Performance as Fouling-Release Surfaces. *J. Coatings Technol. Res.* **2017**, *14* (2), 307–322.
- (168) Amini, S.; Kolle, S.; Petrone, L.; Ahanotu, O.; Sunny, S.; Sutanto, C. N.; Hoon, S.; Cohen, L.; Weaver, J. C.; Aizenberg, J.; et al. Preventing Mussel Adhesion Using Lubricant-Infused Materials. *Science (80-.)*. **2017**, *357* (6352), 668–673.
- (169) Xiao, L.; Li, J.; Mieszkin, S.; Fino, A. Di; Clare, A. S.; Callow, M. E.; Callow, J. a.; Grunze, M.; Rosenhahn, A.; Levkin, P. a. Slippery Liquid-Infused Porous Surfaces Showing Marine Antibiofouling Properties. *ACS Appl. Mater. Interfaces* **2013**, *under revi.*
- (170) Masoudi, A.; Irajizad, P.; Farokhnia, N.; Kashyap, V.; Ghasemi, H. Antiscaling Magnetic Slippery Surfaces. *ACS Appl. Mater. Interfaces* **2017**, *9* (24), 21025–21033.
- (171) Epstein, A. K.; Wong, T.-S.; Belisle, R. A.; Boggs, E. M.; Aizenberg, J. Liquid-Infused Structured Surfaces with Exceptional Anti-Biofouling Performance. *Proc. Natl. Acad. Sci.* **2012**, *109* (33), 13182–13187.
- (172) Nurioglu, A. G.; Esteves, A. C. C.; De With, G. Non-Toxic, Non-Biocide-Release Antifouling Coatings Based on Molecular Structure Design for Marine Applications. *J. Mater. Chem. B* **2015**, *3* (32), 6547–6570.
- (173) Xing, C.; Meng, F.; Quan, M.; Ding, K.; Dang, Y.; Gong, Y. Acta Biomaterialia Quantitative Fabrication , Performance Optimization and Comparison of PEG and

- Zwitterionic Polymer Antifouling Coatings. *Acta Biomater.* **2017**, *59*, 129–138.
- (174) Yeh, S.; Chen, C.; Chen, W.; Huang, C. Modi Fi Cation of Silicone Elastomer with Zwitterionic Silane for Durable Antifouling Properties. **2014**.
- (175) Leng, C.; Hung, H.; Sieggreen, O. A.; Li, Y.; Jiang, S.; Chen, Z. Probing the Surface Hydration of Nonfouling Zwitterionic and Poly(Ethylene Glycol) Materials with Isotopic Dilution Spectroscopy. **2015**, 1–6.
- (176) Zhang, L.; Cao, Z.; Bai, T.; Carr, L.; Ella-Menye, J. R.; Irvin, C.; Ratner, B. D.; Jiang, S. Zwitterionic Hydrogels Implanted in Mice Resist the Foreign-Body Reaction. *Nat. Biotechnol.* **2013**, *31* (6), 553–556.
- (177) Xie, Q.; Liu, C.; Zhang, G. Poly(Dimethylsiloxane)-Based Polyurethane with Chemically Attached Antifoulants for Durable Marine Antibiofouling. **2015**.
- (178) Zhang, H.; Chiao, M. Anti-Fouling Coatings of Poly (Dimethylsiloxane) Devices for Biological and Biomedical Applications. *J. Med. Biol. Eng.* **2015**, 143–155.
- (179) Scardino, A. J.; Nys, R. de. Mini Review: Biomimetic Models and Bioinspired Surfaces for Fouling Control. *Biofouling* **2011**, *27* (1), 73–86.
- (180) Bohn, H. F.; Federle, W. Insect Aquaplaning: Nepenthes Pitcher Plants Capture Prey with the Peristome, a Fully Wettable Water-Lubricated Anisotropic Surface. *Proc. Natl. Acad. Sci. U. S. A.* **2004**, *101* (39), 14138–14143.
- (181) Wong, T. S.; Kang, S. H.; Tang, S. K. Y.; Smythe, E. J.; Hatton, B. D.; Grinthal, A.; Aizenberg, J. Bioinspired Self-Repairing Slippery Surfaces with Pressure-Stable Omniphobicity. *Nature* **2011**, *477* (7365), 443–447.

- (182) Irajizad, P.; Al-Bayati, A.; Eslami, B.; Shafquat, T.; Nazari, M.; Jafari, P.; Kashyap, V.; Masoudi, A.; Araya, D.; Ghasemi, H. Stress-Localized Durable Icephobic Surfaces. *Mater. Horizons* **2019**.
- (183) Chaudhury, M. K.; Kim, K. H. Shear-Induced Adhesive Failure of a Rigid Slab in Contact with a Thin Confined Film. *Eur. Phys. J. E* **2007**, *23* (2), 175–183.
- (184) Irajizad, P.; Al-bayati, A.; Eslami, B.; Shafquat, T.; Nazari, M.; Jafari, P.; Kashyap, V.; Masoudi, A.; Araya, D.; Ghasemi, H. Materials Horizons. **2019**, *19*.
- (185) Urata, C.; Dunderdale, G. J.; England, M. W.; Hozumi, A. Self-Lubricating Organogels (SLUGs) with Exceptional Syneresis-Induced Anti-Sticking Properties against Viscous Emulsions and Ices. *J. Mater. Chem. A* **2015**, *3* (24), 12626–12630.
- (186) Callow, M. E.; Callow, J. A.; Conlan, S.; Clare, A. S.; Stafslie, S. Efficacy Testing of Nonbiocidal and Fouling-Release Coatings. *Biofouling Methods* **2014**, 291–316.
- (187) Krishnan, S.; Wang, N.; Ober, C. K.; Finlay, J. A.; Callow, M. E.; Callow, J. A.; Hexemer, A.; Sohn, K. E.; Kramer, E. J.; Fischer, D. A. Comparison of the Fouling Release Properties of Hydrophobic Fluorinated and Hydrophilic PEGylated Block Copolymer Surfaces: Attachment Strength of the Diatom *Navicula* and the Green Alga *Ulva*. *Biomacromolecules* **2006**, *7* (5), 1449–1462.
- (188) Schilp, S.; Kueller, A.; Rosenhahn, A.; Grunze, M.; Pettitt, M. E.; Callow, M. E.; Callow, J. A. Settlement and Adhesion of Algal Cells to Hexa(Ethylene Glycol)-Containing Self-Assembled Monolayers with Systematically Changed Wetting Properties. *Biointerphases* **2007**, *2* (4), 143–150.
- (189) Walker, G. C.; Sun, Y.; Guo, S.; Finlay, J. A.; Callow, M. E.; Callow, J. A. Surface

- Mechanical Properties of the Spore Adhesive of the Green Alga *Ulva*. *J. Adhes.* **2005**, *81* (10–11), 1101–1118.
- (190) Schilp, S.; Rosenhahn, A.; Pettitt, M. E.; Bowen, J.; Callow, M. E.; Callow, J. A.; Grunze, M. Physicochemical Properties of (Ethylene Glycol)-Containing Self-Assembled Monolayers Relevant for Protein and Algal Cell Resistance. *Langmuir* **2009**, *25* (17), 10077–10082.
- (191) Jiang, Y.; Turner, K. T. Measurement of the Strength and Range of Adhesion Using Atomic Force Microscopy. *Extrem. Mech. Lett.* **2016**, *9*, 119–126.
- (192) Reads, C. The Influence of Elastic Modulus and Thickness on the Release of the Soft-Fouling Green Alga *Ulva Linza* (Syn . Enteromorpha ... **2015**, No. February 2005.
- (193) Ekin, A.; Webster, D. C.; Daniels, J. W.; Stafslie, S. J.; Cassé, F.; Callow, J. A.; Callow, M. E. Synthesis, Formulation, and Characterization of Siloxane-Polyurethane Coatings for Underwater Marine Applications Using Combinatorial High-Throughput Experimentation. *J. Coatings Technol. Res.* **2007**, *4* (4), 435–451.
- (194) Molino, P. J.; Wetherbee, R. The Biology of Biofouling Diatoms and Their Role in the Development of Microbial Slimes. *Biofouling* **2008**, *24* (5), 365–379.
- (195) Holland, R.; Dugdale, T. M.; Wetherbee, R.; Brennan, A. B.; Finlay, J. A.; Callow, J. A.; Callow, M. E. Adhesion and Motility of Fouling Diatoms on a Silicone Elastomer. *Biofouling* **2004**, *20* (6), 323–329.
- (196) Flemming, H.-C. C.; Wingender, J. Relevance of Microbial Extracellular Polymeric Substances (EPSs)--Part II: Technical Aspects. *Water Sci. Technol.* **2001**, *43* (6), 9–16.
- (197) Liu, Y.; Fang, H. H. P. Influences of Extracellular Polymeric Substances (EPS) on

- Flocculation, Settling, and Dewatering of Activated Sludge. *Crit. Rev. Environ. Sci. Technol.* **2003**, 33 (3), 237–273.
- (198) Boyle, J. A.; Pickett-Heaps, J. D.; Czarnecki, D. B. Valve Morphogenesis in the Pennate Diatom *Achnanthes Coarctata*. *J. Phycol.* **1984**, 20 (4), 563–573.
- (199) Mayer, C.; Moritz, R.; Kirschner, C.; Borchard, W.; Maibaum, R.; Wingender, J.; Flemming, H. The Role of Intermolecular Interactions : Studies on Model Systems for Bacterial Biofilms. **1999**, 26, 3–16.
- (200) Sheng, G. P.; Yu, H. Q.; Li, X. Y. Extracellular Polymeric Substances (EPS) of Microbial Aggregates in Biological Wastewater Treatment Systems: A Review. *Biotechnol. Adv.* **2010**, 28 (6), 882–894.
- (201) Hamm, C. E.; Merkel, R.; Springer, O.; Jurkojc, P.; Maiert, C.; Prechtelt, K.; Smetacek, V. Architecture and Material Properties of Diatom Shells Provide Effective Mechanical Protection. *Nature* **2003**, 421 (6925), 841–843.
- (202) Coombs, J.; Darley, W. M.; Holm-Hansen, O.; Volcani, B. E. Studies on the Biochemistry and Fine Structure of Silica Shell Formation in Diatoms. Photosynthesis and Respiration in Silicon-Starvation Synchrony. *Plant Physiol.* **1967**, 42, 1607–1611.
- (203) Dickinson, G. H.; Vega, I. E.; Wahl, K. J.; Orihuela, B.; Beyley, V.; Rodriguez, E. N.; Everett, R. K.; Bonaventura, J.; Rittschof, D. Barnacle Cement: A Polymerization Model Based on Evolutionary Concepts. *J. Exp. Biol.* **2009**, 212 (21), 3499–3510.
- (204) Barlow, D. E.; Dickinson, G. H.; Orihuela, B.; Kulp, J. L.; Rittschof, D.; Wahl, K. J. Characterization of the Adhesive Plaque of the Barnacle *Balanus Amphitrite*: Amyloid-like Nanofibrils Are a Major Component. *Langmuir* **2010**, 26 (9), 6549–6556.

- (205) Wiegemann, M. Adhesion in Blue Mussels (*Mytilus Edulis*) and Barnacles (Genus *Balanus*): Mechanisms and Technical Applications. *Aquat. Sci.* **2005**, *67* (2), 166–176.
- (206) Kamino, K.; Inoue, K.; Maruyama, T.; Takamatsu, N.; Harayama, S.; Shizuri, Y. Barnacle Cement Proteins: Importance of Disulfide Bonds in Their Insolubility. *J. Biol. Chem.* **2000**, *275* (35), 27360–27365.
- (207) Waite, J. H. Nature's Underwater Adhesive Specialist. *Int. J. Adhes. Adhes.* **1987**, *7* (1), 9–14.
- (208) Yu, J.; Kan, Y.; Rapp, M.; Danner, E.; Wei, W.; Das, S.; Miller, D. R.; Chen, Y.; Waite, J. H.; Israelachvili, J. N. Adaptive Hydrophobic and Hydrophilic Interactions of Mussel Foot Proteins with Organic Thin Films. *Proc. Natl. Acad. Sci.* **2013**, *110* (39), 15680–15685.
- (209) Lee, B. P.; Messersmith, P. B.; Israelachvili, J. N.; Waite, J. H. Mussel-Inspired Adhesives and Coatings. *Annu. Rev. Mater. Res.* **2011**, *41* (1), 99–132.